UNIVERSITÀ DEGLI STUDI DI CAGLIARI

FACOLTÀ DI INGEGNERIA

DIPARTIMENTO DI INGEGNERIA DEL TERRITORIO

DOTTORATO DI RICERCA
IN INGEGNERIA DEL TERRITORIO
XIX CICLO

SSD: ICAR/01 IDRAULICA

LAGRANGIAN ACCELERATION MEASUREMENTS VIA PTVA (PARTICLE TRACKING VELOCIMETRY AND ACCELEROMETRY) ON A TURBULENT-LIKE FLOW

Tesi di dottorato

Relatori:
Prof. Giorgio Querzoli
Prof. John Christos Vassilicos

Dottorando:
Simone Ferrari

Cagliari, 1 Febbraio 2007

CONTENTS

1. INTRODUCTION

Acceleration is of primal relevance in fluid mechanics, as it shows the effect of the combination of all the forces acting on a fluid flow; the Navier-Stokes equations highlight this fact and the importance of its knowledge in the description of a fluid motion:

$$\vec{a} = \frac{D\vec{u}}{Dt} = \vec{f} - \frac{\nabla P}{\rho} + \upsilon \nabla^2 \vec{u} + \frac{\upsilon}{3} \nabla(\nabla \cdot \vec{u}) \tag{1.1}$$

Moreover, only in few particular cases (as for example, in parallel fluxes such as Couette one) it is possible to analytically solve them: for the other cases it would be important to measure their single components. Unfortunately, despite the acceleration is at the very base of fluid motion (see, for instance, Tsinober 2001), only few measurement of the acceleration in the Lagrangian frame can be found in literature. Even if, on one hand, a certain number of authors have studied acceleration properties via numerical simulations, for instance Vedula and Yeung (1999), Tsinober et al. (2001), Biferale et al. (2004), Goto et al. (2005), Osborne et al. (2005), Chen et al. (2006), on the other very few examples of its experimental measure are available up to now. Moreover, among them not all the measurements are taken in the Lagrangian frame: among the Eulerian measurements, Christensen and Adrian (2002), Dong et al. (2001) and Lowe and Simpson (2005) can be pointed out, among the Lagrangian ones, Virant and Dracos (1997), Ott and Mann (2000), La Porta et al. (2001), Voth et al. (2002) and Luthi et al. (2005) can be found.

This is due to the fact that the Lagrangian measurement of the acceleration of a fluid it is not surely a trivial one. Among the difficulties to measure and analyse the acceleration there is the fact that the acceleration, $\vec{a}$, is a Galilean invariant composed of two components (namely, the local rate of change of the velocity in an Eulerian frame, or "local acceleration", $\frac{\partial \vec{u}}{\partial t}$ and a convective acceleration $(\vec{u} \cdot \nabla)\vec{u}$) which are not Galilean invariants. Measurements of the Eulerian field of the acceleration by time differencing successive measurements of the Eulerian velocity field have been performed (for instance, by Christensen and Adrian, 2002). Anyway, when the flow is strongly convected by a mean flow or when small eddies are swept by larger ones (as shown in equation (1.2)

$$\vec{a} = \frac{D\vec{u}}{Dt} = \frac{\partial \vec{u}}{\partial t} + (\vec{U}_C \cdot \nabla)\vec{u} - (\vec{U}_C \cdot \nabla)\vec{u} + (\vec{u} \cdot \nabla)\vec{u} \tag{1.2}$$

where the velocity $\vec{U}_C$ represents the Galilean choice for the referee, $\frac{\partial \vec{u}}{\partial t} + (\vec{U}_C \cdot \nabla)\vec{u}$ is the "swept local acceleration" and $-(\vec{U}_C \cdot \nabla)\vec{u} + (\vec{u} \cdot \nabla)\vec{u}$ the swept convective acceleration, in the same referee), $(\vec{U}_C \cdot \nabla)\vec{u}$ can be dominant and a weak but not strictly zero acceleration can become very difficult to measure. This implies a very high quality of the measurement, such as to catch very low value of acceleration, and is even more crucial for Eulerian measurement, as they need to be of high precision to measure

cial for Eulerian measurement, as they need to be of high precision to measure "fluctuation" of acceleration that are weak compared to $(\vec{U}_C \cdot \nabla)\vec{u}$ for both local and convective acceleration.

Lagrangian statistics of acceleration are also important for transport, stirring and mixing. Moreover, for particles dispersion (and so for stirring that can widely enhance mixing), it is not only $\vec{a}$ which is important but also its divergence, $\nabla \cdot \vec{a}$, as stated in Vassilicos (2002). The estimation of $\nabla \cdot \vec{a}$ needs accuracy on $\vec{a}$ as well as on its spatial derivatives: this is, at the state of the art, a challenging measurement from the experimental point of view.

The Navier-Stokes equations are not, however, enough to allow the understanding of turbulent flows that, at this stage, remain the only misunderstood field of classical Mechanics. This despite that turbulence is present almost everywhere and so it has many practical applications. For instance, turbulence has a huge role in stirring, enhancing mixing by increasing the transfer rate of momentum, energy and many other properties. The core of stirring is the dispersion of particles: among the studies about particle dispersion, Taylor (1921), investigating one particle statistics, found out that the mean square displacement of the particles is, at small times, approximately proportional to the square of time whilst, for large times, the displacement is proportional to time. Richardson (1926) discovered the relationship that relates the particle dispersion to time (which then became the celebrated Richardson's law of turbulent diffusion), stating that the mean square distance between two fluid elements is proportional to the third power of time (valid in the inertial range of scale).

It is known that pairs of particles travel together for a long time before they rapidly disperse when they meet a particular point in the flow, a hyperbolic stagnation point. The flow structure has straining regions of vortices and of stagnation points; in particular, two-dimensional turbulence has been shown to have a multiple-scale instantaneous streamline structure of cats' eyes within cats' eyes, which can be outlined as two vortices (i.e., two elliptical stagnation points) linked by a hyperbolic stagnation point, see Figure 1.1.

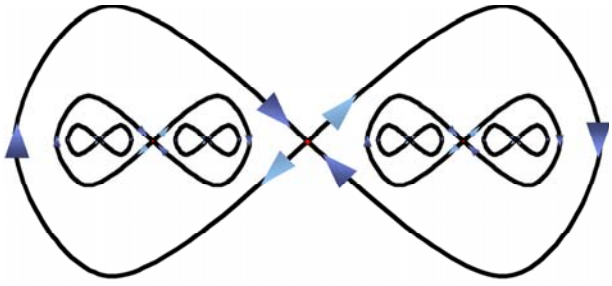

Figure 1.1 Schematic of a multiple-scale streamline structure of cats' eyes within cats' eyes.

This multiple-scale (fractal) instantaneous streamline structure, which can be found also in three-dimensional turbulence, influences the energy spectrum and other properties of the flow such as dissipation and mixing. For example, according to Davila and Vassilicos (2003), this multi-scale structure of stagnation points is intimately linked to flow energy spectra, as there is a relationship between the number of stagnation points and the fractal dimension and also between the latter and the power exponent of the energy spectra.

These aspects will be better outlined in chapter 2, relating to turbulent flows and turbulent-like flows.

To model and study some of the multiple-scale aspects associated to turbulence as well as to stirring and mixing, Rossi et al. (2005, 2006a and 2006b) have generated, in the Hydraulics Laboratory of the Imperial College London, a quasi-two dimensional multiple-scale flow experiment. This multiple-scale flow has a multiple scale distribution of stagnation points according to the flow structures the stagnation points are connected to. Rossi et al. (2005 and 2006a) have shown in the laboratory that a fractal forcing can impose the power law energy spectrum of a flow. This experimental result is confirmed by the Direct Numerical Simulation (DNS) of Hascoët et al. (2006a). As it is not possible to fully control turbulence or its complicated structure, the aim of this experiment is to simulate a flow with some aspects of turbulence, which can be fully controlled: a "turbulent-like" flow. One advantage of this kind of flow is that its topology and its forcing time dependence is known and controlled.

The experimental set-up, the procedures followed to prepare and carry out the experiments and the post-processing will be showed in chapter 3.

For this multiple-scale flows experiment, acceleration is important for the behaviour of all the scales, so the target is to measure, accurately, velocity and acceleration in the Lagrangian frame on these turbulent-like flows. An available technique to measure the velocity in the Lagrangian frame is Particle Tracking Velocimetry. The measurements need to be very accurate at all the scales, with a critical insight given to the close vicinity of the hyperbolic stagnation points (where the velocities are small but with strong curvature of the streamlines and high strain). One extra difficulty for time dependent flows is that these stagnation points can move, even if this displacement is small compared to turbulence intensity (hereafter $\vec{u}_{RMS}$), as shown in Goto et al. (2005). These points and their connected structures are thus difficult to measure, but at the same time they are areas of strong streamlines curvature and so of first importance for dispersion and turbulent flows. In addition, considering a bounded displacement of these points, we should expect their acceleration to be time dependent. As the acceleration measurement has to be accurate at large and small scales, including large and low intensity of the acceleration, a great care is accorded to the trajectory extraction.

In order to achieve the target of an accurate acceleration measure on these turbulent-like multi-scale flows, the use of a self-adaptive iterative method Particle Tracking Velocimetry and Accelerometry (PTVA) is proposed here: this method relies on an adaptive number of tracked positions, for the trajectories approximation, depending only on

the local flow properties. The criterion proposed holds the potential to "withdraw" some convection information and thus to extract more accurately the acceleration and velocity of convected structures. This method is validated with a geometrical approach, with and without convection and time dependency, and later on used in order to extract velocity and acceleration in the Lagrangian frame from these multiple-scale flow experiments.

On chapter 4, the PTVA method will be explained, validated with a geometrical approach and its accuracy compared with some previous measurement methods based on PTV.

PTVA has permitted to obtain the Lagrangian statistics of the flow such as the probability distribution functions of instantaneous velocity and acceleration. Taking advantage of the Eulerian repeatability of these measurements (as they are performed on multiple-scale laminar flows), PTVA has also allowed to extract the Eulerian fields of $\vec{u}$ and $\vec{a}$ from the Lagrangian information and, so, to study their multiple-scale distribution according to the flow topology and to its fractal forcing, to measure the Eulerian field of the viscous term of the Navier-Stokes equations, $\upsilon\nabla^2\vec{u}$, permitting to complete the measurement of the Navier-Stokes equations' terms for incompressible flows.

Finally, the issue of efficient mixing was faced. Efficient mixing can be defined as the one achieved when a required mixing is reached with the minimum power input or, vice versa, where the mixing is maximized given a certain power input. The chance to measure an efficient mixing and therefore to design an efficient mixer would be of major significance for many fields in industry and for a lot of engineering applications (for example, a quasi-two-dimensional efficient mixer can be important for the glass and plastic sheet industry). To clarify which one of the feasible configurations of a particular apparatus gives efficient mixing, the measure of the power input into the flow and of how this input generates mixing is needed. As a way to analyse the power input/output and transformation for unit mass in the flow, the study of the scalar field of the scalar product $\vec{u}\cdot\vec{a}$ and of the pseudo-vectorial field of the vectorial product $\vec{u}\times\vec{a}$ has been chosen, while as a way to measure where there is a strong stirring in the flow, the study of the acceleration divergence $\nabla\cdot\vec{a}$ was selected (see Vassilicos, 2002). In particular, the measure of $\nabla\cdot\vec{a}$, implying a spatial derivative on the acceleration (already coming out from two temporal derivatives of the trajectory) was challenging; in fact, on the Author's knowledge, an experimental measure of the acceleration divergence over the entire investigation field had been never achieved before.

These results will be discussed in details in chapter 5.

2. TWO-DIMENSIONAL TURBULENT FLOWS AND TURBULENT-LIKE FLOWS

1 INTRODUCTION

The work presented in this thesis is a part of a bigger project with the aim of studying turbulent flows through turbulent-like flows: in brief, the idea is to consider turbulence in its entirety like a wall, to dismantle it into its characteristic constituents (the bricks of turbulence) and to try understanding what is the role of the single constituents in re-building the whole picture of turbulence; this can be done adding, at the beginning, only few bricks and trying to understand their role, to then add other bricks to see how the global picture of turbulence is recreated. As the ultimate target of turbulent-like flows is so to understand more carefully how turbulent flows work, a brief introduction regarding turbulent flows and their role in Engineering will be given in this chapter, with a particular attention to two dimensional turbulence (section two), to eventually describe the so-called turbulent-like flows (section three).

2 TURBULENT FLOWS AND TWO-DIMENSIONAL TURBULENCE

Turbulence can be defined as a state of a fluid flow that is very irregular in time and in space. Turbulence needs to be maintained by some external forcing; otherwise, if the external energetic input stops, it can become the so-called decaying turbulence, that tends to an equilibrium state. As the term suggests, turbulence was studied the first time in fluid mechanics and was later generalized for far-from-equilibrium states in solids and plasma (Falkovich et al., 2001).

A complete definition of turbulence, taking into account all its characteristics, is difficult to get, but some common features of all the turbulent flows can be spotted, like a fluctuating velocity field, highly disordered in space and time, that is unpredictable because an infinitesimal change in the initial conditions produces a finite change to the subsequent motion (Davidson, 2004). This implies that, after more than one century from the first experiments in the field (Reynolds 1883) and despite the fact that the equations governing the motion (the Navier-Stokes equations) have been known since 1845, there are very few properties of turbulent flows that can be predicted with a certain accuracy: the understanding of these flows remains, at this stage, the only misunderstood field of classical Mechanics.

This despite the fact that turbulence is present almost everywhere and so it has many practical applications in Engineering, Medicine, Geophysics, etc. As a matter of fact, this lack of understanding is the most serious obstacle to reach a systematic description of many important engineering and environmental phenomena: for instance, turbulence has a huge role in the motion of air around cars and airplanes, in dilution of pollutant released in the atmosphere or in the sea (Figure 2.1) as it enhances mixing increasing the

transfer rate of momentum, energy and many other properties, in weather forecasts, in prevision of the motion of hurricanes (Figure 2.2), in the study of motion of water and air masses in the ocean and in the atmosphere (Figure 2.3), in mixing and combustion in engines and chemical reactors, in reduction of drag, in the study of the wake behind an object or of the air flowing through the lungs, etc. Transport processes of scalar quantities by turbulent flows also play an important role in many environmental phenomena, such as particle transport in geophysical flows (Boffetta et al., 2001).

Not only turbulence is present almost everywhere, it is also present in a broad range of length scales, from 10^{23} m in galaxies, to 10^{-5} m in liquid crystal flows, passing through 10^{7} m in the Earth's atmosphere, 10^{3} m in clouds and 10^{-2} m in soap films.

An example of the major role that turbulence plays in the dilution of passive scalars can be the release of a pollutant fluid in the sea (see Figure 2.1, where the turbulent spreading of a buoyant jet released in the sea is made visible by the use of LIF, Light Induced Fluorescence, technique): as there is a linear relation between the concentration of pollutant and the light intensity, it possible to note how the concentration is decreasing from the jet origin along the jet trajectory. This is made possible by the transition to turbulence of the jet: as a matter of fact, the jet keeps initially the width of the outlet, then widens where turbulent structures (Kelvin-Helmholtz structures) arise. These structures include external fluid into the jet, so allowing a decrease of the pollutant concentration and its dilution. It is possible to stress that, without the turbulence that disperses the pollutants, the traffic of cars going through the streets would asphyxiate immediately most of the citizens of modern towns.

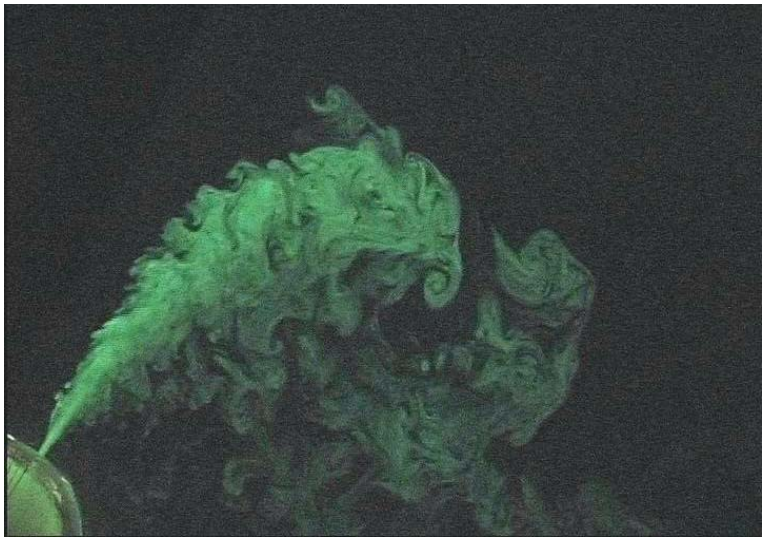

Figure 2.1 Turbulent spreading of a buoyant jet released in the sea: experiment carried out making use of Light Induced Fluorescence (LIF); as there is a linear relation between the concentration of pollutant and the light intensity, the reduction of light intensity implies the dilution of the discharged substance.

Figure 2.2 A hurricane or a quasi two-dimensional vortex with its elliptical stagnation point

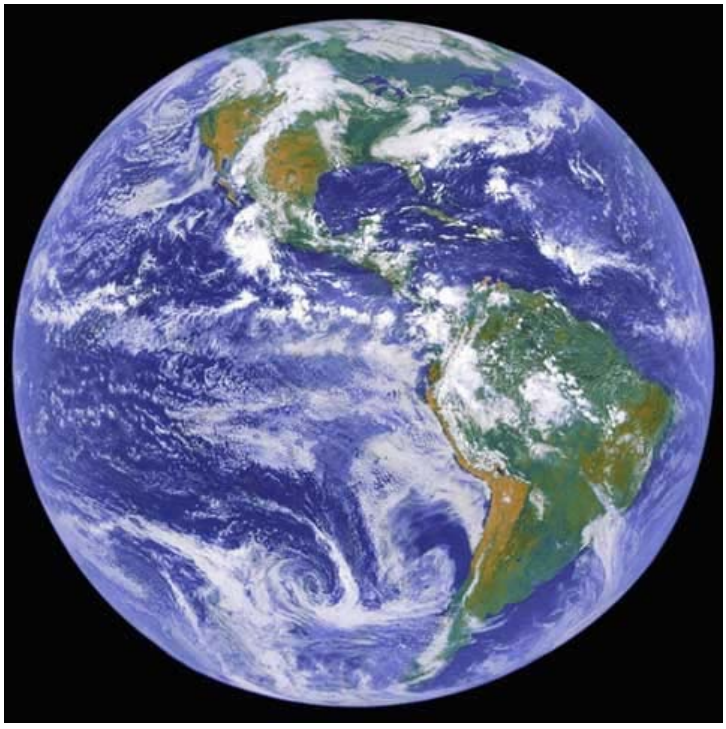

Figure 2.3 A quasi-two-dimensional jet (close to Chile) with a hyperbolic stagnation point and two elliptical ones.

Quasi-two-dimensional turbulent flows occur in many physical situations, for example in atmosphere and oceans, mainly because of stratification and Heart's rotation (Salmon, 1998). Two-dimensional turbulence is a field rich of activities, both from the numerical and experimental point of view.

On the numerical side, Boffetta et al. (2000) investigated the deviation from the Gaussian behaviour of the inverse cascade, Boffetta and Celani (2000), studied via Direct Numerical Simulation the pair dispersion in turbulence, Bracco et al. (2004), studied numerically the dynamics of passive Lagrangian tracers in three-dimensional quasi-geostropic turbulence and compared it with the behaviour of two-dimensional barotropic turbulence (finding that two-dimensional turbulence can carry over to more realistic baroclinic flows, such the ones in the large scale atmospheric and oceanic motion). On the experimental side, Cardoso et al. (1994), carried out a quantitative experimental study of the free decay of quasi-two-dimensional turbulence, Williams et al. (1997), experimentally measured the mixing of a passive scalar, Hansen and Tabeling (1999), studied the interaction between coherent structures in two-dimensional decaying turbulence (showing that when the forcing is stopped like-sign vortices start to merge forming fewer and larger structures), Jullien (2003), did an experimental statistical analysis of the separation of particle pairs in the enstrophy cascade, Voth et al. (2003), experimentally determined the mixing rate for a magnetically forced two-dimensional time periodic flow exhibiting chaotic mixing, Cenedese et al. (2004), experimentally measured the energy spectrum of a two-dimensional electromagnetically forced turbulent flow (finding the two different slopes corresponding to direct and inverse cascade).

Two dimensional turbulence is important because it is a simplification of three dimensional one but it has, also, some peculiarities because, for example, in two-dimensional turbulence, small-scale structures merge to bigger ones: an initially disorganized two-dimensional flow finally becomes organized in large persistent vortical structures (the so-called *self-organization* principle of the two-dimensional turbulence), exactly the opposite of what happens in three-dimensional turbulence (see below).

A second difference between three-dimensional and two-dimensional turbulence is the effect of "vortex stretching": in three-dimensional turbulence, when a vortex is stretched, the matter contained in it is pulled towards the rotation axis of the vortex and, due to conservation of angular momentum, it rotates faster. In a two-dimensional flow the mechanism of vortex stretching is absent and this appears to have important consequences for its dynamics: the kinetic energy of the flow now shows a spectral flux from the small to the large length scales. This property can be derived from the equation for the vorticity of the flow

$$\vec{\omega} = \nabla \times \vec{u} \tag{2.1}$$

For a two-dimensional flow, the vorticity vector is always directed perpendicular to the plane of motion and, due to the mechanism of stretching and tilting, the vorticity is a conserved quantity for inviscid flows. From the inviscid vorticity equation two conser-

vation laws can be derived, namely those for the kinetic energy $E = \frac{\|\vec{u}\|^2}{2}$ and for the so-called *enstrophy* $V = \frac{\|\vec{\omega}\|^2}{2}$, which can be considered as a measure for the total vorticity of the flow. These conserved quantities E and V can be written in spectral form:

$$E \approx \int_0^\infty e(k,t)dk = const \tag{2.2}$$

$$V \approx \int_0^\infty k^2 e(k,t)dk = const \tag{2.3}$$

where *e(k, t)* is the spectral energy density in the wavenumber interval (k, $k+dk$) at time t. In agreement with Kraichnan (1967) prediction, the coupled constrains of energy and enstrophy conservation make the energy injected into the flow going toward the large scales (in three-dimensional turbulence, the energy flows from large toward small scales in the so called direct cascade). As two-dimensional turbulence has both kinetic energy and enstrophy as inviscid constants of motion, it admits two inertial ranges,

$$E(k) \sim \varepsilon^{2/3} k^{-5/3} \tag{2.4}$$

and

$$E(k) \sim \eta^{2/3} k^{-3} \tag{2.5}$$

where ε is the rate of cascade of kinetic energy per unit mass, η is the rate of cascade of enstrophy, k is the wavenumber, and the kinetic energy per unit mass is the integral from zero to infinite of $E(k)\,dk$. The $k^{-5/3}$ range is found to entail backward energy cascade, from higher to lower wavenumbers k, together with zero-vorticity flow. The k^{-3} range gives an upward vorticity flow and zero-energy flow.

Turbulence can arise when the so-called Reynolds number *Re*, representing the ratio between inertial and viscous forces, is high enough. For example, an obstacle of size L placed into a fluid moving with velocity U creates a turbulent wake if the Reynolds number *Re* is large enough

$$Re = U\,L/\upsilon >> 1 \qquad (2.6)$$

where υ is the kinematic viscosity; similar consideration can be done for a fluid moving with velocity U along a pipe of diameter L. At large Re, the viscous dissipation of the flow perturbations produced at the scale L are small compared to the nonlinear effects, so the nonlinearity produces motions of smaller and smaller scales until viscous dissipation stops this at a scale much smaller than L: there is so a wide interval of scales, the inertial range, where viscosity is negligible and nonlinearity dominates.
This complicated and irregular dynamics makes necessary a statistical description based over ensemble average, i.e. an average of some quantity of interest across the entire ensemble of flows. As turbulent flows vary randomly in time and in space, a sufficiently long time or space average is usually a good approximation to the ensemble average.
Conservation laws impose some constraints on dynamics and therefore conserved quantities must play an essential role in turbulence. Pumping and dissipation break the conservation laws, but both factors do not act in the inertial interval: for instance, in the incompressible turbulence, the kinetic energy is pumped by external forcing and is dissipated by viscosity. This fact is in agreement with the observation of smoke plumes from chimneys or from a cigarette that show that large vortices tend to be unstable and to break up into smaller vortices which, in turn, become again unstable and break up into even smaller vortices. This process continues down to molecular length scales, the scales at which the kinetic energy of the flow is eventually dissipated, i.e. transformed into heat. Hence, there is a spectral energy flux from the large to the small length scales, and this phenomenon is known as the "energy cascade" in three-dimensional turbulence. Phenomenologically, this cascade expresses itself in the development of a relatively disorderly flow from an initially rather ordered flow: this is in striking contrast with the *self-organization* principle of the two-dimensional turbulence seen above. According to the work of Kolmogorov, the kinetic energy flows throughout the inertial interval of scales in a cascade-like process. A central property of turbulent flows is that their energy spectra are continuous and in fact power-law functions of wavenumber over appropriate intermediate ranges of scales. In homogeneous isotropic turbulence, it is known since Kolmogorov's seminal contributions of 1941 and the many experimental works which followed, that the energy spectrum's shape is not too far from $E(k) \sim k^{-5/3}$ in the inertial range (see Davidson, 2004). This energy cascade can explain some of the basic macroscopic manifestation of turbulence: for instance, the fact that the rate of dissipation of the dynamical integral of motion has a finite limit when the dissipation coefficient tends to zero. This explains why the mean rate of the viscous energy dissipation does not depend on the viscosity at large Reynolds numbers. That means that the symmetry of the inviscid Euler equation is broken by the presence of the viscous term, even though the latter might have been expected to become negligible in the limit of Re that goes to infinite. Due to this non-linearity, there is not a general description of turbulent flows and, in order to describe the turbulence statistics of strongly interacting systems, one has to solve problems on a case-by-case basis, with most cases still unsolved.

This sentence of Sir Horace Lamb quoted by Goldstein and Hultgren (1989) can give an idea of the difficulties encountered in the field of turbulence: “I am an old man now, and when I die and go to Heaven there are two matters on which I hope enlightenment. One is quantum electro-dynamics and the other is turbulence. About the former, I am really rather optimistic”.

If from the theoretical point of view studying turbulence could seem frustrating, it can be an exciting topic when one gives a look to some practical aspects of turbulence: the most important one is mixing. As a matter of fact, turbulence is an enhancer of mixing, that comes from the combined action of stirring (stretch and fold mechanism) and diffusion: the role of stirring is to distort and stretch out blobs or clouds of scalar quantities, so that their bounding surface increase in area until the molecular diffusivity can make feel its effects.

The core of stirring is the dispersion of particles: among the studies about particle dispersion, Taylor (1921), investigating one particle statistics, found out that the mean square displacement of the particle is approximately proportional to the square of time at small times while, for large times, the displacement is proportional to time.

Later, Richardson (1926) discovered the relationship between particle dispersion and time (which then became the celebrated Richardson’s law of turbulent diffusion), stating that the mean square distance between two fluid elements is proportional to the third power of time (valid in the inertial range of scales).

Is turbulence a random phenomenon? For many decades the answer to this question was positive and turbulence was studied only from a statistical point of view; however, it has been shown recently that the statistics of particle pair dispersion in turbulent flows (as said, proportional to the third power of time) are different from the ones in Brownian motion (random walk) (Ottino, 1990).

2.1 Topological aspects of turbulent flows

During the last two decades, increasing attention has been paid to the topological aspects of turbulent flow: in both experimental and numerical works characteristic structures were detected (Moffat, 2001), with some characteristic points of the flow, called critical points (points with zero velocity relative to an appropriate observer where the streamlines slope is indeterminate), playing a major role in the behaviour of the flow. Given a certain distribution of critical points, much of the flow field in their surroundings can be deduced, as there is only a limited number of ways that the streamlines can be joined. Consider, for incompressible flows, the Navier-Stokes equations

$$\frac{\partial u_i}{\partial t} + u_j \frac{\partial u_i}{\partial x_j} = -\frac{1}{\rho}\frac{\partial P}{\partial x_i} + \upsilon \frac{\partial^2 u_i}{\partial x_j \partial x_j} \tag{2.7}$$

and the continuity one:

$$\frac{\partial u_i}{\partial x_i} = 0 \tag{2.8}$$

where u_i is the ith velocity component, ρ is the density, P the pressure and ν the kinematic viscosity. Following Perry and Chong (1987), an arbitrary point O in the flow can be chosen as origin for a Taylor series to expand u_i in terms of x_j :

$$u_i = \dot{x}_i = A_i + A_{ij} x_j + A_{ijk} x_j x_k + ... \tag{2.9}$$

The coefficients A are symmetric tensors in all the indices except the first. If the point O is exactly on a critical point, the streamlines slope is indeterminate and the zeroth-order terms A_i are null. The quoted Authors consider two classes of critical points: the *no-slip critical points* (where $A_{ij} = 0$ and A_{ijk} is finite if $j = 3$ or $k = 3$ but zero in all the other cases, with x_3 the coordinate normal to the no-slip boundary) and the free-slip critical points (where A_{ij} has a finite value). Asymptotically exact solutions of equations (2.7) and (2.8) can be derived close to the critical points, pinpointing a certain number of flow patterns, by integrating the velocity field: for instance, the velocity field close to a no-slip critical point can be expressed as:

$$\frac{u_i}{x_3} = B_{i\alpha} x_\alpha \tag{2.10}$$

where $B_{i\alpha}$ is a 3 × 3 matrix linearly related to A_{i3k} and A_{ij3}. A similar relation can be found for the velocity field close to a free-slip critical point. So, the properties and classification of the flow patterns can be obtained by examining the eigenvalues and eigenvectors of $B_{i\alpha}$. If the eigenvalues and eigenvectors are real, three planes containing solution trajectories can be defined by the eigenvectors; if eigenvalues and eigenvectors are complex, there will exist in general only one plane that contain solution trajectories. On each of those planes, a new coordinate system can be defined where the following equation holds:

$$\begin{bmatrix} \dot{y}_1 \\ \dot{y}_2 \end{bmatrix} = \begin{bmatrix} a & b \\ c & d \end{bmatrix} \begin{bmatrix} y_1 \\ y_2 \end{bmatrix} \tag{2.11}$$

or

$$\dot{\vec{y}} = F\vec{y} \tag{2.12}$$

where y denotes a time differentiation and F is a 2 × 2 matrix. The two quantities

$$p = -(a + d) = -trace\ F \tag{2.13}$$

and

$$q = (ad - bc) = det\ F \tag{2.14}$$

can be used to classify the different types of critical points on a p-q chart (Figure 2.4), obtaining nodes, saddles and foci. For two dimensional flows, the only critical points that can occur are saddles (or hyperbolic stagnation points) and degenerate focus or center (or elliptical stagnation points).

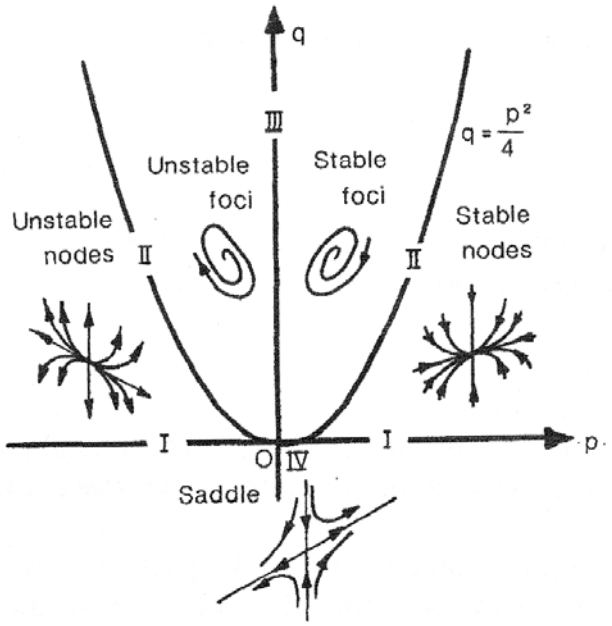

Figure 2.4 Classification of critical points on the p-q chart (adapted from Perry and Chong, 1987).

The application of this topological concept of critical points has been applied to the description of many common flows. For instance, in Figure 2.5, the instantaneous velocity field of an externally illuminated smoke pattern, measured in the vertical plane of symmetry, clearly shows three classes of critical points (Perry and Chong, 1987).

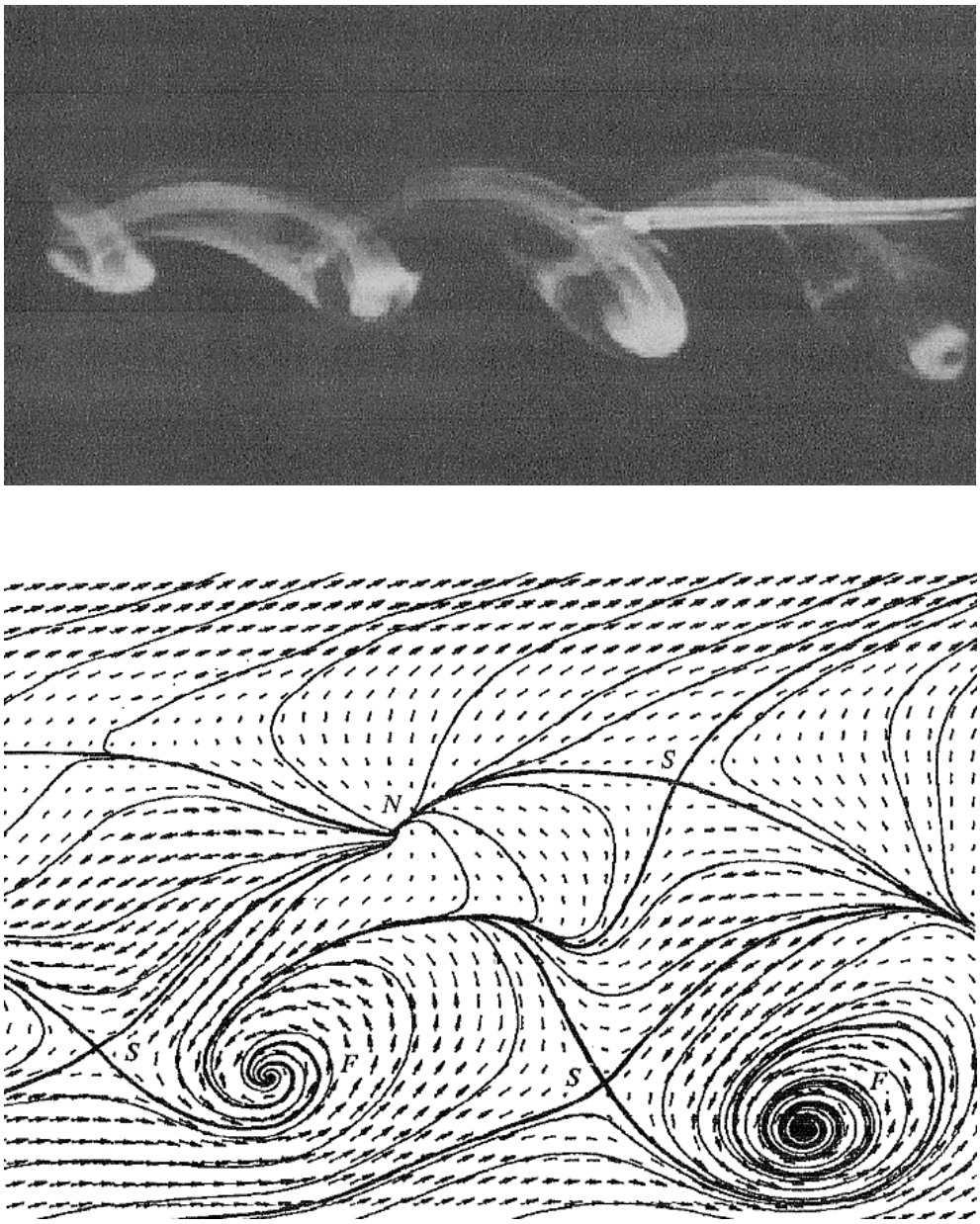

Figure 2.5 On the top, a smoke pattern, externally illuminated, passing a hot wire; on the bottom, the instantaneous velocity field in the vertical plane of symmetry: S stands for saddle, F for focus and N for node (adapted from Perry and Chong, 1987).

The appearance of coherent structures (vortices or eddies), connected to elliptical stagnation points, in two-dimensional turbulent flows is well established (see, for instance, Figure 2.2 and 2.3), both experimentally (starting from early experiments by Hopfinger et al., 1983, and Couder et al., 1989 until recent ones by Hansen and Tabeling, 2000) and numerically (e.g. McWilliams, 1984). In turbulent flows a large hierarchy of these eddies can be found, with sizes covering a wide range of length-scales. The energy spectrum of the turbulence *E(k)* is generally used to describe this hierarchy of eddies, *k* being the wave number or inverse length-scale. In spatially homogeneous non-decaying turbulence, the well-known Kolmogorov's $k^{-5/3}$ law for *E(k)* characterises the inertial range of *k*. A statistically homogeneous and non-decaying turbulent flow in two dimensions with this kind of energy spectrum has been studied experimentally by Paret and Tabeling (1997) and numerically by Fung and Vassilicos (1998). They found that instantaneous snapshots of the streamlines field (i.e., pairs of particles travel together for a long time before they rapidly disperse when they meet a particular point in the flow, a hyperbolic stagnation point) have a self-similar topological structure made of cat's eyes within cat's eyes, these being streamline structures consisting of two co-rotating vortices (two elliptical stagnation points) with one straining hyperbolic point in between (see Figures 2.5, 2.6 and 2.7). Smaller cat's eyes have smaller time scales determined by *E(k)* and they are therefore essential in turbulent mixing.

Fung and Vassilicos (1998) have also reproduced, with their Kinematic Simulation, Richardson's law for the separation of fluid elements pairs in non-decaying homogeneous flows with a $k^{-5/3}$ energy spectrum

$$\langle | \Delta |^2 \rangle \propto t^3 \tag{2.15}$$

where Δ is the pair separation at time t and the brackets signify an average over many realizations. This Richardson's turbulent pair diffusion law has been confirmed by Jullien et al. (1999).

According to Davila and Vassilicos (2003), the multi-scale (fractal) structure of stagnation points typical of turbulence is intimately linked to flow energy spectra, as there is a relationship between the number of stagnation points and the fractal dimension and also between the latter and the power exponent of the energy spectra. This self-similar structure of turbulence underlies Kolmogorov's 1941 theory: turbulence creates its multi-scale fractal structure.

A link between this Richardson's law and the cited cat's eyes streamline topology has been proposed by Davila and Vassilicos (2003) in terms of D_S, that is the fractal dimension of the spatial distribution of straining hyperbolic points in two-dimensional turbulence. In their numerical simulations they found that

$$\langle | \Delta |^2 \rangle \propto t^{4/D_S} \tag{2.16}$$

with a value for D_S of 4/3 for the Kolmogorov spectrum. These studies are at the basis of the idea of the turbulent-like flows presented in the next section.

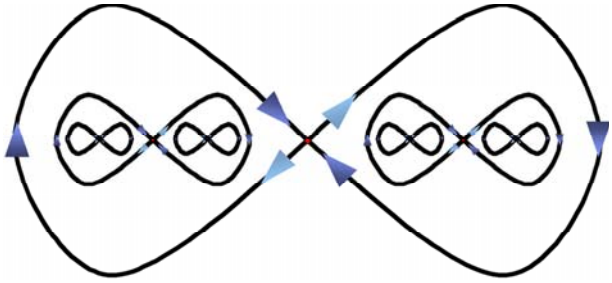

Figure 2.6 Schematic of a multiple-scale streamline structure of "cats' eyes within cats' eyes" or "8 in 8".

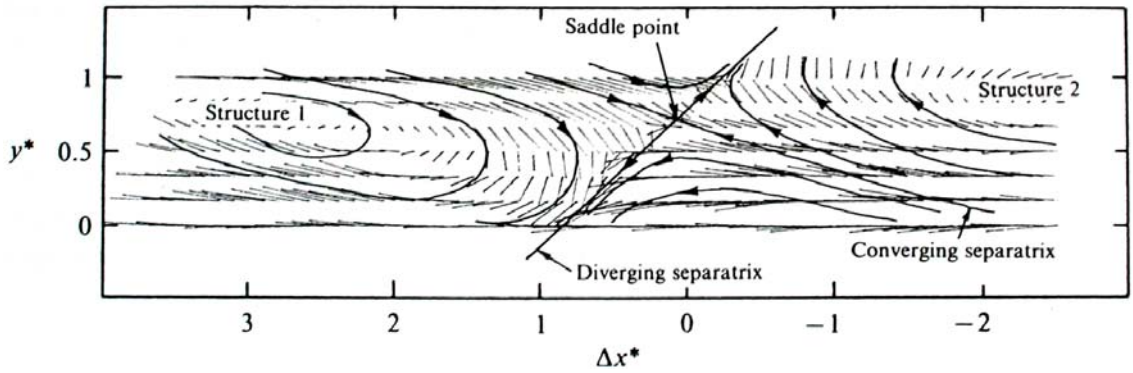

Figure 2.7 Two elliptical stagnation points connected by a hyperbolic one (adapted from Antonia et al., 1986).

3 TURBULENT-LIKE FLOWS

As previously stated, the idea of turbulent-like flows is to consider turbulence in its entirety like a wall, to dismantle it into its characteristic constituents (the bricks of turbulence) and to try understanding what is the role of the single constituents in rebuilding the whole picture of turbulence; this can be done adding at the beginning only few bricks and trying to understand their role, to then add other bricks to see how the global picture of turbulence is recreated. In the work object of the present thesis, only a first brick (a multi-scale distribution of streamline structures of "8 in 8") was used; a second brick, that is a time dependency of the forcing, has been already introduced in the experimental setup and some experiments have been already carried out but data are not

analyzed here and are kept for future work.

From the coupling of the topological approach (see previous section) and the flow control one (see next chapter), turbulent-like flows can be obtained. The aim of the turbulent-like flows is to have a full control on a flow with some characteristics of turbulence, because it not possible to fully control a turbulent flow or its complicated structure: electromagnetically forcing was chosen as it allows a full control of the number of the scales of the flow, of the topology of these scales, of the power input at each scale and of the time dependency of the forcing. In fact, the term turbulent-like flows itself refers to flows are not strictly turbulent but that simulate some of the multi-scale aspects of turbulence in a laboratory experiment where the relations between the flow topology and resulting mixing can be changed and demonstrated at will. To start, a two-dimensional flow was chosen instead of a three-dimensional.

So, to model and study some of the multiple-scale aspects associated to turbulence as well as to stirring and mixing, Rossi et al. (2005, 2006a and 2006b) have generated, in the Hydraulics Laboratory of the Imperial College London, a quasi-two dimensional multiple-scale flow experiment that has a multi-scale distribution of stagnation points (zero velocity point in Eulerian referee) according to the flow structures the stagnation points are connected to (a multi-scale flow based on the schematic given in Figure 2.4 characterised by a fractal dimension which can be varied at will so as to monitor the effects of their changes on spectra, structure functions, dissipation rates, etc).

Rossi et al. (2005 and 2006a) have shown in the laboratory that a fractal forcing can impose the power law energy spectrum of a flow and Hascoët et al. (2006) have confirmed it numerically by Direct Numerical Simulation (DNS). It should be highlighted that also if these flows have a power law of energy spectrum like turbulent flows, they are a low Reynolds number laboratory simulation of high Reynolds number flows.
These turbulent-like flows incorporate some of the essential ingredients of the turbulent pair-diffusion model of Davila & Vassilicos (2003), Goto & Vassilicos (2004), Goto et al (2005) and Osborne et al (2005). In this model, stagnation points are assumed to be responsible for pair-separation statistics because they are shown to be statistically long-lived compared to all time-scales of the turbulence and slowly moving compared to fluid elements. This model leads to

$$\overline{\Delta^2} \cong G_\Delta L^2 \left(\frac{u't}{L} \right)^\gamma \tag{2.17}$$

where Δ is the separation between fluid element pairs at time t, the overbar symbolises an average over many pairs and/or many flow realisations, G_Δ the Richardson constant - a universal dimensionless constant, see Tatarski (1960)-, L is the outer length scale (characterizing the largest eddies), u' is the root mean square turbulence velocity, t spans an intermediate range of times bounded from above by the Lagrangian correlation time-scale, and the Richardson exponent γ is given by

$$\gamma = \frac{2d}{D_S} \tag{2.18}$$

By positioning stagnation points at will in the laboratory tank of Rossi et al., it is possible to design a continuous power-law shaped energy spectrum with a chosen exponent p determined by *Ds* from the relation

$$p + \frac{2D_S}{d} = 3 \tag{2.19}$$

proposed by Davila and Vassilicos (2003) and confirmed by Goto & Vassilicos (2004). By then controlling the time dependence of this laboratory flow, it could be possible to increase the knowledge about the relations between spatio-temporal flow structure (multi-scale streamline topology and its time dependence) and scalar diffusion.

Another of the possible target of turbulent-like flow could be to control stirring and mixing to achieve efficient mixing that can be defined like the one achieved when a required mixing is reached with the minimum power input or, vice versa, when the mixing is maximized given a certain power input. Turbulent-like flows can be used to study the dependence of scalar variance decay and mixing on spatio-temporal flow structure: in fact, eddies mix contaminants and scalar concentrations over scales comparable to their own size and such mixing is therefore of limited applicability and perhaps also limited efficiency, while mixing by multi-scale forcing injects energy at various specific scales which can be chosen so as to maximise mixing efficiency.

3. EXPERIMENTS: EXPERIMENTAL SETUP, PROCEDURES, EXPERIMENTS AND POST-PROCESSINGS

1 INTRODUCTION

This chapter deals with the experimental side of this work, so with the experimental setup, with the main procedures followed to setup the experiments, with the experiments carried out and, finally, with the main post-processing elaborations done on the pictures. A general description of the experimental setup and of the procedures followed to carry the experiments out will be given in the following section, while a more detailed description will be given from the section 3 on.

2 GENERAL DESCRIPTION OF THE EXPERIMENTAL SETUP

The main target of the experimental setup is to generate and control a multi-scale distribution of stagnation points in a quasi-two-dimensional flow.

There are different methods for constraining flows into two dimensions, for example the use of soap film to obtain geometrical confinement (Couder et al, 1989, Belmonte et al., 1999), the use of liquid metals in a magnetic field (Sommeria, 1986) or the use of a system of thin fluid layers, confined in a container and driven by electromagnetic forces (Cardoso et al., 1994). The flow generated in this way can essentially be regarded as two-dimensional, as shown by Paret and Tabeling (1997). Configurations of this kind have been extensively used for many different purposes, such as studying the phenomenon of vortex stripping (Legras et al., 1998), the equilibrium states of 2D turbulence (Marteau et al., 1995), the decay of 2D turbulence (Cardoso et al., 1994), the dispersion phenomenon (Williams et al., 1997), the double cascade in 2D turbulence (Cenedese et al, 2004), etc. For this experiments, an electromagnetical forcing of a shallow layer of brine was chosen.

In the experimental set-up, a shallow layer of brine (salt water, 158 g/l NaCl), supported by a horizontal wall and contained in a tank, is electromagnetically forced by a fractal distribution of opposite pairs of Lorentz forces.

The tank is made of Perspex, with a 1.7x1.7 m^2 inner board, painted in black, at the centre of the tank, where the experiments are performed and the camera takes pictures of the 2D flow.

The electromagnetic body forcing ($\vec{j} \times \vec{B}$) is produced by the use of permanent magnets ($\vec{B}$ **,** Br ≈ 0.68T)) of various horizontal sizes (10mm, 40mm, 160mm), placed under the horizontal wall of the tank that supports the brine, in combination with electrical currents through the brine ($\vec{j}$), generated by platinum electrodes on each side of the tank. Each electrode is made of 16 platinum wires with a diameter of 11.5 μm and a length of 40 mm. Both tank's side are covered with 43 electrodes, with a typical spacing of about 4 cm between two electrodes of same polarity. The electrical field has been checked as uniform above the active part of the wall. The electrical current used in the experiments presented in this work is I = 0.53 A, leading to a two-dimensional Reynolds number of about 5000. The electromagnetical forcing is used over many scales simultaneously to design the stagnation point distribution of Figure 3.1: the three scales

of forcing are associated with a size of the square magnets of 160 mm, 40 mm and 10 mm. The size of the tank (1700 x 1700 mm^2) is large compared to the size of the magnets: the EM forcing area of the experiment represents only 2.8 % of the area of the bottom wall, which is small compared with previous works (e.g., Cardoso et al., 1994, Williams et al., 1997). Each forcing scale is made of a pair of North and South magnets, placed on an iron plate, whose spacing is about the typical length of the associated magnets. The iron plates (supporting the magnet-pairs) are of sufficient thickness to close the magnetic field.

Figure 3.1 shows a plan view of a schematic of the a fractal flow of "8 in 8" generated by the multi-scale distribution of permanent magnets used in the experiments object of this work; Figure 3.2 illustrates a vertical section of the tank with a schematic for the electromagnetic forcing of a shallow brine layer (5 mm thickness).

Due to the particular configuration of the setup, a couple of opposite wall jets is generated over each couple of North-South magnets: the hyperbolic stagnation points at each scale of forcing are so controlled by a couple of magnets.

The sustained forcing compensates the dissipation due to the bottom friction. Once the viscous damping is overcome, Lorentz forces provide a good way to control the intensity of the flow (Thibault and Rossi, 2003).

The thickness of the shallow brine layer during the experiments was about H = 5 mm (H_{MEAN} = 5.009 ± 0.121 mm). The decrease of water thickness due to evaporation is about 0.3 mm/day, which gives less than 0.1 mm during the time of the experiments (less than six hours). A thickness of 5 mm was chosen to be smaller than the smallest magnet size (10mm), because the magnetic field weakens exponentially with distance from the magnet according to the magnet's size, to be small enough to inhibit as much as possible three-dimensionality of the flow in case of strong EM forcing but also large enough for the bottom friction not to bring the flow to near standstill away from the magnets. The quasi-two-dimensionality of the flow has been checked and verified (for more details, see *Rossi et al.*, 2006). The brine is let at rest for more than 24 hours in order to reach a naturally stratified shallow layer. The working brine, obtained with 40 kg of salt diluted into 50 gallons (around 227.3 litres) of water, is made black by diluting 57 ml of black ink (without any metallic component) in it. In order to reduce the static electricity, three drops of a wetting agent for photographic use containing Ethylene Glycol (Kodak photo-flo) were added to the brine too.

Image Analysis techniques have been used to perform measurements on this flow, so the experimental set-up is completed by a 2 ADC high definition camera (2048x2048 $pixel^2$ for a maximum acquisition frequency of 14 Hz and a 14 bit depth), placed orthogonally to the measurement plane (Figure 3.3), and by two 500 W lamps that uniformly enlighten the investigation field (Figure 3.4). The flow was seeded with particles of Chemigum P83. The experiments in this paper were filmed with an acquisition frequency of 10 Hz. Two frames of different sizes (1015.4mm and 842.1mm) were investigated so as to measure the entire flow and to complete the resolution at the small scales.

Some sheets of black cardboard have been added to the corners of the tank, where the light from the two lamp comes from, and on the camera stand (Figure 3.4), and a black adhesive tape has been attached on the edges of the vertical Perspex walls (Figure 3.5), with the aim of reducing reflection an diffusion of light over the investigation field.

Finally, Figure 3.6 and 3.7 give an illustration of the platinum electrodes and of their placement on the vertical Perspex walls of the tank.

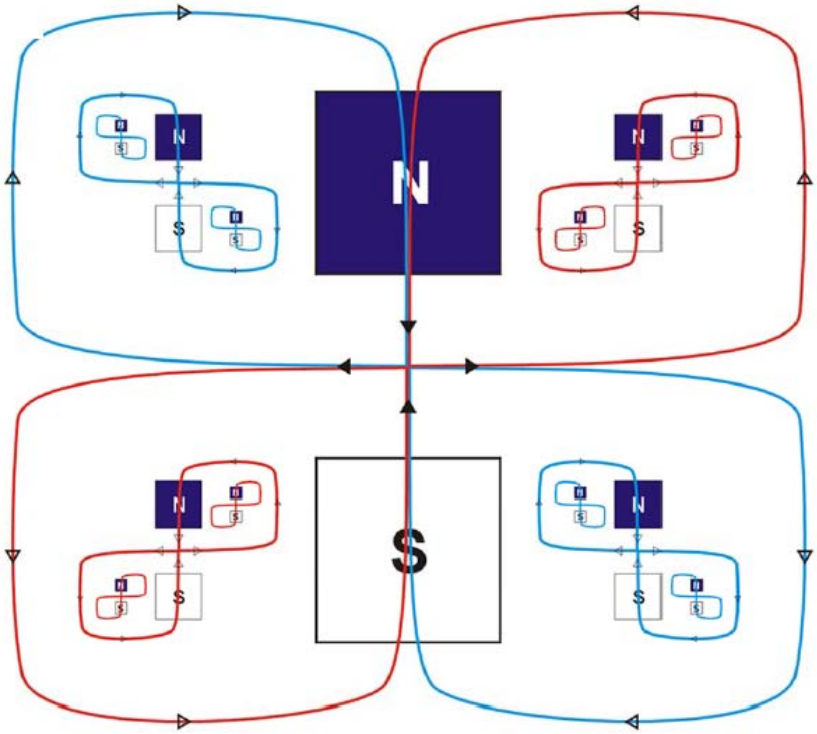

Figure. 3.1 Plan view of a schematic of the a multi-scale flow of "8 in 8" generated by the multi-scale distribution of permanent magnets used in the experiments object of this work; N and S indicate the couples of North-South magnets.

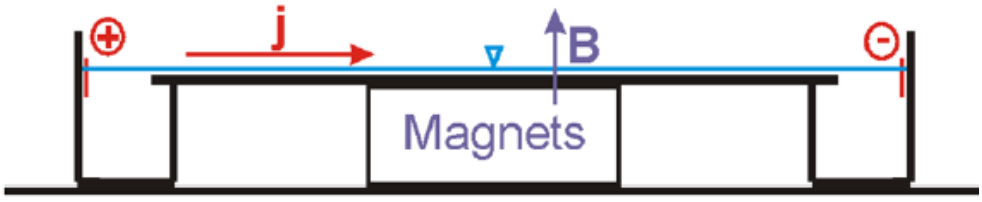

Figure. 3.2 Vertical section of the tank with a schematic for the electromagnetic forcing of a shallow brine layer (5 mm thickness).

Figure. 3.3 Picture of the experimental set-up, with the tank, the camera and its stand: the black cardboard visible on the right corner of the tank and on the camera stand has the aim of reduce reflection of light coming from the lamps (visible on Figure 3.4); the working brine is made black by diluting 57 ml of black ink.

Figure. 3.4 Picture of the experimental set-up with one of the two 500 W lamps.

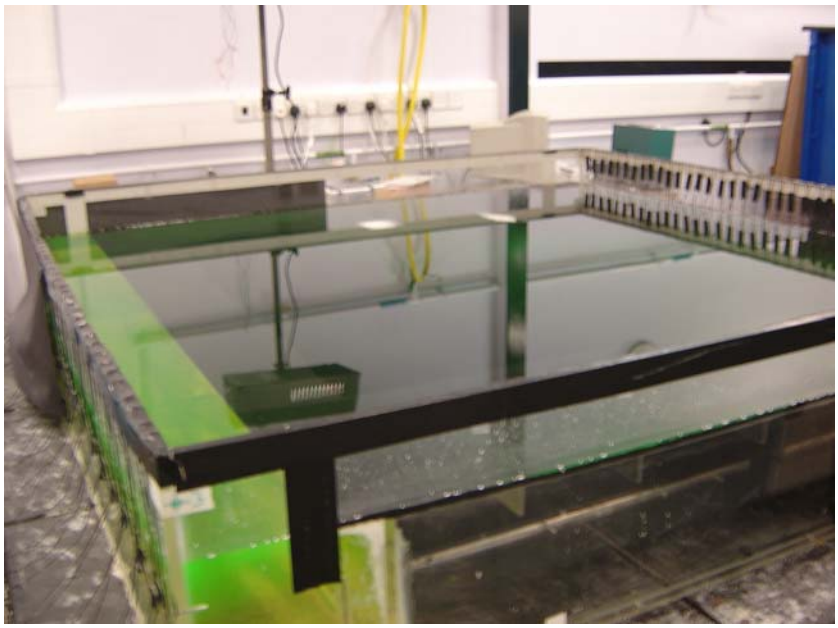

Figure. 3.5 Picture of the tank: the black adhesive tape on the edges of the vertical Perspex walls has the aim of reduce reflection of light coming from the lamps.

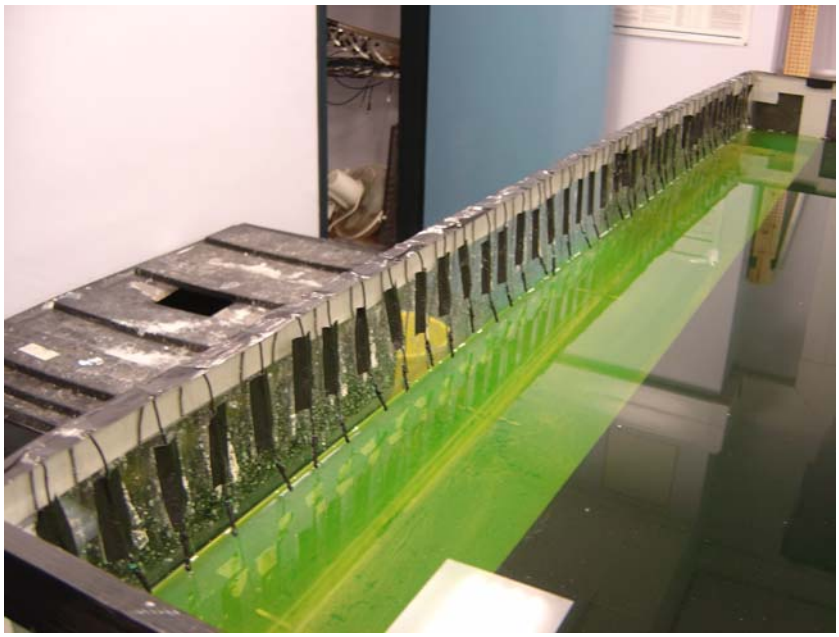

Figure. 3.6 Picture of one of the two sides of the tank covered with the platinum electrodes.

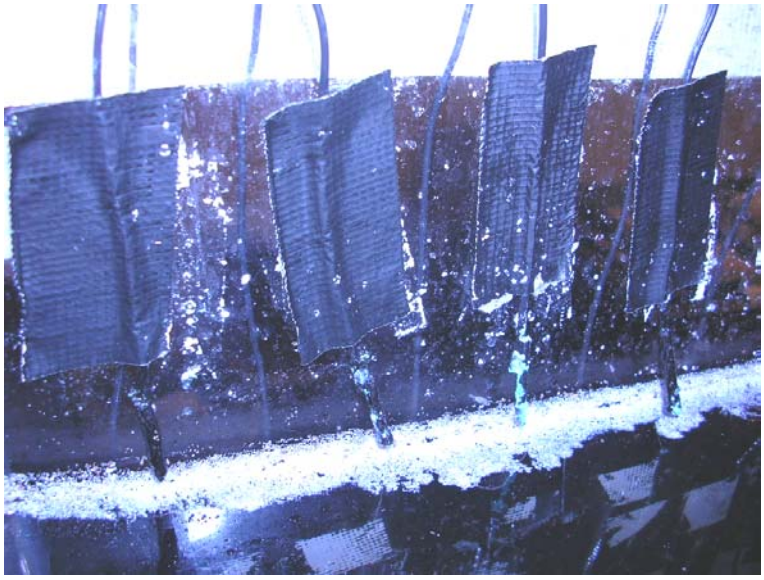

Figure. 3.7 Picture of the platinum electrodes.

3 COMPONENTS OF THE EXPERIMENTAL SETUP

In this section, a more detailed description of some components of the experimental setup will be given in order to permit to properly reproduce the experiments if needed. In particular, the different kinds of particles tested will be described in section 3.1, together with the reason for the choice of the type used in the experiments and with some brief evaluations of the difference between the velocity of the particles and the actual velocity of a fluid element; some details concerning the camera equipment will be given in section 3.2; the calibration plate will be shown in section 3.3; the electrical equipment used to generate the electrical signal for the forcing of the brine will be the topic of section 3.4.

3.1 Particles

Many different kinds of particles have been tested before to choose the one better suitable for this experiment. The first kind of particles were polystyrene pearls with a diameter of one eighth of inch (corresponding to 3.175 mm) and with medical finish: their advantages were an almost perfect spherical shape and the fact that all the particles have exactly the same size and shape but, on the other side, they were too large if compared to the smallest scale of the forcing (10 mm) and to the thickness of the brine layer (5 mm) and not so bright to the camera eye; moreover, the large diameter caused many issues concerning clustering of particles, so the hypothesis of using them was ruled out.

Then, particles of Plioliite VTCAL, sifted to have a diameter between 1 and 2 mm, were tested: they were more bright and caused less clusters than medical polystyrene balls but, on the other side, they were too irregular in shape and with the tendency to orient themselves in the flow: this could add a rotation of the barycentre that could consequently cause false acceleration measurements.

Later, some raw polystyrene particles of 0.5 mm were tested and they resulted too little bright. Anyway, these particles have the characteristic of increase their size when immersed in hot water, so they were enlarged by putting them for 3 minutes in a cup of

boiling water, to finally reach a maximum diameter of less than one mm. These particles were used in the first campaign of measures with PTV (Particle Tracking Velocimetry, see section 3 of chapter 4) as they turned out to be very bright on picture but, in order to avoid clustering, their density was kept relatively low (around 600 particle per meter square were identified by PTV codes).

Finally, to try having a higher insemination density, particles of Chemigum P83 (a kind of white powder with single particles having a range of diameters between about 100 to 600 μm and a density of 1.03 compared to fresh water) were tested and, as they were bright enough on pictures, they were used to have a density of around 800 particle per square meter.

In order to reduce the static electricity of the particle and so their tendency to cluster, three drops of a wetting agent containing Ethylene Glycol for photographic use (Kodak Photo-flo) were added to the brine on before each day of experiments.

These particles are slightly lighter than brine so, to a first approximation, they can be considered neutral to the two dimensional flow.

To understand if the velocity measured via PTV, that is the velocity of the particles (what is measured), was close enough to the velocity of the fluid elements (the required measure), a brief review of the literature on this topic was carried out. Adrian (1991) and Melling (1997) give applied relations between the acceleration of a particle and the velocity lag, ($\vec{v} - \vec{u}$), for gaseous flows (high ratio between the density of the particles and the one of the fluid), where $\vec{v}$ is the velocity of the particle and $\vec{u}$ is the velocity of the fluid flow. This relation had been modified by Virant and Dracos and applied to a water flow in a laboratory flume: they stated that, when the following condition is verified,

$$\|\vec{a}\| \leq 0.36 \frac{\upsilon \|\vec{u}\|}{D_P^2} \frac{\rho_F}{\rho_P} \qquad (3.1)$$

(where $\vec{a}$ is the acceleration of the particles, υ the kinematic viscosity of the fluid, $\vec{u}$ the velocity of the particles, D_P their diameter, ρ_P their density and ρ_F the density of the fluid), the velocity of the particles deviates from the velocity of the fluid elements by 1%. Following this equation and considering that in the present case the ratio

$$\frac{\upsilon}{D_P^2} \frac{\rho_F}{\rho_P} \cong 1, \qquad (3.2)$$

the measured Eulerian fields of velocity and acceleration, whose description is given in section 5.1, have been used to compute the expected percentage error in the velocity measurement between the particle and the actual fluid velocity, equal to

$$error = \frac{\|\vec{a}\|}{0.36\|\vec{u}\|} \qquad (3.3)$$

whose spatial distribution is reported in Figure 3.8.

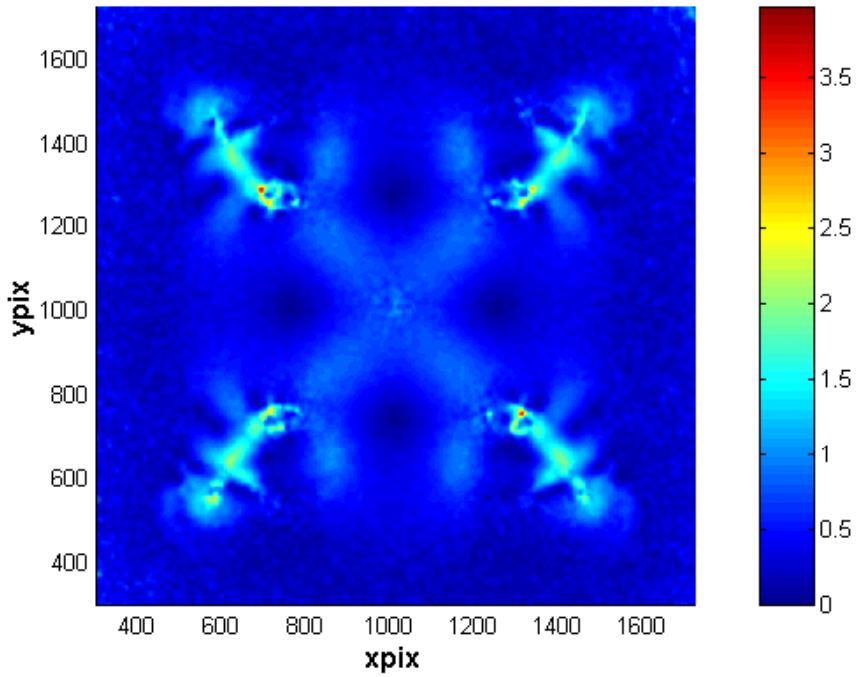

Figure 3.8 Percentage error on the velocity of the particles to the fluid velocity according to equation 3.3; 1mm is about 2.02 pixels, the mesh is of 600x600 points with a mesh's size of 3 pixels.

Using equation 3.1, the percentage error results always fewer than 4% but, for the largest part of the flow, well under 1%.

3.2 Camera

The camera system used to shoot the experiments is an Imager Pro Plus camera system (by LaVision company), whose fundamental components are a camera with a digital image output, a separate camera control unit and a dedicated personal computer with the DaVis software for data acquisition and data processing.

The core of the system is the Imager Pro Plus 4M camera (see Figure 3.9), a 2 monochrome ADC high definition camera (2048 x 2048 pixel^2 and a 14 bit depth corresponding to 16384 grey levels). A PTU unit installed in the dedicated computer triggers the recording of the camera. The acquisition frequency with the maximum definition was tested with the datalogger and it was found that the maximum operational frequency is of 14 Hz of 2800 microseconds and of 13 Hz with an exposure time of 8900 microseconds. The CCD image sensor in the camera system is thermoelectrically cooled by a Peltier cooler. The camera supports 2 different acquisition modes. The first one, “memory recording”, allows image recording at the camera data rate: the digitized images are stored within the camera memory. The second one, “direct data transfer”, forces the camera images to be directly transferred to the PC memory: this second mode was used during the experiments.

The camera exposure may be controlled by external trigger and enable/disable signals: these signals must be feed into the BNC sockets on the back panel of the external camera control unit (see Figure 3.10). The camera signals coming out from the external

camera unit were sent to the datalogger through the amplifier (see section 3.4).

Figure 3.9 The Imager pro Plus camera by LaVision Company used in this work.

Figure 3.10 The external camera control unit by LaVision Company.

3.3 Calibration plate

The calibration plate is a plate made of white plastic with the position of the magnets marked on it (see Figure 3.11): it was leant on the horizontal wall supporting the brine and positioned in a way to give the approximated position of the magnet. It is useful to both places the camera in the correct position, in order to take pictures only on the desired investigation field. After that the camera was in the correct position, few pictures (usually three) of the calibration plate were shot: these picture were then used to check if any mistake was made in positioning the camera and to compute the conversion coefficient to convert data from pixels to millimetres.

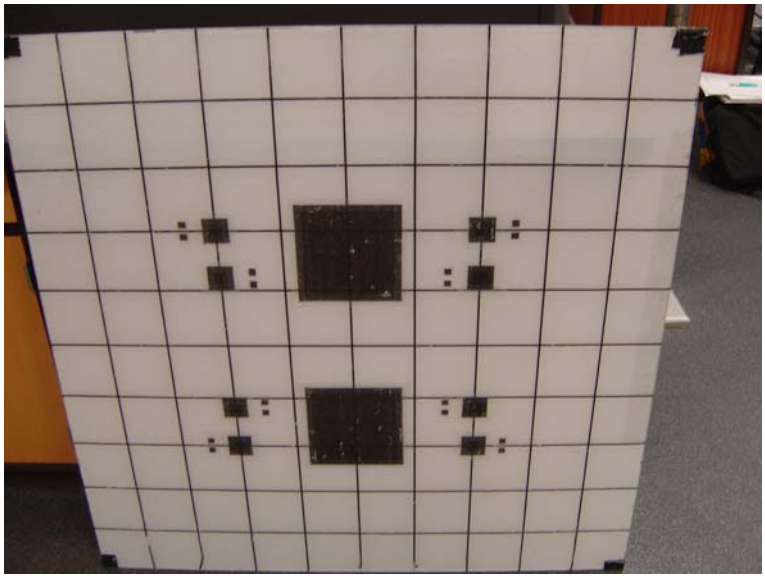

Figure 3.11 Picture of the calibration plate with the position of the magnets.

3.4 Electrical equipment

A complex electrical apparatus was used to generate the electrical signal for the experiments: also if the results object of this work concerns only experiments with a constant electrical current, nevertheless experiments with a time dependent current were performed too and will be object of future investigations; so, the electrical apparatus was designed in order to generate a sinusoidal signal of various amplitude and period and to record it, to have the possibility to check, after each experiment, if the electrical signal had the desired characteristics. The main components of the electrical apparatus will be briefly described in the following paragraphs: each component was tested for accuracy before performing the experiments.

3.4.1 Datalogger

The datalogger (by Picotech company) used in the experiment is an electronic instrument that records readings of voltage over time. It is a small device that is equipped with a microprocessor with memory for data storage received from sensors. The datalogger records each reading and stores it in memory along with the acquisition time. It interfaces with a computer through software for viewing/storing the collected data. The sensors installed on the datalogger are used to record the time dependence forcing from the power supply and the camera signals. The datalogger was tested for its limitation and the validation of the recorded data was checked. A driver installed in a computer triggers the data recording. As previously stated, in the experiment with a time dependence forcing the electrical signal has a sinusoidal shape: the repeatability of this sinusoidal signal have been checked and verified to be consistent for each set of recording.

Figure 3.12 Picture of the datalogger (by Picotech company).

3.4.2 The Picolog adapter

This device is shown in Figure 3.13, the Electrical and Electronics Services of the Department of Aeronautics of the Imperial College London home make it. The two ports of the adapter are designed to allow the datalogger measuring the input current from the power supply to the tank. Since the datalogger only works with a maximum voltage input of 2.5 V, the resistors plugged in the adapter can be used to limit the current flow. With different resistors, the limiting current can be altered for the desired range.

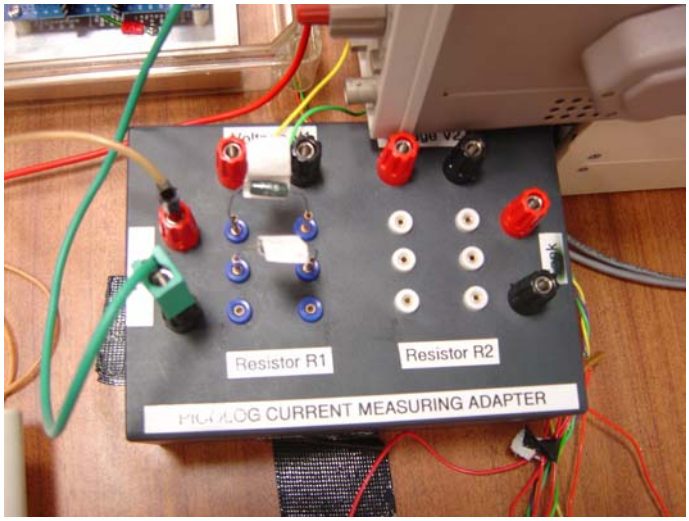

Figure 3.13 Picture of the homemade Picolog adapter.

3.4.3 Amplifier circuit box

This amplifier circuit box is shown in Figure 3.14: it is home made by the Electrical Laboratory of the Department of Mechanical Engineering of the Imperial College London and it is designed to convert high voltage input (± 25 V) into low output (± 1.5 V).

It allows summing of the signal input from the function generator and input from the power supply. The gain resulted from the summing is performed by series of power amplifiers. There are three OPA27 and one OPA541 power operational amplifiers in the circuit. The latter power amplifier has a heat sink for dissipating heat. There are specified resistors to limit the current. The offset control located below the OPA27 power amplifiers allows a ± 5 V offset of the output. The output of the amplifier is connected to the input plugs of the Picolog current measuring adapter.

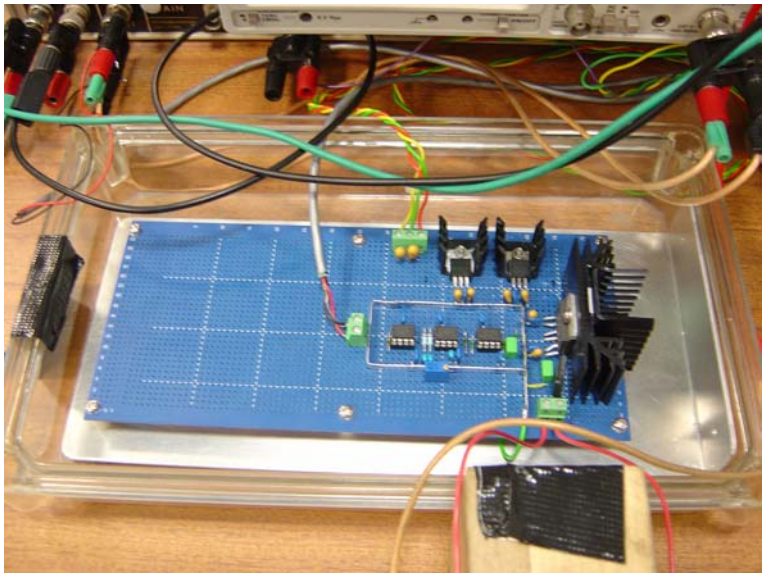

Figure 3.14 Picture of the home made amplifier circuit box

3.4.4 Power supply

This device generates the current signal that goes to the tank. A dual channel power supply was used in the experiments. It is connected to the amplifier circuit box through some wires.

Figure 3.15 Picture of the homemade power supply.

3.4.5 Multimeter

Two multimeters (TTi 1705 True rms programmable multimeter, see Figure 3.16) were used to read the values of current and voltage during the experiments.

3.4.6 Oscilloscope

An oscilloscope (see Figure 3.17) was used to visualize the current signal. In the experiments, it was decided to start the recording at the minimum current.

3.4.7 Power amplifier and the function generator

There are four channels available in the power amplifier (see Figure 3.18): each one of them provides the gain and offset control of the input voltage. In the experiments, the input of the channel 1 is connected to the function generator and its output to the amplifier circuit box; input of the channel 2 is connected to the camera, so that the offset and the amplitude of the camera signal could be varied. The output of channel 2 is linked to the sensor two of the datalogger.
A function generator (TWG501, see Figure 3.19) able to generate different mode shapes of time-period current was used: the shape of the signal can be a triangular, square or sinusoidal one. As already stated, the sinusoidal shape was used in this experiment. The amplitude and frequency of the output signal can also be changed by adjusting the setting of the device.
The amplifier was needed to amplify and change the offset of the time period current, so that the input current of the sensor was limited within 0 and 2.5 V. By using the datalogger, the voltage readings of the current are recorded and the data is analysed in an Excel worksheet. The repeatability of the current generated by the generator was checked and verified. The frequency of the time-period forcing required in the experiment wais targeted at around 0.066 Hz. Therefore, all the tests were made by setting the frequency of the output current to be lower than 0.1 Hz. The errors of the maximum and minimum peaks of the periods were found to be less than 0.1%.
The main connections in this section of the electrical apparatus were the following: the dual channel power supply was connected to the amplifier circuit box; the function generator was also connected to the circuit box through the amplifier; the Picolog current measuring adapter was connected to the circuit box and to a resistor with a resistance similar to the one of the tank.
During the tests to check the repeatability of the current generated by this apparatus, it was found that the standard deviation of periods is descending, as the amplifier circuit box tends to warm up. It was so decided to switch on the circuit box some hours earlier (at least three) before taking measurements in the experiments.

Figure 3.16 Picture of the TTi 1705 True rms programmable multimeter

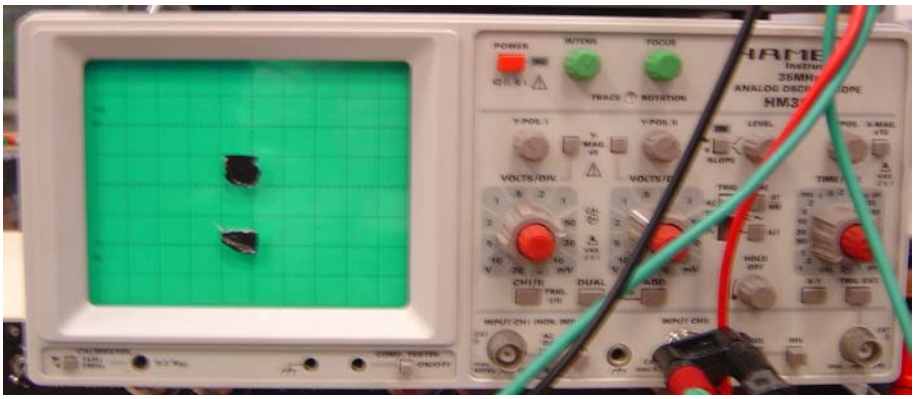

Figure 3.17 Picture of the oscilloscope.

Figure 3.18 Picture of the power amplifier.

Figure 3.19 Picture of the function generator TWG 501

4 MAIN EXPERIMENTAL PROCEDURES

Some procedures had to be followed in order to grant the accuracy of the measurements: the most important ones are briefly described in the following three paragraphs and concern the measurement of the horizontality of the brine supporting wall and of the brine layer thickness, the measure evaporation rate, the check of the Ohm's law for the brine layer and the warm-up procedure to stabilize the electrical apparatus.

4.1 Measurements of the horizontality of the brine supporting wall, of the thickness of the brine layer and of the evaporation rate

The measurement of the horizontality of the brine supporting wall and of the brine layer thickness, as well as the measure evaporation rate were carried out using a meter tool (see Figure 3.20) giving the measures with a precision of one hundred of inch (equivalent to around 0.254 mm).

The horizontality of the brine supporting wall is adjustable, via 18 sustains placed beneath, of one tenth of millimetre adding or removing some paper sheets from/to the sustains. The bottom wall of the tank was adjusted, by checking the standard deviation of the water thickness, until the maximum deviation from the mean value of depth was under 0.2 mm.

The water thickness on the surface of the inner broad of the tank is set to be 5mm for the purpose of the experiment. To meet this requirement, the water thickness is measured via the meter tool in 49 points of measure over the investigation area. A marked pinewood is used to locate the 49 points when taking the measurements. The brine layer thickness measurement is repeated until the mean and the standard deviation are satisfied. The measured thickness of the shallow brine layer during the experiments was about $H = 5.009 \pm 0.121$ mm.

Measurements of the brine layer thickness after known time intervals were taken too, in order to evaluate the evaporation rate: it was found the evaporation rate to be of about 0.3÷0.4 mm/day, low enough to not alter the depth too much during measurements (less than six hours, so a reduction of the brine layer thickness of less than 0.1 mm was expected during the first and the last run of the experiments).

Figure 3.20 Picture of the meter tool used to check the horizontality of the brine supporting wall and the thickness of the brine layer.

4.2 Measurement of the Ohm's law

As the readings from datalogger are in voltage, a calibration to convert the voltage data into current ones was required, to compute the time dependence forcing: this means that the Ohm's law of the current passing through the resistor represented by the layer of brine was needed. In order to do that, the thickness of the brine layer was adjusted to a value very close to 5 mm (4.998 ± 0.112 mm), then the components of the experimental setup were prepared like for the actual experiments (except for the function generator that, in order to have a constant current, was switched off) and the power supply was switched on starting from very low values of voltage. The two multimeters were used to measure the current crossing the tank and the linked voltage. A broad range of values was measured covering all the field of interest. On Figure 3.21, the data of voltage and current are reported, with the straight line that best fit the data in a least mean square sense. The resulting Ohm' law for the brine layer was found to be $V = 13.102\ I+3.445$, so the resistance was R = 13.102 Ω. As the relation between resistance R and conductivity σ is $\sigma = l / (RA)$, with l = length of the conductor = 1.7 m, A = section area of the conductor = $1.7 \cdot 0.005$ m^2, the conductivity of the brine layer can be obtained: it was found σ = 15.26 S/m, a value close enough to the value of 16.58 S/m for a brine with the same concentration of 158.38 kg/m^3 that can be found in chemical handbooks.

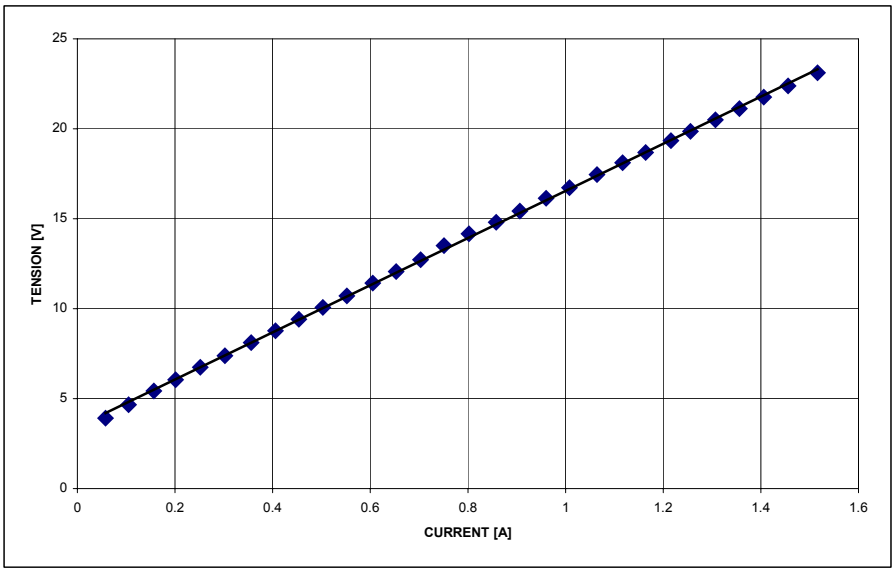

Figure 3.21 The Ohm's law for the brine layer used in the experiments

4.3 Electrical system warm-up

As previously stated, from the tests done to check the repeatability of the current generated by the signal generator, it was found that, in order to maximize the repeatability of the electrical signal, the electrical apparatus had to be switched on some hours earlier before taking measurements in the experiment. To do that, a resistor with a resistance similar to the one of the tank was connected to the Picolog current measuring adapter, to then switch the dual channel power supply on, in order to keep the amplifier circuit box running for at least three hours. After three hours, the resistor was plug out and the electrical apparatus was connected to the tank. During the first ten minutes, the amplitude of the current forcing was decreasing, because of the chemical reactions occurring in the tank, to then become stable after 10 minutes. The tank was so ready for a new campaign of experiments.

4.4 Shooting of the dark image

When everything in the experimental setup was adjusted and the electrical apparatus warmed up, just before to start shooting the experiments the dark image of the camera was taken: it is a picture taken with the lens cup on and with switched off lamps, that so can give a measure of the electrical noise of the camera. This dark image can be subtracted from each picture of the experiments to remove part of the background, directly by the camera during the experiments or, as this process reduces the camera performances, during the post-processing of the picture. The dark image is obtained as an average over 100 images taken under the mentioned conditions.

5 EXPERIMENTS

Two main type of experiments were carried out, with a constant forcing and with a time dependent one: in particular, two series of runs with a constant forcing (with two different investigation fields) and seven series of runs with a time dependent one (with

various periods and amplitudes of the current) were performed.

5.1 Constant Forcing

A total number of 133 runs with a constant forcing (a current of 0.53 A and a voltage of 10.2 V) were carried out using two different investigation fields, one larger than the other.

110 runs over an investigation field of 1015.4 x 1015.4 mm^2 were performed to measure the entire flow, during four days of measurements on February 2005. The camera exposure time was set to 10000 μs, with an acquisition frequency of 10 Hz. 1200 images were taken for each run (120 s), starting from the flow at rest and so shooting pictures of the transient too: the transient was found to be of around 20 s, so more than five turnover times of the integral length scale (around 19.2 s, see Rossi et al., 2006a) where recorded.

23 runs with the same constant forcing but over a smaller investigation field (842.1 x 842.1 mm^2) were carried out so as to increase the resolution at the small scales on March 2006. During the period between the first and this second campaign, the camera was shipped back to the manufacturer in order to solve some problems discovered during data analysis (see sections 6.2 and 6.3). The camera parameters were the same as for the previous measurements, except for the number of pictures (1000): as in this second series the pictures were recorded with the flow at regime, they were enough to have, also in this case, more than 5 turnover times of the integral length scale.

Three of the runs with the largest investigation frame were discarded because there were too many lost images by the camera (see section 6.2), leading to a total number runs with a constant forcing of 130.

5.2 TD forcing

The results reported in the chapter 5 this work come from the analysis of the experiments with a constant forcing: nevertheless, some series of experiments with a time dependent forcing were carried out and kept for future work.

The introduction of this new class of turbulent-like flows with a time dependent forcing can be considered as another brick added to try rebuilding the wall of turbulence, as explained in the previous chapter 2. From some preliminary visualization with dye (fluoresceine), it was noticed that the introduction of a time dependent forcing induces unsteadiness in the flow: for example, the vortices living for all the time of the experiment in the flow with constant forcing tend to break down after some time in the time dependent flow, increasing the mixing. Indeed, the mixing process in the flow becomes more complex than in steady flow. One of the target of the time dependent flow is also to identify the relationship between the temporal characteristics and spatial characteristic of the flow, that is how the time dependent forcing influences the flow topology, the stagnation points and the streamlines.

A first preliminary campaign was carried out with a sinusoidal current with a period of 15 s, an amplitude ΔI of 0.505 A, a minimum current 0.155 A, a maximum current 0.660 A and a mean value of 0.408 A. 60 runs were recorded during three days, with a camera exposure time of 8900 μs, an acquisition frequency of 13 Hz and 1950 images taken for each run (19.5 s, in order to have 10 periods of the forcing). The forcing data of these 60 runs are shown in Table 3.1.

Run	Average Voltage [mV]			Average Current [A]			Average Periods [s]	STD [%]
	Min	Max	Mean	Min	Max	Mean		
1	581.9	2471.9	1517.4	0.1548	0.6580	0.4039	15.0526	0.017
2	581.0	2475.8	1518.9	0.1546	0.6590	0.4043	15.0417	0.029
3	579.9	2484.6	1522.8	0.1543	0.6614	0.4053	15.0196	0.017
4	578.6	2489.4	1524.9	0.1539	0.6627	0.4059	15.0079	0.018
5	578.0	2494.5	1527.0	0.1538	0.6640	0.4064	14.9966	0.013
6	572.5	2495.2	1525.0	0.1523	0.6642	0.4059	15.0362	0.010
7	573.3	2482.5	1520.1	0.1525	0.6608	0.4046	15.0160	0.011
8	573.3	2493.0	1524.7	0.1525	0.6636	0.4058	15.0118	0.012
9	579.7	2481.0	1522.5	0.1542	0.6604	0.4052	15.0130	0.014
10	580.9	2487.8	1525.6	0.1545	0.6622	0.4061	15.0134	0.010
11	581.0	2485.0	1524.7	0.1546	0.6615	0.4058	15.0134	0.011
12	581.3	2485.7	1525.4	0.1546	0.6617	0.4060	15.0171	0.019
13	581.1	2484.0	1524.6	0.1546	0.6612	0.4058	15.0145	0.026
14	578.0	2476.7	1519.2	0.1538	0.6593	0.4043	15.0173	0.011
15	577.8	2473.3	1517.5	0.1537	0.6584	0.4039	15.0201	0.009
16	578.0	2472.1	1516.4	0.1538	0.6580	0.4036	15.0214	0.013
17	578.1	2480.3	1521.0	0.1538	0.6602	0.4048	15.0227	0.012
18	576.1	2476.9	1517.7	0.1533	0.6593	0.4039	15.0211	0.017
19	576.0	2468.5	1513.3	0.1532	0.6571	0.4028	15.0201	0.009
20	580.9	2493.5	1528.4	0.1545	0.6637	0.4068	15.0242	0.009
21	580.6	2481.1	1522.2	0.1545	0.6604	0.4051	15.0082	0.011
22	580.7	2483.5	1523.1	0.1545	0.6611	0.4054	15.0064	0.017
23	580.7	2485.1	1523.8	0.1545	0.6615	0.4056	15.0044	0.012
24	579.6	2485.7	1524.2	0.1542	0.6617	0.4057	15.0012	0.012
25	578.8	2485.3	1523.8	0.1540	0.6616	0.4056	14.9987	0.001
26	580.8	2479.1	1521.3	0.1545	0.6599	0.4049	15.0390	0.010
27	580.9	2478.1	1520.7	0.1545	0.6596	0.4047	15.0394	0.006
28	580.8	2479.1	1520.9	0.1545	0.6599	0.4048	15.0370	0.020
29	580.7	2478.9	1520.9	0.1545	0.6599	0.4048	15.0361	0.009
30	580.2	2477.6	1519.8	0.1543	0.6595	0.4045	15.0353	0.010
31	580.0	2476.0	1518.8	0.1543	0.6591	0.4042	15.0394	0.010
32	579.6	2474.3	1518.1	0.1542	0.6586	0.4040	15.0371	0.021
33	578.0	2468.0	1514.8	0.1538	0.6570	0.4032	15.0397	0.022
34	575.5	2477.3	1517.9	0.1531	0.6594	0.4040	15.0152	0.007
35	575.5	2477.2	1517.9	0.1531	0.6594	0.4040	15.0175	0.010
36	576.0	2476.5	1517.8	0.1532	0.6592	0.4040	15.0180	0.017
37	577.6	2483.0	1521.5	0.1537	0.6609	0.4050	15.0188	0.011
38	575.5	2476.2	1517.5	0.1531	0.6591	0.4039	15.0157	0.033
39	577.3	2484.6	1522.1	0.1536	0.6614	0.4051	15.0152	0.034
40	576.1	2482.1	1520.6	0.1533	0.6607	0.4047	15.0165	0.011
41	576.0	2480.4	1519.8	0.1532	0.6603	0.4045	15.0108	0.011
42	576.0	2481.7	1519.5	0.1532	0.6606	0.4044	15.0033	0.010
43	574.7	2480.1	1518.7	0.1529	0.6602	0.4042	14.9942	0.022
44	573.0	2471.2	1513.5	0.1524	0.6578	0.4028	15.0222	0.017
45	572.6	2471.0	1513.2	0.1523	0.6578	0.4027	15.0219	0.007
46	574.9	2471.6	1514.0	0.1529	0.6579	0.4030	15.0175	0.020
47	572.8	2473.6	1514.5	0.1524	0.6584	0.4031	15.0126	0.015
48	577.2	2493.3	1525.7	0.1535	0.6637	0.4061	14.9995	0.007
49	578.0	2492.8	1525.6	0.1538	0.6636	0.4061	15.0219	0.001
50	577.4	2491.2	1525.1	0.1536	0.6631	0.4059	15.0203	0.012
51	575.8	2485.0	1521.3	0.1532	0.6615	0.4049	15.0196	0.013
52	572.7	2476.4	1515.4	0.1523	0.6592	0.4033	15.0116	0.011
53	574.5	2479.2	1517.7	0.1528	0.6599	0.4040	15.0054	0.007
54	575.4	2478.9	1517.9	0.1531	0.6599	0.4040	15.0067	0.014
55	573.8	2478.5	1517.5	0.1526	0.6598	0.4039	15.0057	0.008
56	579.6	2484.9	1522.9	0.1542	0.6615	0.4053	15.0014	0.007
57	580.9	2489.6	1525.9	0.1545	0.6627	0.4061	14.9991	0.009
58	581.0	2484.6	1523.7	0.1546	0.6614	0.4055	15.0296	0.009
59	580.6	2479.5	1520.7	0.1545	0.6600	0.4047	15.0304	0.010
60	580.0	2478.3	1520.3	0.1543	0.6597	0.4046	15.0301	0.024

Table 3.1 Forcing data of the 60 runs of the first campaign with time dependency.

In order to chose the parameters of the time dependent forcing for the second campaign, the expected time scales of the three scales of forcing were computed as the ratio between the integral length scale and the root mean square of the velocity (taking data from a previous campaign, see Rossi et al., 2006a), see Figure 3.22: as these curves, together with the line that shows where the bottom friction becomes no more negligible, identify six zones, it was decided to force each zone while keeping constant the value of $\Delta I / I_{mean}$. Data of the forcing are reported in Table 3.2: in particular, the forcing current of series 1 and 2 is under the limit of the bottom friction and between medium and large scales, the forcing current of series 3 is under the limit of the bottom friction and between the small and medium scales, the forcing current of series 4 and 5 is above the limit of the bottom friction and between medium and large scales and, finally, the forcing current of series 6 is above the limit of the bottom friction and above the large scales. 1800 pictures were taken for each run (in order to have at least 10 periods), with an exposure time of 10000 μs and an acquisition frequency of 12 Hz. Also if these data still have to be analysed, different interactions among the scales were spotted, during the experiments, for different forcing.

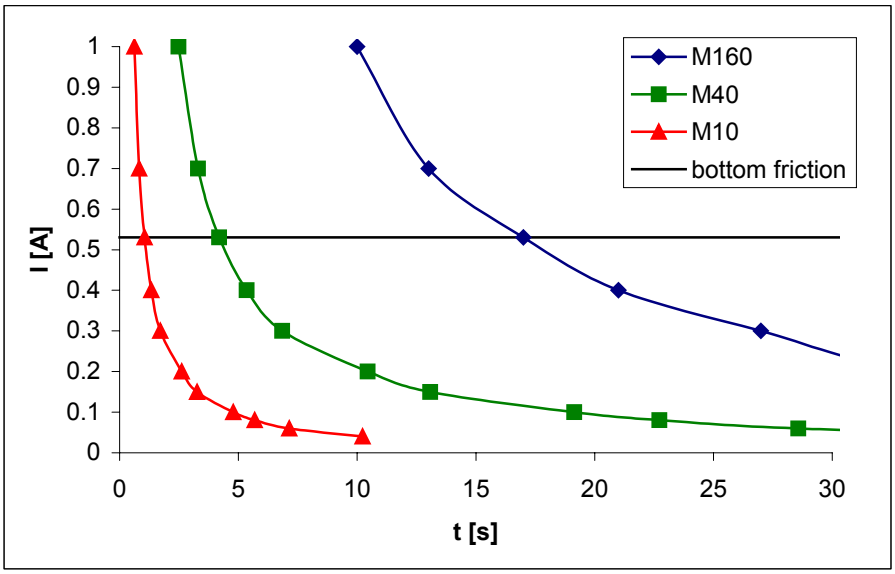

Figure 3.22 Expected time scales of the three scales of forcing *t* versus current *I*; M160, M40 and M10 refers to the magnets' size; the black straight line identifies the current value over which the bottom friction is no more negligible.

Series	Period [s]	I min [A]	I max [A]	I mean [A]	ΔI [A]	ΔI / I mean
1	5	0.258	0.408	0.333	0.15	0.45
2	5	0.581	0.919	0.75	0.337	0.45
3	10	0.258	0.408	0.333	0.15	0.45
4	10	0.581	0.919	0.75	0.337	0.45
5	15	0.326	0.5145	0.42	0.189	0.45
6	15	0.647	1.023	0.835	0.376	0.45

Table 3.2 Mean forcing data of the 6 series of the second campaign with time dependency.

6 POSTPROCESSING

After that pictures of the experiments were taken, some postprocessings were needed for many reasons and, in particular, in order to increase the quality of the PTV codes' particle detection (see section 3.2 of Chapter 4), to identify the best particle parameters to give as an input to the PTV codes, to reduce the size of the data for storing purposes and to solve some issues arising from the camera equipment.

6.1 Image post-treatment

The first picture postprocessing code was written in order to enhance the contrast between the particle and the background (so allowing a reduction of the background noise and a better particle detection), to solve an issue arising from one of the PTV codes used (DigiFlow, see section 3 of chapter 4) and to reduce the size of the data to store. The issue with DigiFlow concerned the identification of more than one barycentre over each particle: to solve this problem, it was decided to give as an input to DigiFlow black and white pictures. This actually solved the problem with DigiFlow, with the drawback of a little increase of the measurement noise.

The bit depth of the pictures were initially reduced from 14 bit (see Figure 3.23) to 8 bit (see Figure 3.24) applying on the raw picture a double threshold (values below a threshold went to zero, values above 255 went to 255); this allowed to largely reduce the background noise and to highlight the particles. Finally, a smoothing filter was applied and black and white pictures (see Figure 3.25) were obtained by applying a simple threshold (binarization). The smoothing filter worked in this way: for each pixel of the original image, the mean value of the light intensity over a window (with a five pixel facet and centred over the pixel under investigation) was put in place of the original value.

All the thresholds were adaptive according to the light intensity of each picture on the strength of the following equation:

$$threshold = mean + n \cdot std \qquad (3.4)$$

This allowed taking into account changes in the light intensity. In particular, for the first threshold n was equal to three, for the binarization n was equal to two. The smoothing window's size was 5.

To give an example of the reduction in size of the data to handle, on the run 24 of the first campaign of experiments (see section 5.1), a compressed 14 bit raw picture had a size of about 3 MB (so around 3.5 GB for the whole run, 1200 pictures), whilst one compressed 8 bit had a size of about 48 KB (around 54 MB for the whole run) and one compressed black and white picture of around 24 KB (around 23 MB for the whole run).

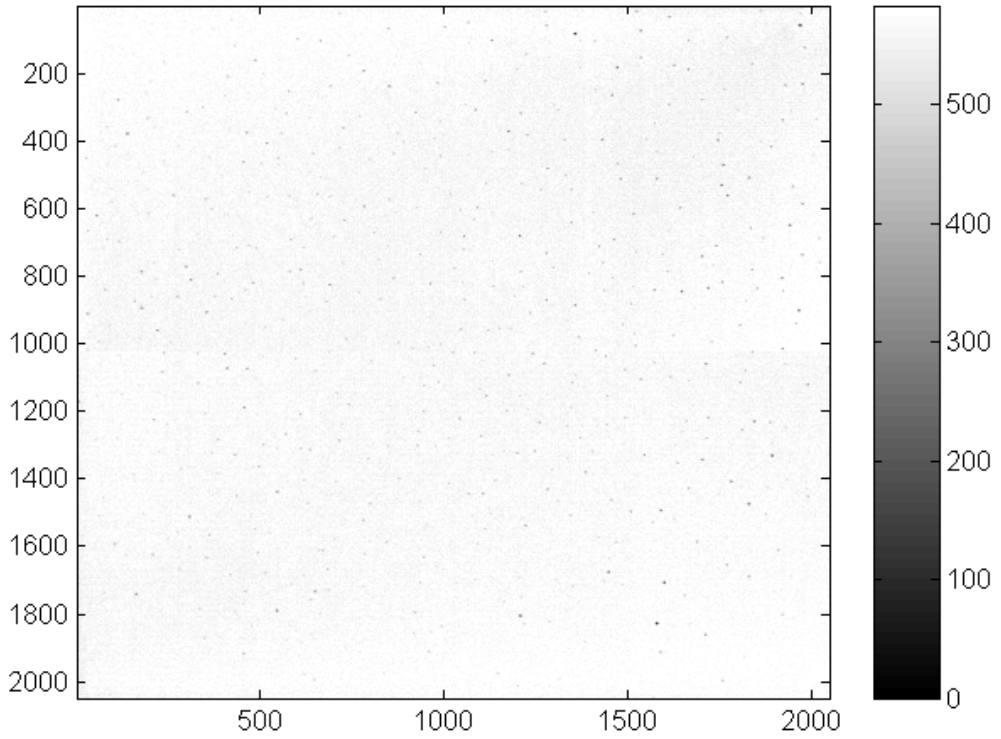

Figure 3.23 Example of the negative of a raw 14 bit picture from the camera; coordinates are in pixel, 1mm is about 2.02 pixels.

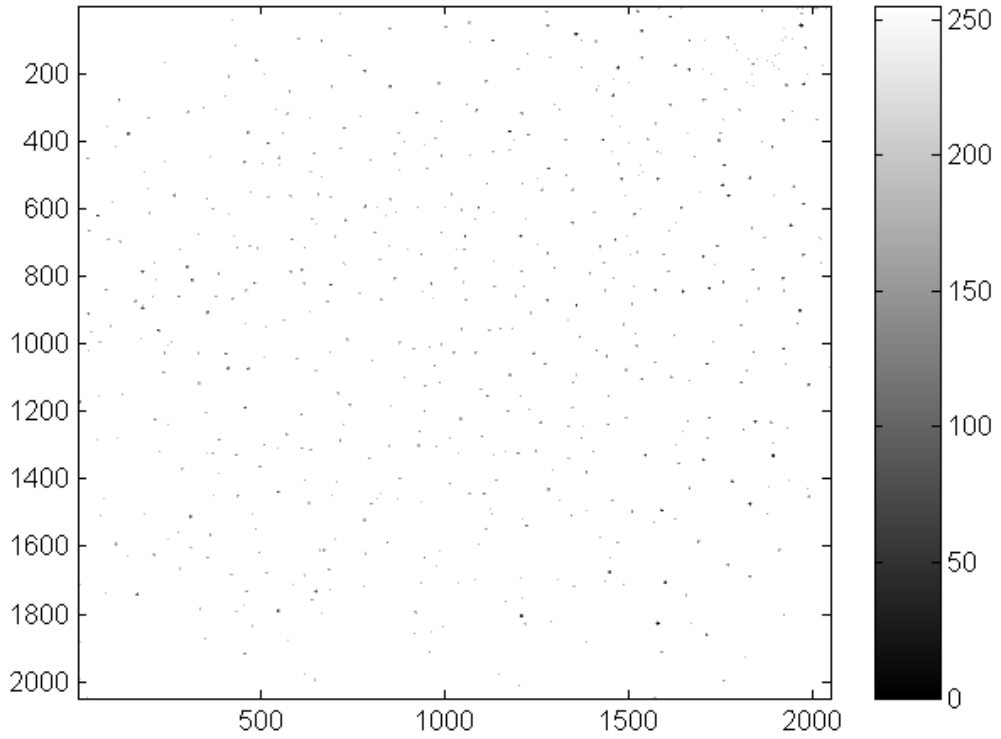

Figure 3.24 Example of the same picture of Figure 3.23 with a bit depth reduced from 14 to 8 bit; coordinates are in pixel, 1mm is about 2.02 pixels.

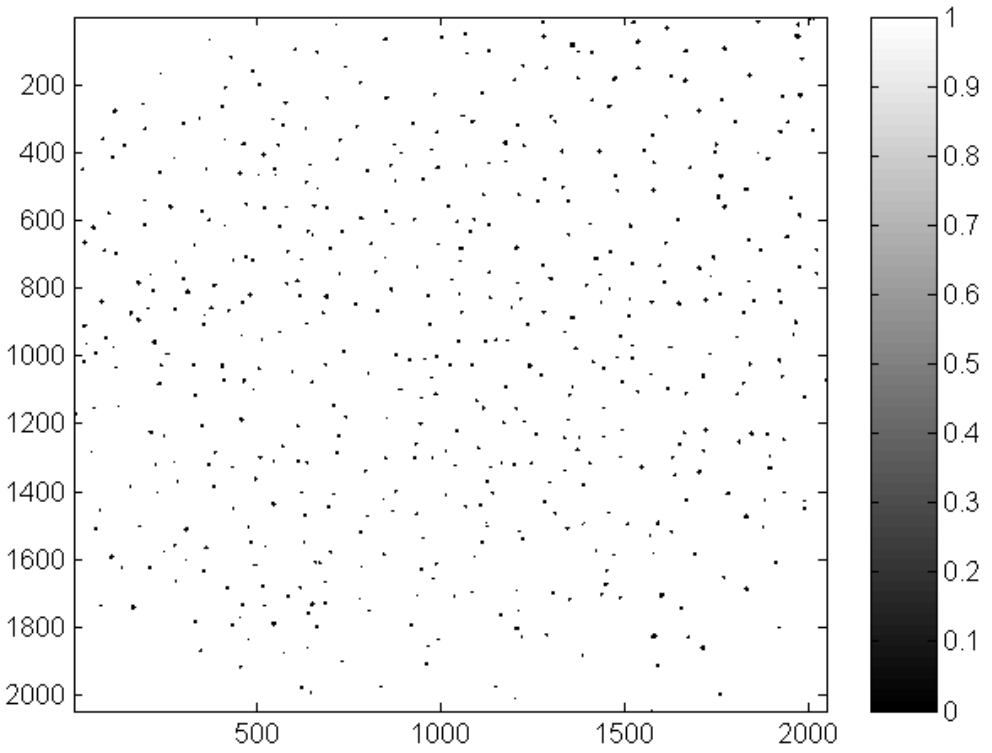

Figure 3.25 Example of the same picture of the previous two Figures reduced to a binary (black and white) picture; coordinates are in pixel, 1mm is about 2.02 pixels.

6.2 Lost of pictures

Due to a problem with the fast storage mode used during the experiments (see section 3.2), the camera failed time to time to store images: as this problem was discovered during the data analysis after the first campaign of measurements with constant forcing (see section 5.1), in which 110 experiments were taken, in order to not throw away this big amount of data, a code to detect where images were lost was written.

In order to automatically do that, this code computes initially the raw kinetic energy of the flow (namely, the sum of the particles displacements, that are proportional to the velocities, divided by the number of particles): this has an almost constant value (after the initial transient, because in the first campaign experiments started with the flow at rest) which, when one picture went lost, doubles for one time step to then come back to the initial value in the next time step (see blue lines on Figure 3.26). As the flow is stationary, the value of this raw kinetic energy should be almost constant (the small fluctuations on the raw kinetic energy appear because it is computed on the tracked particles, which enter and exit the investigation windows and have a not perfectly uniform spatial distribution, and because of the measurement noise), a sudden doubling of its values points out that the time interval between two images is twice the usual one (i.e., the camera failed to record one image). The code performs a median filter on the raw kinetic energy, using 31 positions (green lines on Figure 3.26), then computes a threshold curve (red lines on Figure 3.26) as 1.2 times the filtered raw kinetic energy and creates a vector with the time interval from one picture to the next one: when the raw kinetic energy is under the threshold, the time interval is the usual one (0.1 s), when it is

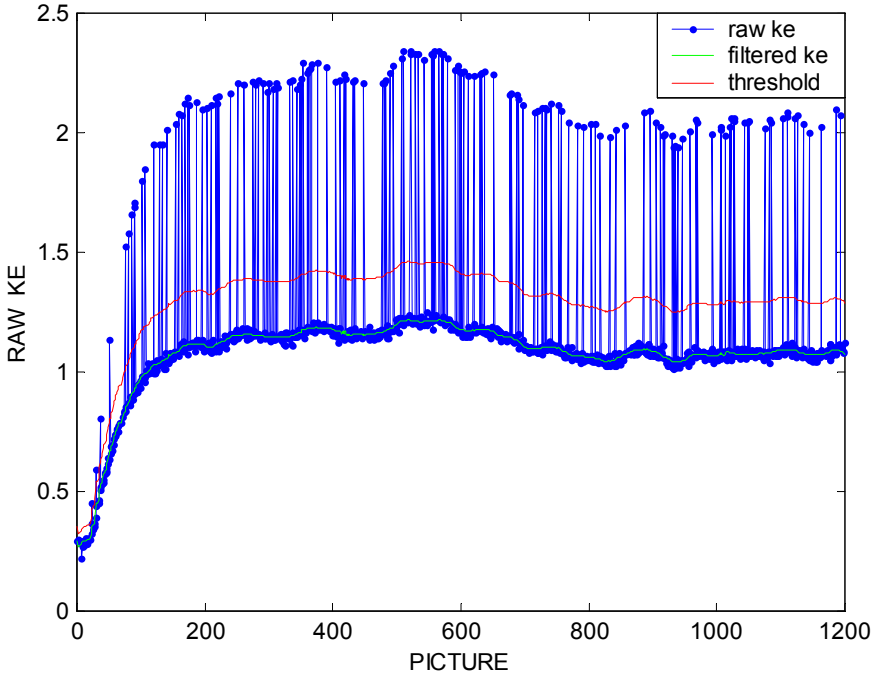

Figure 3.26 The raw kinetic energy (blue line), on run 37 of the first campaign of measurements, together with its filtered value (green line) and with the threshold curve (red line): values of the raw kinetic energy above the threshold point out that one picture was not recorded by the camera (the time interval between two consecutive pictures is twice the usual value).

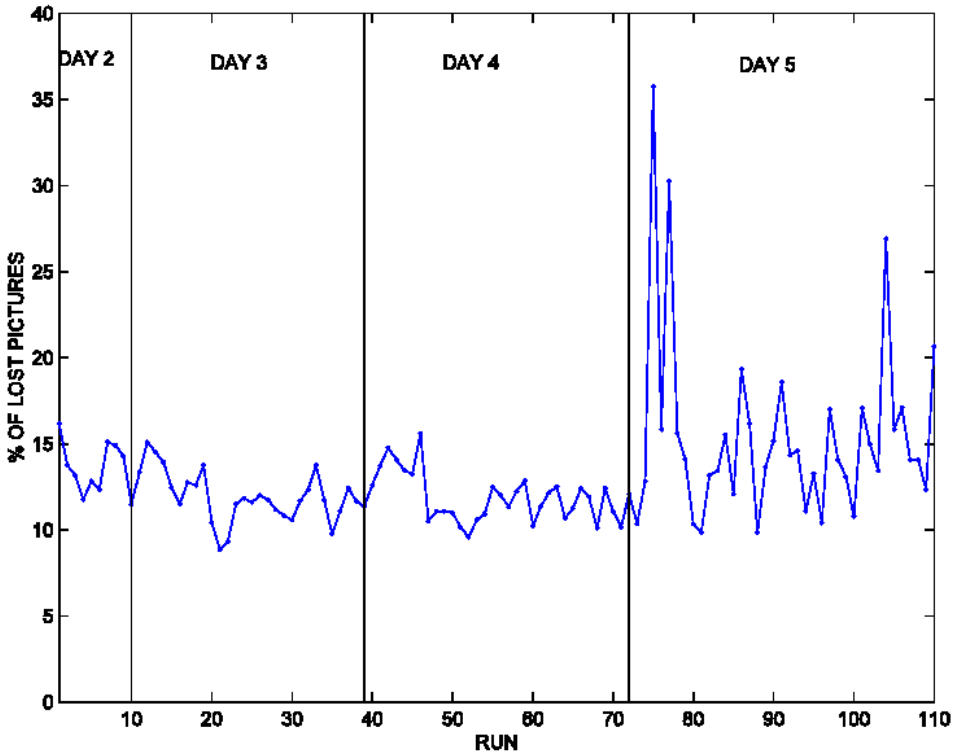

Figure 3.27 Percentage of pictures lost from the camera during the first campaign of experiments (110 runs during four days).

above, the time interval is 0.2 s. In order to allow PTV codes tracking trajectories, a larger investigation radius was used (see section 3.3 of chapter 4) and then the PTVA code (see section 4 of chapter 4) was fed with the vector containing the variable time intervals between pictures instead of constant ones (as it would have been done without camera failures).

Figure 3.27 shows the percentage of lost picture during the first campaign of experiments (the camera was shipped back to the manufacturer and repaired before the second campaign) for the various runs: as in run 75, 77 and 103 this percentage was too high, they were not taken into account for the subsequent measures.

6.3 1-pixel displacement

Another issue aroused from the camera: pictures were sometimes moved in the y-direction of exactly one pixel, like if the camera was moved of exactly one pixel in that direction before an image was shot to then be moved back in the initial position. It was found out later by the manufacturer that it was a problem with the camera firmware. This problem was corrected writing a code that moved the particles' y-coordinate down of one pixel when the mean value of the displacements in the y direction (blue line on Figure 3.28) was not almost zero (as the flow is symmetric and stationary) but almost one. The threshold to spot when that issue aroused (red line on Figure 3.28) was computed as four times the standard deviation of the mean value of the displacements in the y direction. As already stated in the previous section, the small fluctuations on the mean displacement in the y-direction are due to particles entering and exiting the investigation windows, to their not perfectly uniform spatial distribution, and because of the measurement noise.

Figure 3.29 shows the number of occurrences of this problem for the various runs.

6.4 Particle parameters for PTV

After post processing, a Matlab code was used to find the particle parameters on the binary images to use as an input for the PTV codes (see chapter 4) for each run: these parameters were area, x-size, y-size and edge-to-area ratio of the particles. A histogram of these parameters was produced for each run, so allowing a very accurate selection of the particles to track. Some typical value of these parameters were as follows: maximum area around 160 pixel, minimum area 4 pixel, maximum x and y size around 18 pixel, minimum x and y size 2 pixel, maximum edge-to-area ratio 26 pixel, minimum edge-to-area ratio 11 pixel (see Figures from 3.30 to 3.33, with the values of run 34 of the first campaign of measurements).

It should be noticed that these values, computed over post-processed images, are much larger than the ones of the actual particles, because the post-treatment tends to enhance the particles' brightness on the picture but to spread and enlarge them too (see section 6.1 and compare Figure 3.23 with Figure 3.25).

The edge-to-area ratio is the ratio between the square of the perimeter of a particle and its area and gives an indication of the particle shape: for instance, a large value for this ratio indicates either linear particles or particles with very convoluted and tortuous edges, whilst a value of 16 indicates a large, circular particle. In fact, a perfectly spherical particle would have an edge-to-area ratio of $(2\pi r)^2/(\pi r^2) = 4\pi$, a square particle would have a ratio of 16, while a line of length L and one single pixel wide would have a ratio equal to 4L.

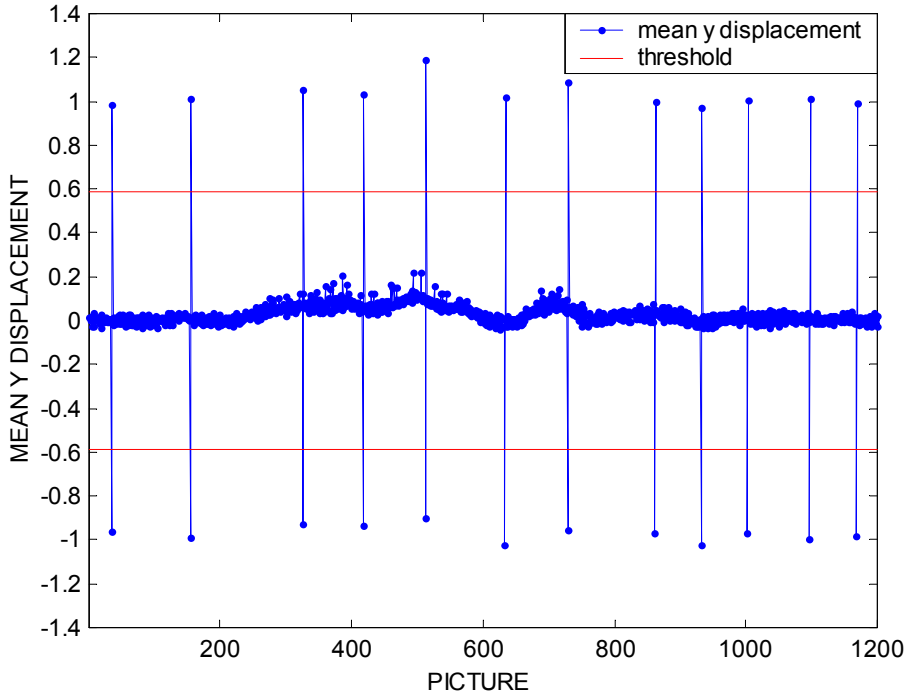

Figure 3.28 The mean value of the displacements in the y direction (blue line) and the threshold used to detect the pictures moved of one pixel in the y-direction, on run 21 of the first campaign of measurements; below.

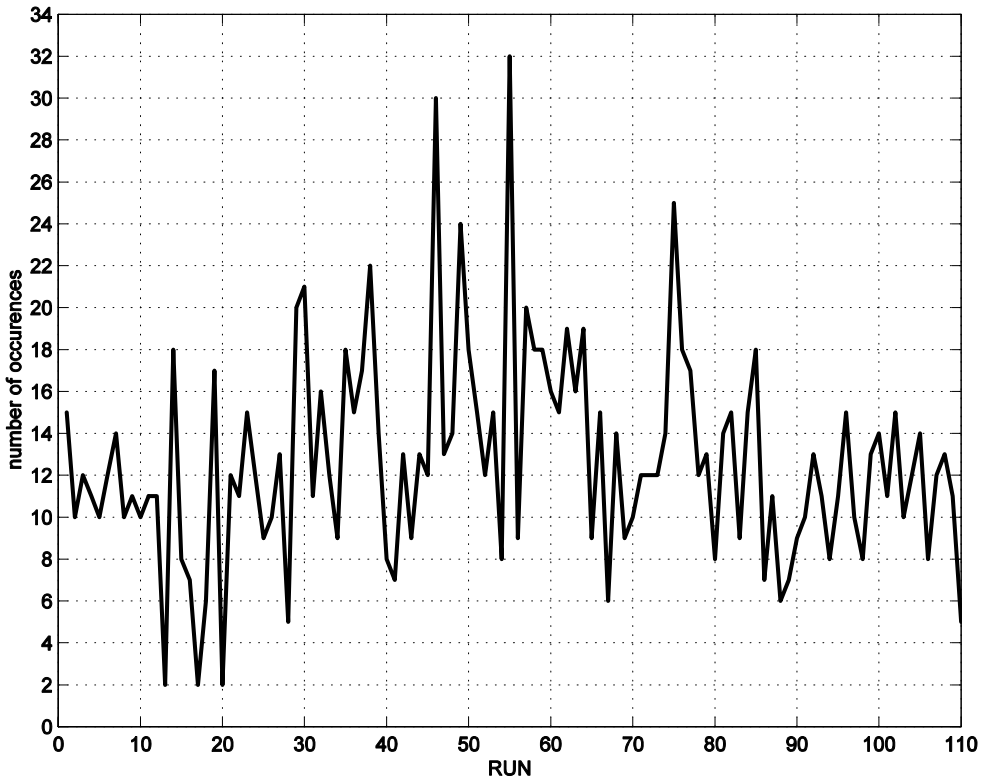

Figure 3.29 Number of occurrences (over 1200 pictures) of the 1-pixel upward issue from the camera, during the first campaign of experiments (110 runs during four days).

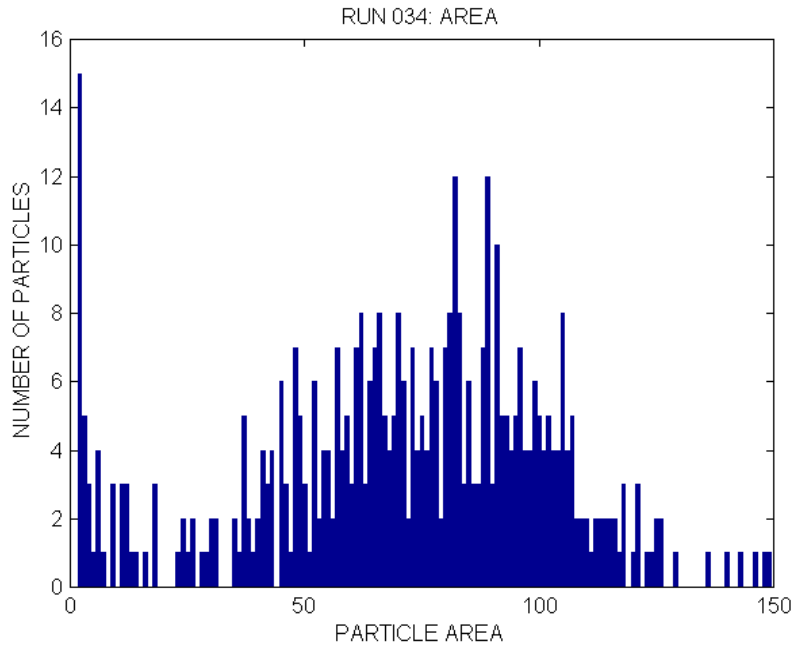

Figure 3.30 Example of the histogram of particle area, in pixel, on one run of the first campaign of experiments with constant forcing.

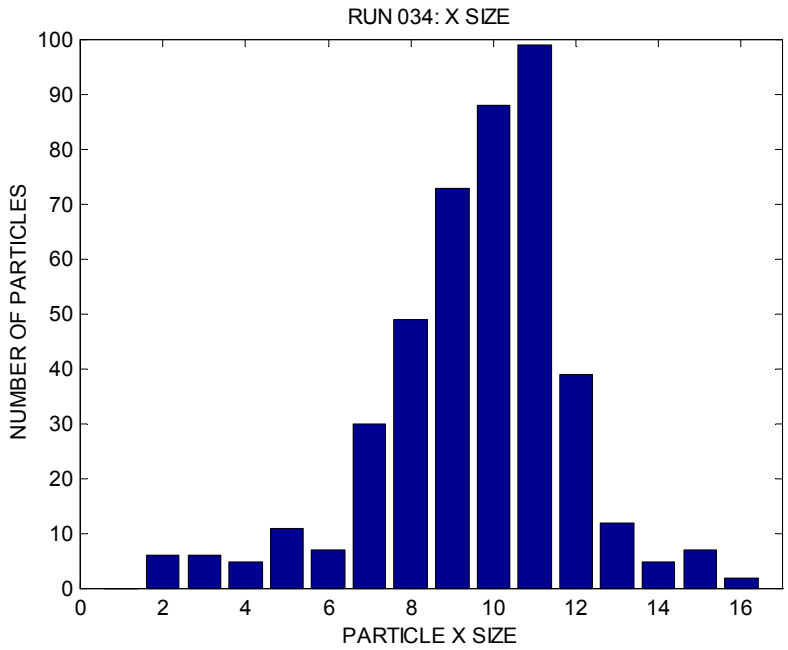

Figure 3.31 Example of the histogram of particle x-size, in pixel, on one run of the first campaign of experiments with constant forcing.

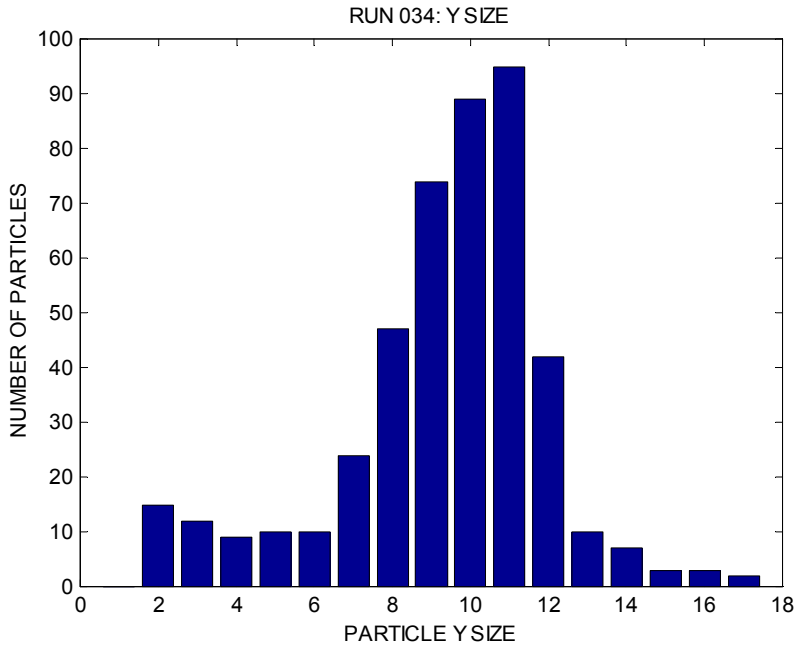

Figure 3.32 Example of the histogram of particle y-size, in pixel, on one run of the first campaign of experiments with constant forcing.

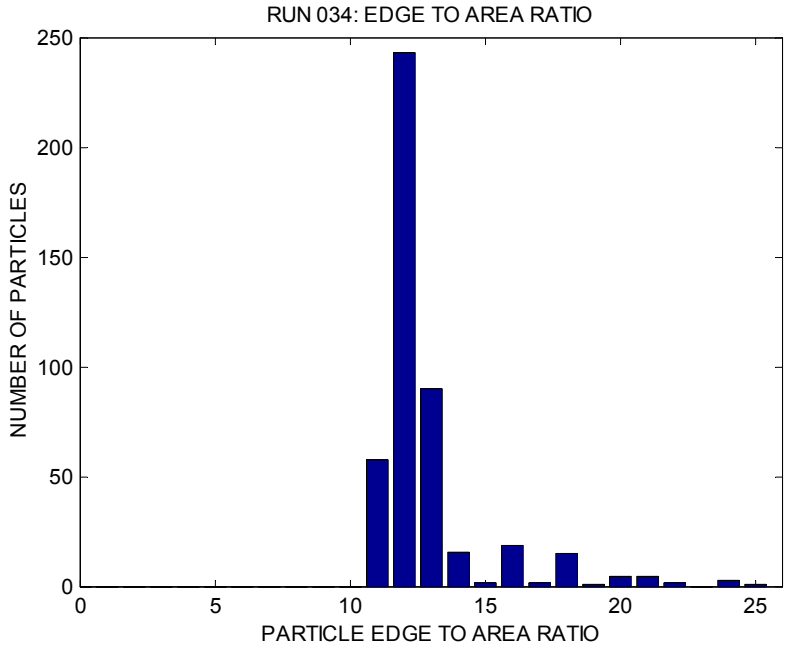

Figure 3.33 Example of the histogram of particle edge-to-area ratio, in pixel, on one run of the first campaign of experiments with constant forcing.

4. PTVA (PARTICLE TRACKING VELOCIMETRY AND ACCELEROMETRY)

1 INTRODUCTION

As explained in chapter 1, to study multiple-scales turbulent-like flows is important to accurately measure the local acceleration, which is significant for the behaviour of all the scales of the flow. The measurements should be very accurate at all the scales, with a critical insight given to the close vicinity of the hyperbolic stagnation points, where the velocities are small but with strong curvature of the streamlines and high strain. As experiments regarding turbulent-like flows with a time-dependent forcing are currently carried out in the Hydraulics Laboratory of the Department of Aeronautics of Imperial College London, these measurements should be accurate also when the flow is time dependant. One extra difficulty for time dependent flows is that the stagnation points can move, even if this displacement is small compared to turbulence intensity, as shown in Goto et al. (2005). These points and their connected structure are thus difficult to measure, but at the same time they are areas of strong streamlines curvature and so of first importance for the study of dispersion and turbulent flows. In addition, considering a bounded displacement of these points, we should expect their acceleration to be time dependent.

So the target was to measure accurately Lagrangian velocity and acceleration on these turbulent-like flows, for both high and low values (actually, for zero values). Measuring very small values of velocity has by itself some difficulties also on laminar flows, as stated in Stanislas et al. (2005), where it is shown that traditional PIV (Particle Image Velocimetry)-PTV (Particle Tracking Velocimetry) codes encounter some difficulties in the region of a submerged turbulent round jet where there is no turbulence and the flow moves very slowly (regions with a nearly uniform displacement with a magnitude that is well below one pixel): as one of the target here is to accurately measure stagnation points, it is clear that these methods cannot be used.

Another target of this study was to have access to the measure of all the component of the Navier-Stokes equations, so as to have a deeper insight upon the physics governing these turbulent-like flows. But, to date, the only available techniques for pressure measurement away from boundaries are based on Pitot-tube type of probes (Liu and Katz, 2006), that are intrusive, not suitable for dynamic measurements (because of their limited response in frequency) and can only perform measure in one point per probe. Another technique used in the past to measure pressure away from the boundaries was based on microscopic bubbles as pressure sensors (Ooi and Acosta, 1983, O'Hern, 1990, Ran and Katz, 1994), but they provided only a very limited number of data points for each run of measure.

An available technique to have Lagrangian measurements of velocity is Particle tracking Velocimetry (PTV) but it is very sensitive to the measurement noise. To reduce this problem, low-pass filter have been used on the tracked particle positions (La Porta

et al, 2001, Voth et al., 2002, Mordant et al., 2004, Luthi et al., 2005,): the main issue in this case is the choice of the temporal window size of the filter because, if this size is too large, small fluctuations of the measured values can be smoothed away, if it is too small, the noise is not removed. Again, this technique could not be used to measure multi-scale flows.

In this work, the use of a self-adaptive iterative method (Particle Tracking Velocimetry and Accelerometry, PTVA) that relies on an adaptive number of tracked positions, for the trajectories approximation, depending only on the local flow properties, is proposed. The criterion proposed holds the potential to withdraw some convection/sweeping information and thus to extract more accurately the acceleration and velocity of convected/swept structures. As the turbulent-like flows studied here are repeatable from the Eulerian point of view, if the Lagrangian measures are enough accurate and their number sufficiently high, the extraction of the Eulerian information from the Lagrangian one could be achieved; moreover, whether a very high accuracy should be reached, a double spatial derivative on the velocity could be obtained and then, as the forcing is known, an indirect measure of the pressure gradient achieved too.

In this chapter, a brief introduction around measurement methods used in turbulent flow will be given initially; then, as PTVA takes as an input particle positions from PTV, some words will be spent on PTV and on the codes used here, i.e. DigiFlow (Dalziel, 1992) and GPTV (Querzoli, 1996); the PTVA method will be later explained in detail, including its qualitative and quantitative validation and the comparison among some of its measurements with the ones extracted using previous methods.

2 MEASUREMENT METHODS ON TURBULENT FLOWS

As previously stated in Chapter 2, the turbulent-like flows investigated in this thesis holds some of the features of turbulent flows: for this reason, it was natural to give look at the experimental measurement methods applied to turbulent flow, in the present and in the past, when it was decided to experimentally measure the acceleration, in order to select the most suitable one to this purpose. Several techniques have been used to measure particular characteristics in a turbulent flow: each of them has peculiar features and provides the measurement through a different way. This section, without the pretence to be comprehensive, will give a brief list of these techniques, together with an explanation of why each one of them was selected of discarded in order to achieve the acceleration measurement targeted in this chapter's introduction.

Traditional systems to measure the velocity in a single point of the flow are Laser-Doppler Velocimetry (LDV, also known as Laser Doppler Anemometry LDA), Pitot tubes and Hot Wire Velocimetry (HWV): all of them provide the time history of velocity in a single point of space and, whether a spatial investigation is needed, a number of probes high enough must be used or, provided the flow experiment is repeatable, their position can be changed during the experiments. Their advantage is mainly the high acquisition frequency (more than 105 Hz) whilst, on the other hand, their main drawbacks are the difficulties of obtain a measure over an investigation area, the fact that they are

intrusive (so that it is almost impossible to sample at the same time many points in the flow, particularly if they are close to each other) and the fact that they need a calibration, not always easy and fast.

A technique recently developed by Mordant et al. (2002) make use of ultrasonic techniques (that yield non-intrusive measurements) for the measurement of the velocity of individual solid particles moving in fluid flows; this technique relies on the ability to resolve in time the Doppler shift of the sound scattered by the continuously insonified particle.

Many techniques based on Image Analysis (IA) have been developed: in all of them, pictures of the flow, seeded with tracers, are taken and measurements are extracted from the pictures.

If the target is to measure how a substance can be diluted by the flow, a widely used IA technique is the Light Induced Fluorescence: the flow is seeded with dyes (such fluoresceine, Rhodamine) that, when illuminated, radiate light. Provided the density of the substance is in the correct range, there is a linear relation between the intensity of the light radiated by the substance itself and the concentration of it. More recently, techniques that couple LIF and Particle Image Velocimetry (PIV, see below), in order to have simultaneously measures of concentration and velocity, have been developed (Hishida et al., 2001, Nagaya et al., 2001).

Image Analysis techniques suitable for velocity measurement can be basically classified under these labels: Particle Streak Velocimetry (PSV), Feature Tracking (FT), Particle Image Velocimetry (PIV) and Particle Tracking velocimetry (PTV). All these techniques evaluate the velocity measuring the distance covered by a feature (a particle or a marker for PSV, PIV and PTV, a point of high gradient of the intensity for FT) on the images in a given time. Whilst traditional methods gives measures only in one point, Image Analysis techniques give measures all over the investigation field (or, more precisely, wherever particle/feature are found), do not need a probe (so they are essentially not invasive, at least if the particles do no perturb the flow) and do not need any particular calibration (as the relation between the measured quantity, a displacement, and the required one, a velocity, is linear). All these techniques need that the fluid is seeded with neutrally buoyant particles and illuminated with a light source: pictures of the flow can be then taken at known temporal frequency and the velocity computed as the distance covered by a particle/feature in divided by the time elapsed.

In Feature Tracking (Lucas and Kanade, 1981, Shi and Tomasi, 1994, Cenedese et al, 2004) the object to be tracked is not chosen a priori but by the method itself as a feature that can be well tracked: a certain number of points in the picture with a high spatial gradients of light intensity are usually selected.

Particle Streak Velocimetry (Adrian 1991, Bergthorson and Dimotakis, 2006) measure velocity along the streaks left by moving particles on a long exposure image: if in this way the ambiguity between particles can be reduced, particles entering or going out from the flow or traveling along trajectories with a strong curvature can cause errors in the measure of the velocity; moreover, ambiguity on the velocity sign can arise.

Particle Tracking Velocimetry (see Adrian, 1991, Dalziel, 1992, Querzoli, 1996, Virant and Dracos, 1997, Nadeem and Dracos, 1993) differs from Particle Image Veloci-

metry (see, for example, Adrian, 1991, Merzkirch et al., 1994) in a fundamental way: PIV relies on pattern matching in an essentially Eulerian way, whilst PTV tries to identify individual particles and to follow them in a Lagrangian sense. PIV implies a spectral analysis or a (auto or cross) correlation performed on small window of the investigation field in order to get a single velocity sample for each window, so it is fairly robust to noise, with a spatial resolution that is inversely proportional to the window size. In PTV the displacements of single particles are considered in order to reconstruct trajectories: its information achieve a high local accuracy in every seeded point of the flow, with the possibility of solving small velocity variations and of obtaining a higher spatial resolution compared to PIV; on the other side, PTV is much more sensitive to noise. Because of the different way they use to compute velocity, PIV furnishes the time-history of the velocity at fixed locations (that is Eulerian data), whilst PTV gives velocities along trajectories (that is a Lagrangian description of the flow): moreover, an Eulerian description can be extracted from the Lagrangian information if there are enough samples to cover the investigation region. It should be said that, on the other hand, it is not possible to get reliable Lagrangian information using PIV, because the transformation from the Eulerian description to the Lagrangian one implies an integration in time of the velocity field, not reliable especially when considering phenomena like turbulent flows with high sensitivity to initial conditions.

PIV allows higher seeding levels whilst in PTV the density of particles have to be low enough to allow single particles to be recognized.

In summary, PTV is complementary to PIV, with its ability to cope with low and medium particle concentration, to reach a higher spatial resolution and to cope with specific cases like regions with strong velocity gradients. PTV shows clear advantages to PIV in near-wall regions with high velocity gradients as they can provide measurements nearest to the wall (Stanislas et al., 2005).

To conclude this section, few words will be spent about two novel techniques, which can be considered in some way similar to Image Analysis ones): Holographic Particle Image Velocimetry (HPIV) and fast detectors.

Holographic Particle Image Velocimetry (Hinsch, 2002) is a novel technique to obtain a three dimensional particle image velocimetry (i.e. the measurement of all spatial components of the velocity vector), but it still needs sophisticated instruments to be put in practice.

Fast silicon strip detectors have been used to optically image short particle (tiny transparent beads) tracks and measure particle acceleration (La Porta et al., 2001, Voth et al, 2002), reaching a very high time resolution (up to 70,000 frames per second) but in a small measurement volume (particles can be followed for only few Kolmogorov time scales).

3 PTV

As the technique developed in this work takes as an input particle positions extracted by PTV, in this section an explanation of the basic principles underlying PTV will be

given. Also if there are many different PTV codes based on various procedures, the basic steps followed in PTV can be listed as follows: image acquisition, particle detection and trajectory recognition.

3.1 PTV: image acquisition

Concerning the image acquisition, as previously mentioned, in order to perform PTV the working fluid has to be uniformly seeded with neutrally buoyant particles and the region of interest uniformly illuminated: one or more video-cameras take images on which, if the experiment is correctly set, particles appear as bright spots on a dark background. Particles have to be chosen with a high light scattering property, so that their image is as bright as possible, and with a spherical shape so that the scattered light does not depend on their orientation. Every expedient that can be useful to reduce the noise on the recorded pictures (such as remove every possible source of light not coming from the lighting devices, make as black as possible the background, etc.) should be taken. If the camera is not a digital one, the images need to be digitalized in order to convert them in computer-readable matrices.

3.2 PTV: particle detection

Regarding the particle detection, it is performed on the recorded images in order to obtain the positions of the particles: the process is based on applying one or more thresholds on the images, on the recognition of particles as connected sets of bright pixels and on the computation of the particle position, usually its binary barycentre (if the result of the threshold is a binary image) or its grey scale centre of mass (if the threshold save all the values above it). Another way sometimes used for particle detection is to Gaussian fit the intensity distribution of the particle image and to calculate its centre as the mean value of the Gaussian. Both these methods have sub-pixel accuracy. Grey scale centre of mass and Gaussian fit work on the assumption, true only on ideal particle images, that the position of the particle centre corresponds to the position of the maximum in the image intensity distribution.

3.3 PTV: trajectory recognition

Trajectory recognition is the tracking of particle from image to image, so to link positions of particles at time $t+1$ that match certain criteria with those at time t. The tracking procedure is obviously different if one has knowledge of the previous motion of the particle or not: in the first case, the earlier information can be used to predict a new position of the particle at time $t+1$ and look for particle positions in the search area around this position; in the second case, no prevision can be done and the search radius has to be of the same order of the maximum presumed displacement. Particle tracking is so carried on by looking for temporal series of particle locations that fulfil the criteria of: distance between two successive locations less than a given parameter; difference between two successive displacement less than a second given parameter. While the first condition corresponds to a known/assumed maximum velocity in the investigated flow, the second is equivalent to an assumed maximum acceleration. This last criterion can be

relative to the turbulent parameter of the flow. In the case of an ambiguity due to the presence of more than one particle in the search area, a solution can be to assume that the time interval between images is small enough to use a minimum variation criterion; as a consequence the particle closer to the predicted position is supposed to represent the continuation of the trajectory. If a linear prediction is used this corresponds to validate the trajectory with minimum acceleration.

3.4 DigiFlow and GPTV

To extract the particle positions to be used as an input to PTVA, two PTV codes have been used: DigiFlow (Dalziel, 1992) and GPTV (Querzoli, 1996).
DigiFlow makes use of multiple thresholds to try picking up particles with a broad range of intensities. This multiple-threshold technique has given, in the images recorded for this work, an issue concerning the identification of more than one centroid on each particle: to solve this problem, a post-processing on the pictures, described in the previous chapter, was needed in order to convert grey-level pictures into black and white ones. In order to solve tracking ambiguities, DigiFlow uses a modification of what is known in operations research as the *Transportation Algorithm* that, basically, consists in the minimization of a costing function taking in account various parameters of the particles and of the flow. DigiFlow advantages compared with GPTV can be a better interface, that allows following the particles recognized with their velocity vector, and a more precise chance to select only the particle required for the tracking, as many input parameter for the particle are required (maximum and minimum size in x and y direction, maximum and minimum area, maximum and minimum shape factor, maximum and minimum light intensity, etc.).

GPTV use a single threshold to identify the particles and a tracking procedure similar to the described in the previous section, whose way to solve ambiguities underpins a minimization in the change of the acceleration modulus. If compared with DigiFlow, less parameters of the particles (only maximum and minimum area) and of the flow are required as an input. The biggest advantage of GPTV compared with DigiFlow is the lower time of computation (almost ten times faster than DigiFlow).

In order to not alter the measure of the acceleration, a great care was accorded to the issue of clustering particles: as a matter of fact, when two particles get so close that they are attracted each other, their trajectories are altered and, most significant for this work, spurious accelerations can be measured. As this phenomenon was encountered very seldom in the present flow, it was decided to remove the trajectories belonging to particles that clustered. Both the cited PTV codes are able to deal with cluster: DigiFlow takes advantage of the long list of particle parameters required as an input to recognizing particles that cluster from the changes in these parameters, whilst GPTV uses a single parameter taking in account the variation in the area of a particle belonging to a trajectory: when the variation in the area of a particle from time t to time $t+1$ is larger than a fixed value, the linking is not done and the trajectory is interrupted. This means that, in order to avoid keeping in account trajectories with clustering particles, a careful study of the particle characteristics has to be carried out on the images before performing PTV.

run	1	2	3	4	5	6	7	8	9	10
total trajectories	631	685	626	673	694	704	723	661	671	705
long trajectories	310	340	320	320	346	305	356	325	312	319

run	11	12	13	14	15	16	17	18	19	20
total trajectories	481	477	420	499	528	538	524	545	531	527
long trajectories	264	280	255	285	299	308	297	288	296	298

run	21	22	23	24	25	26	27	28	29	30
total trajectories	530	592	576	581	564	519	526	499	455	470
long trajectories	329	319	324	337	311	291	292	316	317	298

run	31	32	33	34	35	36	37	38	39	40
total trajectories	427	406	421	431	468	495	469	520	540	452
long trajectories	269	264	267	280	294	275	281	337	295	261

run	41	42	43	44	45	46	47	48	49	50
total trajectories	474	467	470	515	471	468	429	449	438	442
long trajectories	289	290	304	303	285	286	291	303	274	285

run	51	52	53	54	55	56	57	58	59	60
total trajectories	454	462	449	480	475	474	475	512	489	504
long trajectories	262	277	278	274	284	289	276	290	279	310

run	61	62	63	64	65	66	67	68	69	70
total trajectories	434	494	440	467	447	443	452	480	497	494
long trajectories	264	271	265	280	249	294	268	282	262	277

run	71	72	73	74	75	76	77	78	79	80
total trajectories	478	469	534	583	525	504	500	515	562	563
long trajectories	284	264	318	290	272	284	248	297	305	309

run	81	82	83	84	85	86	87	88	89	90
total trajectories	540	506	529	530	531	533	565	549	521	543
long trajectories	277	309	293	274	300	288	288	302	298	295

run	91	92	93	94	95	96	97	98	99	100
total trajectories	534	570	559	583	569	537	595	595	580	575
long trajectories	283	278	290	288	279	313	294	327	332	326

run	101	102	103	104	105	106	107	108	109	110
total trajectories	545	542	515	574	593	576	575	542	575	582
long trajectories	335	280	299	305	323	299	355	293	321	325

Table 4.1 Number of trajectories tracked for at least one turnover time of the large scales (total trajectories) and for the entire length (long trajectories) on each run of the first campaign of experiments.

run	1	2	3	4	5	6	7	8	9	10	11
total trajectories	293	353	337	441	468	425	689	543	455	542	439
long trajectories	120	160	158	199	176	185	302	255	220	252	212

run	12	13	14	15	16	17	18	19	20	21	22
total trajectories	416	435	633	720	620	593	604	615	588	649	486
long trajectories	234	195	301	313	266	277	290	306	273	278	255

Table 4.2 Number of trajectories tracked for at least one turnover time of the large scales (total trajectories) and for the entire length (long trajectories) on each run of the second campaign of experiments.

Anyway, it should be noticed that, on the flow object of the present work, these two PTV codes, even if very different in many aspects, have given the same results concerning the number of tracked trajectories and the positions identified. In table 4.1 and 4.2 , the number of particles tracked for at least one turnover time of the large scales (19.17 seconds which is equivalent to 192 time steps, as the acquisition rate in all these experiments were 10 frames per second) and for the entire length of each run (1200 time steps on the first campaign, 1000 time steps on the second one) are accounted.

4 PARTICLE TRACKING VELOCIMETRY AND ACCELEROMETRY (PTVA) METHOD

As already stated, the Lagrangian measurement on this multi-scale flow has to be accurate at large and small scales and for large and low intensity of the velocity and of the acceleration: as PTV gives access to Lagrangian measurement it was naturally chosen for this kind of measurements. The problem was that this technique is very sensitive to the measurement noise. In order to reduce this noise, many attempts have been done in the past. For example, a first effort has been the computation of the velocity as the space covered in time over more than two consecutive frames (Virant and Dracos, 1997). More recently, a low-pass filter has been used on the trajectories to filter the noise in order to have access on the acceleration, using an approximation of the trajectories with a moving polynomial of various order (a parabola in La Porta et al, 2001 and in Voth et al., 2002; a third order polynomial in Luthi et al., 2005) or a filtering kernel (Mordant et al., 2004): anyway, in all these techniques the key issue is represented by the choose of the duration of the time window (i.e., of the number of consecutive positions to use to fit the polynomial), always chosen on the base of the particular data set. An example of filtering, via a moving polynomial of order two and a fixed number of position (31), is given on Figure 4.1 where the raw particle positions extracted by PTV are reported in black together with the filtered ones (red line).

In practice, if, on one hand, this number is too large, small fluctuations of the measured values can be smoothed away, whilst, on the other hand, if it is too small, the noise is not efficiently removed. This clearly shows that these techniques are not feasible to

perform accurate acceleration measurements on multi-scale flows, because a large time window can effectively be adopted to fit almost straight trajectories of particles travelling with an almost constant velocity but not on trajectories that experience sudden and repeated changes indirection, velocity and acceleration, and vice versa.

For this reason, a self-adaptive iterative method (Particle Tracking Velocimetry and Accelerometry, PTVA) is proposed here. It was designed in order to use a moving polynomial to approximate the trajectories using an adaptive number of positions, which depends only on the local flow properties (see the next section for a general description of the method and sections from 4.2 to 4.4 for a more detailed description). Velocities and acceleration are subsequently extracted as time derivative of the trajectories. PTVA was validated with a geometrical approach based on synthetic trajectories with known positions, velocities and accelerations (section 5): this allowed a quantitative evaluation of the method accuracy and a comparison of its accuracy with previous methods' ones (section 5.1). The performance of the different methods was also compared on the multi-scale flow object of this work (section 6).

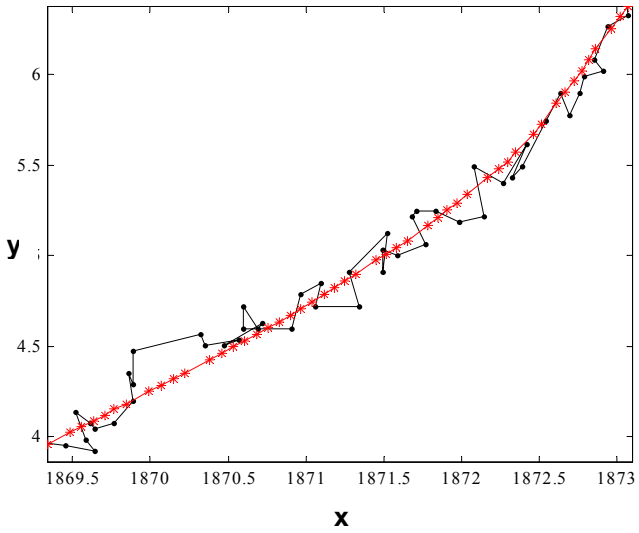

Figure 4.1 Example of the noise filtering from the positions extracted by PTV (black spots) via a moving polynomial of order two and a fixed number of position (31); the red asterisks are the position approximated with the moving polynomial; axes are in pixel.

4.1 General description of the method

As previously stated, PTVA can be described as an "iterative" and "self-adaptive" method to measure acceleration in fluids. PTVA can be defined "iterative" because two approximations of the trajectories are performed, a first one to extract a measure of the velocity to give as the input of the second approximation; PTVA can be called "self-

adaptive" because it adapts the number of position used for trajectories approximation according to some flow parameters.

In particular, in the first step the position extracted by PTV are approximated into x and y-components of the trajectories via a least square approximation, making use of a fourth order moving polynomial, with a variable number of positions depending only on a minimum and maximum distance (see section 4.3.1): from the temporal derivatives of this approximated trajectory components, the velocity components are extracted via a temporal derivative.

In the second step, the same approximation is performed starting again from the positions extracted by PTV, again using the least square approximation of a fourth order moving polynomial, but with a criterion that adapts the number of positions for the approximation in order to have a parameter, the "convected displacement", Δ_S, able to take into account the local flow properties, as close as possible to a target value, Δ_{TARGET} , equal to the perimeter of the smallest eddy to be measured (see section 4.3.2). The components of the velocity and acceleration are then extracted via temporal derivatives.

The polynomial of order four has been chosen in order to allow three changes in the direction of the trajectory components and so one change in the sign of the acceleration components (see next section).

4.2 Moving polynomial of order n to approximate the trajectories

In this section, a description of the polynomial function used to approximate the trajectories will be given. The description of the method is given hereafter making use of vectors (e.g. $\vec{x}$,$\vec{u}$ ...), nevertheless for extra accuracy on each coordinate (but with an extra time of computation) it can easily be adapted for each separate coordinate (e.g. x, u_x, y, u_y,...).

4.2.1 Polynomial functions

Once the particle positions have been extracted via the traditional PTV codes described in the previous section 3, the trajectory components are approximated by fitting to these positions a moving polynomial function of order n:

$$\vec{x}_n(t) = \vec{b}_n t^n + ... + \vec{b}_1 t + \vec{b}_0 \tag{4.1}$$

The velocities and accelerations are then extracted from the trajectories $\vec{x}_n(t)$ with the following time derivatives:

$$\vec{u}_n(t) = n\vec{b}_n t^{n-1} + ... + \vec{b}_1 \tag{4.2}$$

$$\vec{a}_n(t) = n(n-1)\vec{b}_n t^{n-2} + ... + 2\vec{b}_2 \tag{4.3}$$

If the flow is strongly time dependent or experiences sudden and repeated changes indirection, the order of interpolation n should be larger than two or the sampling of the experiment should be performed at very high frequency to obtain accuracy.

4.2.2 Time-scale resolution

The order of the trajectory's approximation, n, determines a maximum number of changes in direction $\frac{n-1}{2}$: for instance, $n = 2$ allows only one change in direction, $n = 3$ two changes, $n = 4$ three changes, etc. This is relevant, for instance, when the polynomial is used to approximate the trajectory of a particle trapped in a rotating eddy: considering an eddy of turnover time, T_{cut}, the largest time interval for the approximation (i.e., the temporal length of the window used for approximation) $N_n \Delta t$ (where N_n is the number of positions used for the approximation and Δt is the time between two positions, related to the sampling or acquisition frequency) has an upper boundary imposed by the number of changes allowed by n:

$$(N_n)\Delta t \leq \frac{n-1}{2} T_{cut} \tag{4.4}$$

The turnover time, T_{cut}, represents a threshold for the time scales resolved in the measurements, corresponding to the smallest turnover time that the trajectory approximation can track. Moreover, N_n has a lower boundary imposed by the minimum number of positions needed to approximate the polynomial function:

$$N_n \geq n+1 \tag{4.5}$$

If was $N_n = n+1$, the polynomial would follow exactly the positions extracted by PTV keeping all the noise, so N_n can be chosen as follows:

$$N_n = An + B = C_n n \tag{4.6}$$

where A and B are two arbitrary constant and C_n a constant depending on n. Equation (4.4) can so be written, to highlight the upper boundary in the sampling time, as:

$$\Delta t \leq \frac{n-1}{n} \frac{T_{cut}}{2C_n} \tag{4.7}$$

The corresponding minimum frequency of the camera $f = \frac{1}{\Delta t}$ is also linked to *n*:

$$f > 2C_n \frac{n}{n-1} \frac{1}{T_{cut}} \tag{4.8}$$

According to equations (4.7) and (4.8), approximations of order higher than two allow to improve the small scales resolution (length and time) for a given frequency and to enlarge the frequency of acquisition for given small flow scales (time and space). It could be noticed than this improvement is less and less effective with the increase of *n*, as *n/(n-1)* rapidly tends to one, while it implies an extra computational time.

4.2.3 Length-scale resolution

The spatial length of the Δ (i.e., the spatial length of the window used for approximation) should be kept smaller than the displacement related to the small scale flow structure that the polynomial approximation is able to extract. This can be estimated by the following relation:

$$\Delta \leq \pi \phi_{ed} \frac{n-1}{2} + \Delta_{conv} \tag{4.9}$$

where Δ_{conv} is the average convection during the temporal window of the approximation, ϕ_{ed} is the diameter of the smallest eddy to be tracked and *n* the order of the polynomial approximation. It should be noticed here that an order of interpolation higher than two allows larger maximum of displacement whilst correctly tracking the small eddies. For $\Delta_{conv} = 0$ and $n = 4$, relation (4.9) leads to $\Delta \leq \frac{3}{2}\pi\phi_{ed}$, so with a polynomial of order four Δ cannot be larger than one and half time the perimeter of the smallest eddy to measure.

4.2.4 Adaptation to local flow properties

The local convective information (mean velocity in the Lagrangian frame) is removed from the signal in the second step approximation of PTVA, in order to ensure that the polynomial approximation focuses on a flow structure (see section 4.3.2). This flow structure can be either a convected (and/or swept) spatial structure, see figure 4.2, or a *temporal structure* due to various time dependencies.

The order of the polynomial approximation gives a limitation in the number of loops which can be approximate, e.g. half a loop for an order two, one loop for on order three, one loop and a half for an order four, etc. As previously stated, an adaptive method should be able to extract the right information, i.e. enough information to be accurate on the acceleration but not too much so to not filter excessively the flow. Thus the smallest turn over time of the flow and the corresponding length scale is chosen as the critical parameter for an order four polynomial approximation. This adaptive method thus relies only on physical criteria related to the flow small scales to be extracted, i.e. to the smallest turn over time of the flow and to the corresponding small scale. The method attempts to extract the information related to one turnover time of this given scale in the corresponding Lagrangian frame. In practise, the smallest turnover time sampling is adapted via the frequency of the camera and the smallest scale diameter, ϕ_{ed}, becomes the only input parameter of this method. In fact, the smallest scale that the method could accurately extract for this smallest turn-over time is related to the order of the polynomial approximation, i.e. $2\phi_{ed} / 3$ for an order four.

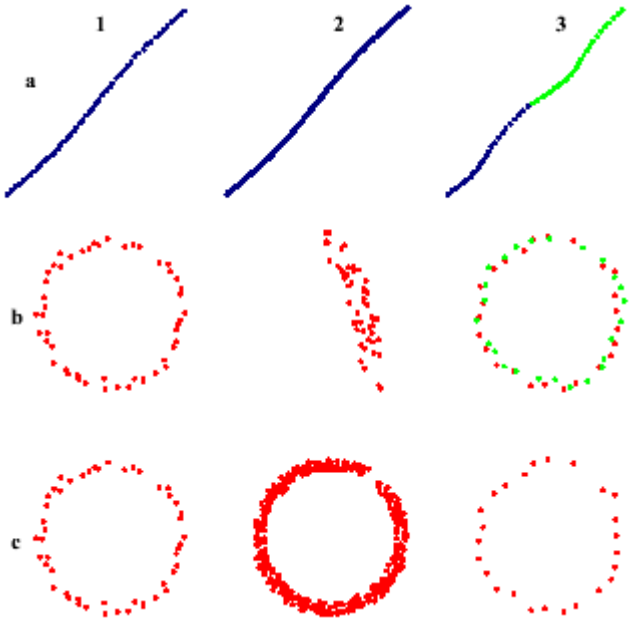

Figure 4.2 Illustrations of the information extracted from tracking with a trajectory approximation based on a moving polynomial in the case of a convected structure; columns refer to different sampling frequency, i.e. (1) to one turn over time and a reference frequency, (2) to one turn-over time and an higher frequency, (3) to two turn over times and a lower frequency; rows refer (a) to the trajectory of a convected eddy, (b) to the positions extracted using a constant number of positions, (c) to the positions extracted using the same fourth order moving polynomial approximation but with an adaptive number of position which take in consideration convection removal (PTVA), that is able to systematically catch one turn over time of the convected eddy.

4.3 Acceleration measurement in two stages, PTVA

In this section the PTVA algorithm and its acceleration measurement in two stages will be discussed: it should be noticed that the two stages do not imply a two time approximation of the trajectories, as the second stage takes as an input the particle positions extracted via PTV as well as the first stage.

4.3.1 First stage: initial velocity measurement

The target of this first stage is to extract a first measure of the velocity to be given as one of the input of the second stage. As already stated, the target is to be accurate for small and large velocities, which is of first importance as the topological structure of this turbulent-like flow is intimately controlled by a multiple-scale distribution of flow structures connected to stagnation points. This requires an adaptive number of positions, $N_n(t)$ for the trajectories approximation able to adapt to the local flow characteristics. The adaptive particle displacement, Δ, is given by:

$$\Delta = \sum_{i=-N_n(t)/2}^{i=N_n(t)/2} \left\| \vec{x}_{i+1} - \vec{x}_i \right\| \tag{4.10}$$

For a certain trajectory and at the time t, $N_n(t)$ is initially put equal to N_{in}, Δ is computed together with its components Δ_x and Δ_y using N_{in} positions; $N_n(t)$ is then adapted so that $\Delta_{min} \leq \Delta \leq \Delta_{max}$ and $N_{min} \leq N_n(t) \leq N_{max}$, in order to give quality to the measure, in this way: while $\Delta_x < \Delta_{min}$, or $\Delta_y < \Delta_{min}$, and $N_n(t) < N_{max}$, $N_n(t)$ is increased; while $\Delta > \Delta_{max}$ and $N_n(t) > N_{min}$, $N_n(t)$ is decreased. When the value of $N_n(t)$ respecting the conditions is found, the trajectory components $x(t)$ and $y(t)$ are approximated, in a least-square sense, using $N_n(t)$ positions, half backwards and half afterwards, and the velocity and acceleration components $u_x(t)$, $u_y(t)$, $a_x(t)$, $a_y(t)$ computed via time derivatives.

Δ_{min} is the minimum displacement needed to have a signal versus noise ratio high enough for the minimum quality required in velocity and acceleration measurement; Δ_{max} is given by a topological consideration on the small scale flow structure, i.e. Δ_{max} has to be less than or equal to the smallest scale of the flow; N_{min} has to larger than $n+1$, that is the minimum number of position that a polynomial of order n requires to fit the data; N_{max} is a large number, with the only limitation that an N_{max} too large would increase too much the computation time. The values of this parameters used to approximate the experimental data object of this work are given in section 6.

This leads to a relatively accurate measurement of the velocity in each position that can be used in the second stage, where the actual measurements are performed.

4.3.2 Second stage: acceleration measurement

A new least mean squares approximation of the trajectories, using the Lagrangian ve-

locity information obtained in the first stage, is performed in this second stage, which gives as an output the velocity and acceleration measurements required. In order to do this, the local time average of the velocity of the tracked particle, $\overline{\vec{u}}$, is computed, making use of the equation

$$\overline{\vec{u}} = \frac{1}{N_n(t)} \sum_{i=-N_n(t)/2}^{i=N_n(t)/2} \vec{u}_n(i) \tag{4.11}$$

This average velocity is thus used to compute the convected (and/or swept) displacement, Δ_S.

$$\Delta_S = \sum_{i=-N_n(t)/2}^{i=N_n(t)/2} \left\| \vec{x}_{i+1} - \vec{x}_i - \overline{\vec{u}}\Delta t \right\| \tag{4.12}$$

$N_n(t)$ is then adapted trying to get a Δ_S close to Δ_{TARGET} , which is equal to the perimeter of the smallest eddy to be extracted, $\pi\phi_{ed}$ (as previously stated, ϕ_{ed} is the smallest scale diameter), i.e. $N_n(t)$ is adapted until $\Delta_{Smin} \le \Delta_S \le \Delta_{Smax}$ and $N_{\max} \ge N_n(t) \ge N_{\min}$, with $\Delta_{S\min} = \frac{\Delta_{TARGET}}{2}$ and $\Delta_{S\max} = \frac{3}{2}\Delta_{TARGET}$. In practice, for a certain trajectory and at a certain time *t*, $N_n(t)$ is initially put equal to N_{in}, *and* Δ_S is computed using N_{in} positions; $N_n(t)$ is then adapted in this way: while $\Delta_S < \Delta_{min}$ and $N_n(t) < N_{max}$, $N_n(t)$ is increased; while $\Delta_S > \Delta_{max}$ and $N_n(t) > N_{min}$, $N_n(t)$ is decreased.

When the value of $N_n(t)$ respecting the conditions is found, the trajectory components *x(t)* and *y(t)* are approximated, in a least-square sense, as in the first stage, using $N_n(t)$ positions, half backwards and half afterwards, and the velocity and acceleration components $u_x(t)$, $u_y(t)$, $a_x(t)$, $a_y(t)$ computed via time derivatives.

Δ_S is so the bulk parameter of PTVA, because it allows to vary the number of positions used for trajectory approximation depending on where the particle is in the flow (see the Eulerian field of N_n on Figure 4.11 and 4.12): for example, when a particle is travelling along an almost straight trajectory with a constant velocity, Δ_S tends to zero (because $\sum_{i=-N_n(t)/2}^{i=N_n(t)/2} \left\| \vec{x}_{i+1} - \vec{x}_i \right\|$ is almost equal to $\overline{\vec{u}}\Delta t$) and consequently the number of position for the approximation is increased; when a particle, is trapped in the smallest vortical structure of the flow, Δ_S reach Δ_{TARGET} exactly after one loop (because, after one loop, $\overline{\vec{u}}\Delta t$ goes to zero). When $\overline{\vec{u}} \neq 0$, the smallest eddy that can be tracked by the trajectory extrapolation is a convected eddy. This can be achieved with polynomial functions of order larger than three.

It should be highlighted that the only key parameter that one has to choose is a physical parameter of the flow, Δ_{TARGET}, i.e. the perimeter of the smallest eddy one wants to measure (or can measure, because of technical limitation due to experimental factors such as particle diameter, camera spatial resolution, etc.).

As discussed later, it should be noticed that the largest impact on the quality of the acceleration measurement comes from this mean Lagrangian velocity correction rather than the order of the polynomial function used to locally approximate the trajectories.

4.4 PTVA: feedback on quality

For each acceleration measurements, i.e. for each position, the PTVA algorithm provides as a feedback the standard deviation of the positions noise, σ_{noise}, i.e. the standard deviation of the distances among the positions extracted by the PTV codes and the position of the approximated trajectory. The ratio $\sigma_{noise} / \Delta_S$ gives a good feedback on the quality of the acceleration measurement (with $N_n(t)\,\sigma_{noise} / \Delta_S << 1$ when $\vec{a} \neq \vec{0}$); on the Figure 4.13 and 4.14 (section 7) the probability density functions of this parameter on the experiments will be shown. This ratio $\sigma_{noise} / \Delta_S$ will be later used to characterize (and validate) the quality of the acceleration measurement according to the noise level. In the experimental conditions encountered here, the total noise level, $N_n(t)\,\sigma_{noise}$, is low compared to the displacement used for tracking Δ_s. As this could not be the case with for other experiments because of the high level of noise (high σ_{noise}) or of a too high sampling frequency (high $N_n(t)\,\sigma_{noise}$ leading to over-sampling, see for example the case b2 on Figure 4.2), an additional correcting term - $N_n(t)\,\sigma_{noise}$ should be added to equation (4.12), leading to

$$\Delta_S = \sum_{i=-N_n(t)/2}^{i=N_n(t)/2} \left\| \vec{x}_{i+1} - \vec{x}_i - \bar{\bar{u}}\Delta t \right\| - \mathrm{N_n}(t)\sigma_{noise} \tag{4.13}$$

The main disadvantage of this correction is that, with this correction, the method will often tend towards the maximum number of positions allowed (i.e., all the positions available for one trajectory), with the measure becoming more a problem of noise filtering. Anyway, in the experiments object of this work (performed with a high spatial resolution, a low acquisition frequency and a low level of noise) this correction was not needed.

5 PTVA: VALIDATION AND MEASUREMENT ACCURACY

In this section, the PTVA method will be validated via a quantitative evaluation of its accuracy in measuring velocity and acceleration, together with a comparison of its accuracy with the one previous method (section 5.1). The performance of the different methods was also compared on the multi-scale flow object of this work (section 5.2).

For this, an approach which makes use of trajectories generated via geometrical considerations, with and without sweeping effect and time dependency, have been chosen: the advantage of this approach is that positions, velocities and accelerations of the trajectories are exactly known. The accuracy is subsequently evaluated via the quantification of the error of the method on velocity and acceleration measurements compared to the real value, according to the intensity of a noise added to the geometrical trajectories.

5.1 Geometrical approach

As briefly stated above, the geometrical approach chosen for the validation is based on a set of geometrical trajectories, analytically defined, whose exact velocity and acceleration is known in each point. These geometrical trajectories can be considered as a synthesis of the trajectories present in a real flow. Their velocity is adjusted so as to have similar maximum velocities between these geometrical trajectories and the one measured in the experiments. Different parameters (noise, convection, time dependency) are combined to give numerous sets of parameters; to reinforce the statistics, the validation is performed on each set over more than 1000 trajectories and than $2 \cdot 10^6$ positions.

5.1.1 Choice of geometrical structures

Equations (4.10) give different two-dimensional velocity fields according to the values of G and K ($-1 \leq K \leq 1$): in particular, $-1 \leq K < 0$ corresponds to a velocity field with an elliptical stagnation point in (x_0 , y_0) and vortical trajectories, $K = 0$ to an unidirectional shear flow and $0 < K \leq 1$ to a velocity field with a hyperbolic stagnation point in (x_0 , y_0), see Ottino (1989).

$$\begin{cases} u = G(y - y_0) \\ v = KG(x - x_0) \end{cases} \tag{4.14}$$

G is chosen in order to have a maximum velocity on each trajectory close to the maximum velocity measured in the flow (50 pixel/s, corresponding to about 25 mm/s). A Galilean transformation of this velocity fields is obtained in equations (4.11): $\vec{U}_C$ is the convective velocity (with components U_{Cx} and U_{Cy}) of flow structures than we define in the frame $\vec{U}_C = 0$. x_0 and y_0 are the centre of the geometrical structures considered and corresponds to the position of the stagnation point in the convective frame, while t is the time.

$$\begin{cases} u = G(y - y_0) + GU_{Cy}t - U_{Cx} \\ v = KG(x - x_0) + KGU_{Cx}t - U_{Cy} \end{cases} \tag{4.15}$$

At time t = 0, the stagnation point of a convected structure is at (x_0 , y_0) in the observer frame. This reference point is moving with velocity $-\vec{U}_C$ in the observer frame. To quantify this convection (or sweeping) according to the intensity of the flow structures, the root mean square of the velocity $\vec{u}_{RMS}$ (for each trajectory), considered the characteristic velocity of that particular trajectory, is computed and then the convection coefficient C_{CONV} is calculated as $C_{CONV} = \frac{\vec{U}_C}{\vec{u}_{RMS}}$. Later on, the quality of the acceleration measurement according to different values of C_{CONV} is studied. By the way, when C_{CONV} = 0 there is not any convection/sweeping, when C_{CONV} = 1 the convection/sweeping is comparable to the velocity intensity, increasing the difficulty of the acceleration measurements (see equation 1.2). It should be noticed that, as in the flow object of this work there is no convection, this is done in order to put in troubles the PTVA methods and find out its limits.

5.1.2 Two type of noise with a controlled intensity

After that trajectories are generated in conjunction with their velocities and accelerations, a noise of controlled the amplitude is added to the trajectories, such as to analyze the sensibility of the measurement accuracy to the measurement noise. To do that, two different kinds of noise are used: the first one is a Gaussian noise with a selected standard deviation, the second one is a directional noise of selected amplitude. The latter is defined, point-by-point, by an angle and a distance, both randomly generated following an uniform distribution (bounded between 0 and 2π for the angle and between 0 and a selected amplitude for the distance). The values of the noise intensity (0 pixel, 0.03 pixel, 0.06 pixel, 0.1 pixel, 0.2 pixel, 0.3 pixel, 0.6 pixel and 1 pixel) have been chosen to broadly cover the typical noise found in this experiment (approx. 0.056 pixel). In order to have nondimensional values and in agreement with what shown in section 4.4 about the index of the measurement quality ratio $\sigma_{noise} / \Delta_S$, in the following section the noise magnitude are normalized with Δ_{TARGET}. This parameter has here a value equal to 25.12 pixel, corresponding to a diameter of the smallest eddy to be tracked of 8 pixels, which is the value used in PTVA for the measurement on the geometrical trajectories. This value has been chosen for two reasons: it is the one used in the laboratory experiments object of this work with the large frame (see section 5 of chapter 3); moreover, it is much smaller than the smallest diameter of the geometrical trajectories generated with equations 4.11 and so it does not introduce any artificial smoothing on the trajectories. The values of $\sigma_{noise} / \Delta_{TARGET}$ used for the validation are so 0, 0.0012, 0.00239, 0.00398, 0.00796, 0.01194, 0.02387 and 0.03979, while on the laboratory experiments a typical value of 0.0065 was found (see section 7 and Figures 4.13 and 4.14).

5.1.3 Accuracy of the PTVA method

The validation starts with the convected structures generated by equations (4.15), and values of the convection coefficient C_{CONV} of 0, 0.1 and 1. Figure 4.3 shows the average percentage errors of PTVA on the velocity (vg are the errors on velocity for the Gaussian noise, vc are the errors on velocity for the circular noise) and acceleration (ag are the errors on acceleration for the Gaussian noise, ac are the errors on acceleration for the circular noise) versus the ratio $\sigma_{noise} / \Delta_{TARGET}$, with $\Delta_s \cong \Delta_{TARGET}$; the symbols corresponds to the different cases of convection, with a circle for $C_{CONV} = 0$, a square for $C_{CONV} = 0.1$ and a triangle for $C_{CONV} = 1$. The percentage error on acceleration is performed on each point as

$$error = \frac{\left\| \vec{a}_{REAL} - \vec{a}_{MEAS} \right\|}{\vec{a}_{REAL}} \tag{4.16}$$

and in a similar way for the velocity.

The curves clearly show a fast increase of the of the measurement error with the increase of $\sigma_{noise} / \Delta_{TARGET}$. The velocity measurements are much more accurate than the acceleration measurements: in particular, the error on the acceleration is larger than more of one order of magnitude than the one on velocity. For values of $\sigma_{noise} / \Delta_{TARGET} <$ 0.008, the errors are found to be smaller than 10% for acceleration (curves ag and ac) and smaller than 0.8% for velocity (curves vg and vc).

When the convection intensity varies, no significant differences are found using PTVA on the accuracy of the acceleration and velocity: this shows that the PTVA method is robust to convection. The increase of the errors with $\sigma_{noise} / \Delta_{TARGET}$ can be roughly approximated as a power law, so as to represent the sensitivity of the measure accuracy to an increase of this ratio. It was found that the acceleration errors increase like $(\sigma_{noise} / \Delta_{TARGET})^{2.44\pm0.05}$ and the velocity errors increase like $(\sigma_{noise} / \Delta_{TARGET})^{2.06\pm0.15}$. This confirms the strongest sensitivity to the noise intensity of the acceleration measurement when compared to the velocity measurements.

According to the experimental conditions, with a typical $\sigma_{noise} / \Delta_S \cong 0.0065$, the errors of the measurements are expected to be about 0.44% on the velocity and about 6.25% for the acceleration. If PTVA is compared with the previous methods (using $C_{CONV} = 1$ and gaussian noise, i.e. the parameters giving the largest measurement errors, and the same noise) based upon a moving polynomial approximation with a constant number of positions, percentage errors on velocities turn out to be about 3% for order 4 and 2.6% for order 2, and percentage errors on acceleration about 25% for order 4 and 23.6% for order 2. It should be noticed that three different numbers of positions have been chosen (the two most probable numbers of positions used by PTVA, that is 25 and 233, and the mean value between them, 129) for the methods using a fixed number of positions and their best performance is the one shown above. If the same velocity measurements are performed through a simple division of the space covered over three time

steps by the time interval (one of the first method used to compute velocity from PTV measurements), the percentage error goes to 120.76%. Clearly PTVA is much more accurate than previous methods: 6 time more accurate on the velocity measure and 4 times more accurate on the acceleration measure. Nevertheless, these results show that a relatively low level of noise is important for the quality of the measurement.

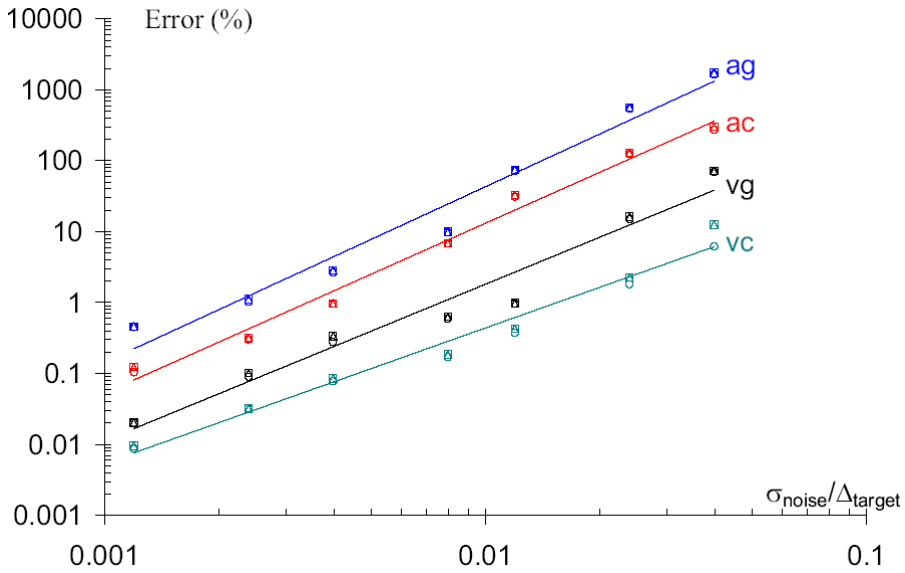

Figure 4.3 Percentage errors of PTVA on the velocity (vg are the errors on velocity for the Gaussian noise, vc are the errors on velocity for the circular noise) and acceleration (ag are the errors on acceleration for the Gaussian noise, ac are the errors on acceleration for the circular noise) versus the ratio $\sigma_{noise} / \Delta_{TARGET}$, with $\Delta_s \cong \Delta_{TARGET}$; the symbols corresponds to the different cases of convection, with a circle for $C_{CONV} = 0$, a square for $C_{CONV} = 0.1$ and a triangle for $C_{CONV} = 1$.

Anyway it should be highlighted that, in order to obtain a good accuracy, the noise should be kept small compared to the displacement of the particles, and thus small compared to Δ_S and Δ_{TARGET}, at least of one order of magnitude.

As a simple convection do not alter the accuracy of the PTVA method, a time dependency of the convected geometrical structure of equation 4.14 is introduced by varying k following the equation

$$k(t) = \frac{t}{t_{\max}} \sin\left(2\pi \frac{t}{\alpha_T \Delta t}\right) \tag{4.17}$$

where t is the time, t_{max} the duration of the tracking (so as to have k bounded between

±1), Δt is the time step of the tracking and α_T is the number of tracked positions per period. This leads to periodic changes in the flow structure geometry with an increase in the speed/amplitude of these changes with time. It can then be considered as a difficult test case where the analytical solution is known for velocity and acceleration as in the steady case.

The same parameters for noise and convection previously cited are then applied to these trajectories. An example of a trajectory generated with *k(t)* for two different convection coefficients C_{CONV} is shown on Figure 4.4. Figure 4.5 shows the percentage errors of PTVA in the measure of velocity and acceleration, for the same conditions than figure 4.3 but on the time dependent flow structures. Again, the values of PTVA errors are not strongly affected by the convection. For $C_{CONV} = 1$ and a Gaussian noise (worst case giving the largest percentage errors) and with the typical ratio $\sigma_{noise} / \Delta_S \cong 0.0065$ of the experiments, a percentage error of 2% is found on velocity and of 15.2% for acceleration. The methods using a polynomial approximations of order n with a constant number of positions N cause (in the same conditions and for the best result coming out from three different N) percentage errors of about 15.8% on the velocity and 48.3% on the acceleration for $n = 4$ and of about 17.3% on the velocity and 89.6% on the acceleration for $n = 2$. If the same velocity measurements are performed through a simple division of the space covered over three time steps by the time interval (one of the first method used to compute velocity from PTV measurements), the percentage error goes to 863.47%.

Even if the time dependency is found to increase the errors of PTVA, it is found to be still much more accurate than previous method on both velocity (almost eight times more precise) and acceleration (more than three) and without any issue regarding the correct number of position to be used.

It should be noticed that the type of the noise and the order of the polynomial interpolation are more important with a time dependent flow structure. Here above the worst case for PTVA was used for the comparison, whilst with a circular noise the percentage errors are only of about 0.8% on the velocity and of about 5.7% on the acceleration. Attempting to fit the evolution of the errors with the ratio ($\sigma_{noise} / \Delta_{TARGET}$) by a power law so as to provide a typical growth of errors with noise, it has been found that the acceleration percentage errors increase like $(\sigma_{noise} / \Delta_{TARGET})^{2.5\pm0.5}$ and the velocity percentage errors increase like $(\sigma_{noise} / \Delta_{TARGET})^{1.5\pm0.3}$. The larger discrepancy of the exponents comes from the strong influence of the noise's type.

In order to complete this quantitative validation of the PTVA method, the effect of the sampling/acquisition frequency has been studied. In Figure 4.6, the percentage errors on the velocity and acceleration measures are plotted versus α_T, that is the number of tracked positions per period: varying α_T corresponds to vary the acquisition frequency of the camera for a given characteristic time scale (which corresponds here to one period) or to vary the sampling frequency on a trajectory of known characteristics (as in this validation).

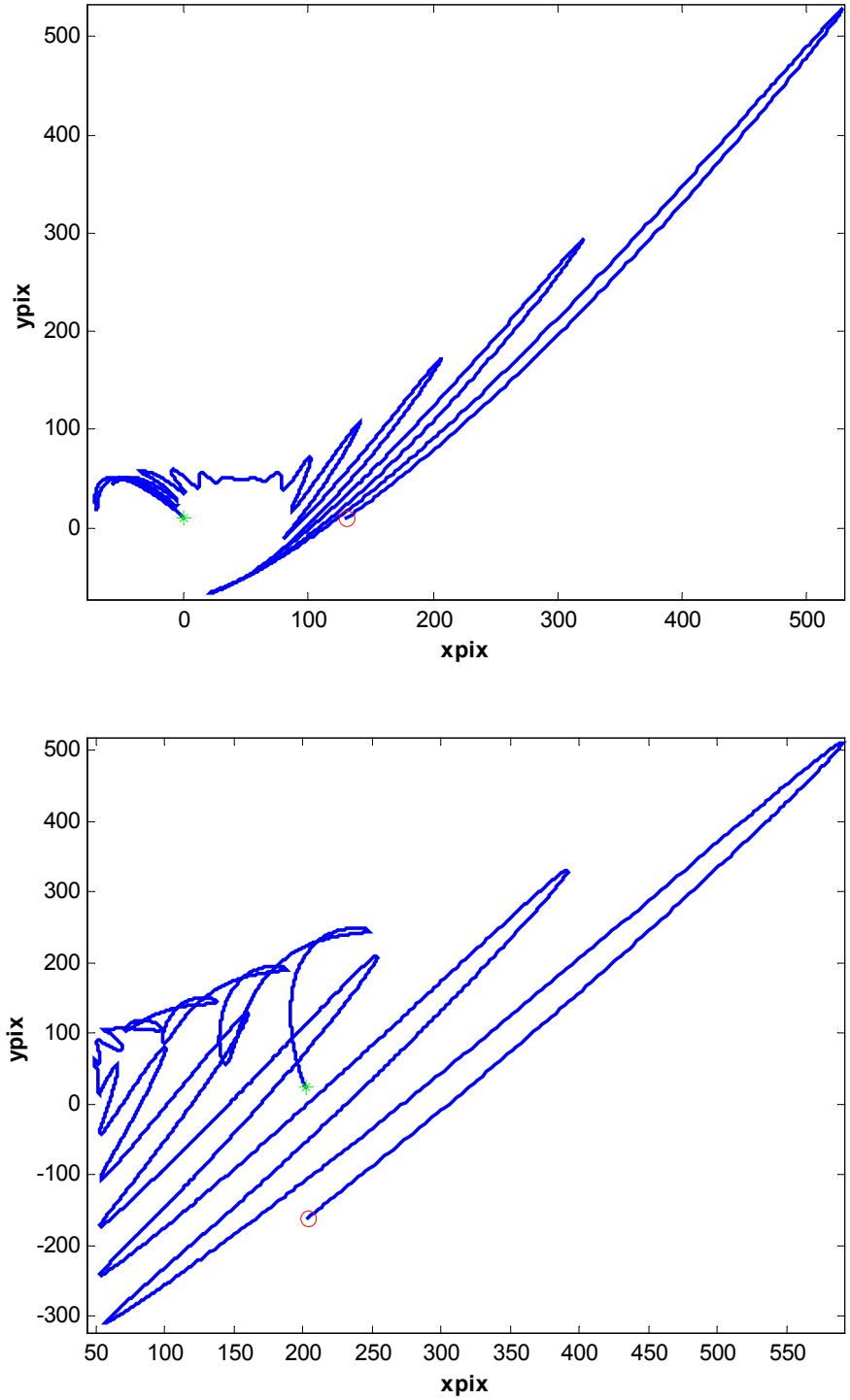

Figure 4.4 Trajectory generated with the time dependent k(t) of equation 4.16 with different convective velocity: above, $C_{CONV} = 0$, below, $C_{CONV} = 1$.

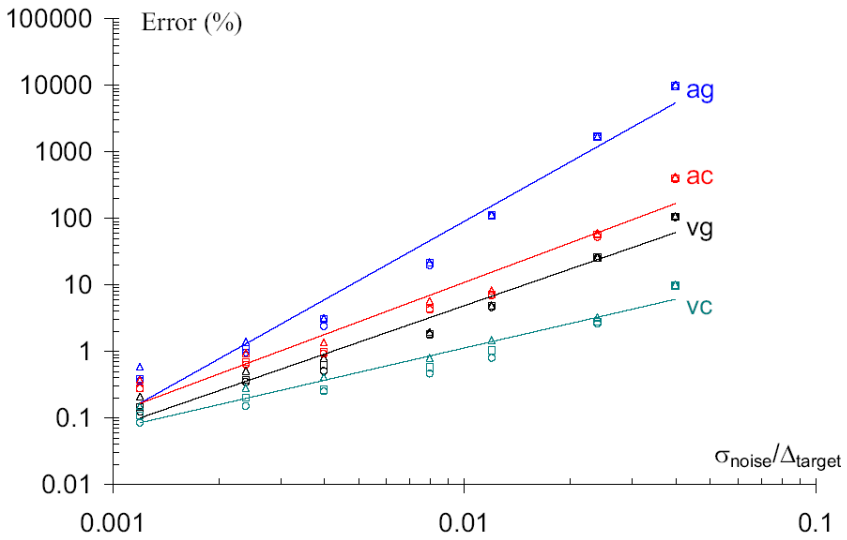

Figure 4.5 Percentage errors of PTVA on the velocity (vg are the errors on velocity for the Gaussian noise, vc are the errors on velocity for the circular noise) and acceleration (ag are the errors on acceleration for the Gaussian noise, ac are the errors on acceleration for the circular noise) versus the ratio $\sigma_{noise} / \Delta_{TARGET}$, with $\Delta_s \cong \Delta_{TARGET}$ for time dependent flow structure; the symbols corresponds to the different cases of convection, with a circle for $C_{CONV} = 0$, a square for $C_{CONV} = 0.1$ and a triangle for $C_{CONV} = 1$.

In particular, on Figure 4.6 vg004 indicates the errors on velocity for a Gaussian noise with ratio $\sigma_{noise} / \Delta_{TARGET} \cong 0.004$, vg008 the errors on velocity for a Gaussian noise with ratio $\sigma_{noise} / \Delta_{TARGET} \cong 0.008$, ag004 the errors on acceleration for a Gaussian noise with ratio $\sigma_{noise} / \Delta_{TARGET} \cong 0.004$, ag008 the errors on acceleration for a Gaussian noise with ratio $\sigma_{noise} / \Delta_{TARGET} \cong 0.008$.

When dividing α_T by two (from $\alpha_T = 628$), the quality of the velocity and acceleration measurements is not affected, as PTVA is self-adapting. For divisions of the frequency larger than four ($\alpha_T < 256$), the errors start to grow as power laws of α_T ($\sim \alpha_T^{-0.67}$ on curve vg004, $\sim \alpha_T^{-1.22}$ on curve vg008, $\sim \alpha_T^{-0.57}$ on curve ag004 and $\sim \alpha_T^{-0.74}$ on curve ag008). This is due to a reduction of the quality of the temporal sampling compared to the strong unsteadiness of the flow. Nevertheless, the fact that PTVA method stays relatively robust for a broad range of sampling frequencies (more than one decade, $39 \leq \sim \alpha_T \leq 628$) is noticeable.

Moreover, as very different accuracy come out from a fourth order moving polynomial approximation using a fixed number of positions and the PTVA using the same polynomial approximation, it could be deduced that the increase in accuracy showed above does not derive from the order of the polynomial but from the adaptive number of positions and from the convection removal.

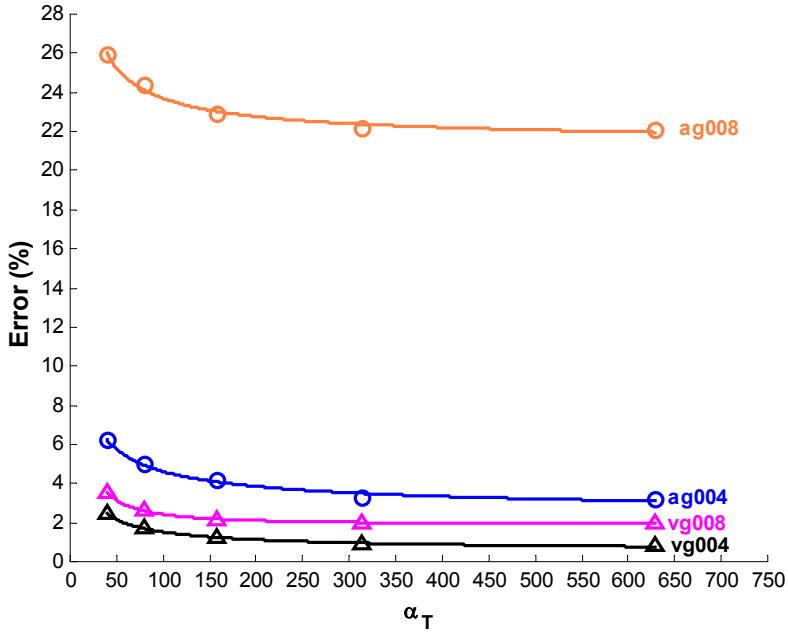

Figure 4.6 Percentage errors of PTVA on the velocity (vg004 are the errors on velocity for a Gaussian noise with ratio $\sigma_{noise} / \Delta_{TARGET} \cong 0.004$, vg008 are the errors on velocity for a Gaussian noise with ratio $\sigma_{noise} / \Delta_{TARGET} \cong 0.008$) and on the acceleration (ag004 are the errors on acceleration for a Gaussian noise with ratio $\sigma_{noise} / \Delta_{TARGET} \cong 0.004$, ag008 are the errors on acceleration for a Gaussian noise with ratio $\sigma_{noise} / \Delta_{TARGET} \cong 0.008$) versus the sampling coefficient α_T.

6 COMPARISON OF PTVA WITH PREVIOUS METHODS ON A QUASI-TWO-DIMENSIONAL MULTIPLE-SCALE ELECTROMAGNETICALLY-CONTROLLED FLOW

In order to show the different performances of PTVA and of the other methods based on Particle Tracking on the multi-scale flow object of this work, some selected trajectories extracted by PTV have been given as an input to the various methods, i.e. to the PTVA, to two methods based on a moving polynomial approximation (of order two and four, respectively) with a fixed number of positions and to one of the first method used in PTV, the division of the space covered over three time steps by the time interval. These trajectories (see Figure 4.7) have been chosen as a ”synthesis” of the flow: in fact, the black one (which crosses the North big magnet, so experiencing the highest velocities in the flow while travelling along an almost straight line, and then goes close to the large scale hyperbolic stagnation point) and the blue one are typical of the large scales of the flow, the red one (which goes close to a medium scales hyperbolic stagnation point and then describes an eight of the same scale) and the magenta one (which rotates around an elliptical stagnation point of the medium scale) are representative of the medium scales, while the green one (which travels close to both an elliptical and a hyperbolic stagnation points of the small scales) identifies some features of the small scales. The trajectories, each one with one thousand positions, are taken from run 12 of the second campaign of measurements on the flow with constant forcing (see section 5.1 of Chapter 3).

Regarding the values of the PTVA parameters (see section 4.3) used on the experimental data (and on the trajectories of this section) to measure velocity and acceleration, an input diameter ϕ_{ed} of 4 mm (equivalent to 8 pixel in the large investigation window and 10 pixel in the small one, respectively $\Delta_{TARGET} \cong 25.1$ pixel and $\Delta_{TARGET} \cong 31.4$ pixel) has been used for the PTVA method. These values are much smaller than the small magnet size (10 mm) and smaller than the smallest eddy effectively tracked (5 mm of diameter), so the method does not introduce an artificial smoothing even at the small scales of the flow. Moreover, in the first stage the following values were used (see section 4.3.1): $N_{in} = 15$, $N_{min} = 11$, $N_{max} = 128$, $\Delta_{min} = 11$ pixel and $\Delta_{max} = 60$ pixel; in the second stage the following values were used (see section 4.3.2): $N_{in} = 63$, $N_{min} = 11$, $N_{max} = 263$, $\Delta_{S\min} = \frac{\Delta_{TARGET}}{2}$ ($\cong 12.6$ pixel in the large investigation window and $\cong 15.7$ pixel in the small one) and $\Delta_{S\max} = \frac{3}{2}\Delta_{TARGET}$ ($\cong 37.7$ pixel in the large investigation window and $\cong 47.1$ pixel in the small one).

Regarding the two methods object of the comparison, based on a moving polynomial approximation with a fixed number of positions, this has been chosen equal to 25, which turns out to be the best case for both these methods. It should be noticed that this value is one of the local maximum for the probability density function of the number of positions used by the PTVA method (see section 7).

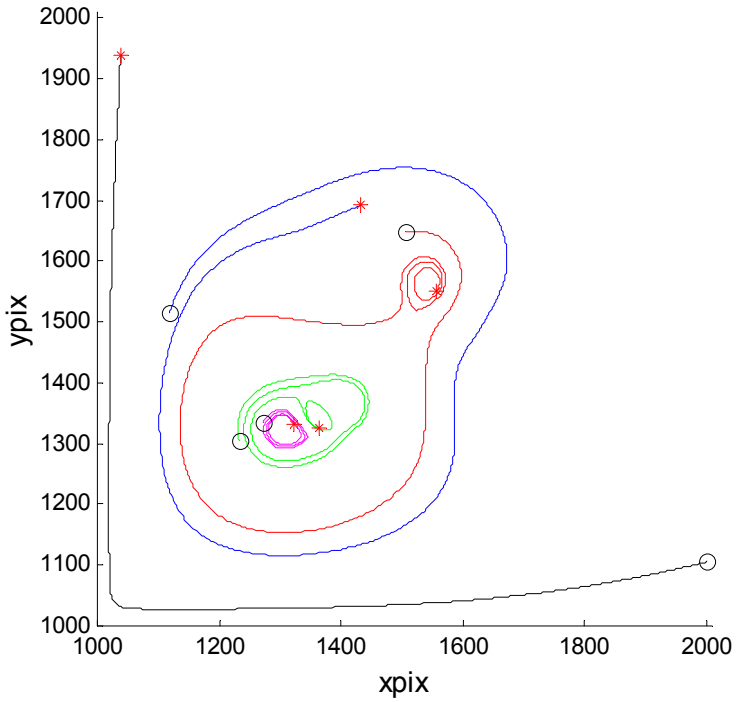

Figure 4.7 Trajectories chosen for the comparison among PTVA and previous methods; a red asterisk marks the first point, a black circle the last one.

Figure 4.8 gives the comparison of the measured velocity x-components, for the trajectories of figure 4.7 (same colours), versus time, extracted from the four methods: except for the method implying the simple division of the space covered over three time steps by the time interval, the measures by PTVA is slightly better than the others, particularly because it does not show any of outlier that instead arise from the other measurement methods (compare red, magenta and green curves), but the differences are not so evident.

A completely different situation arises when the comparison is made among the measured acceleration x-component (Figure 4.9): it is clear that, if the method implying the division of space by time measures only noise, PTVA is able to provide an accurate measure of the acceleration, less noisy than the other two methods and without the outliers that arise from them (see, for example, green, red and magenta trajectories). It is also noticeable that PTVA is able to measure sudden change in the acceleration sign and thus shows a good sensitivity to inflection points, see for example the blue curves.

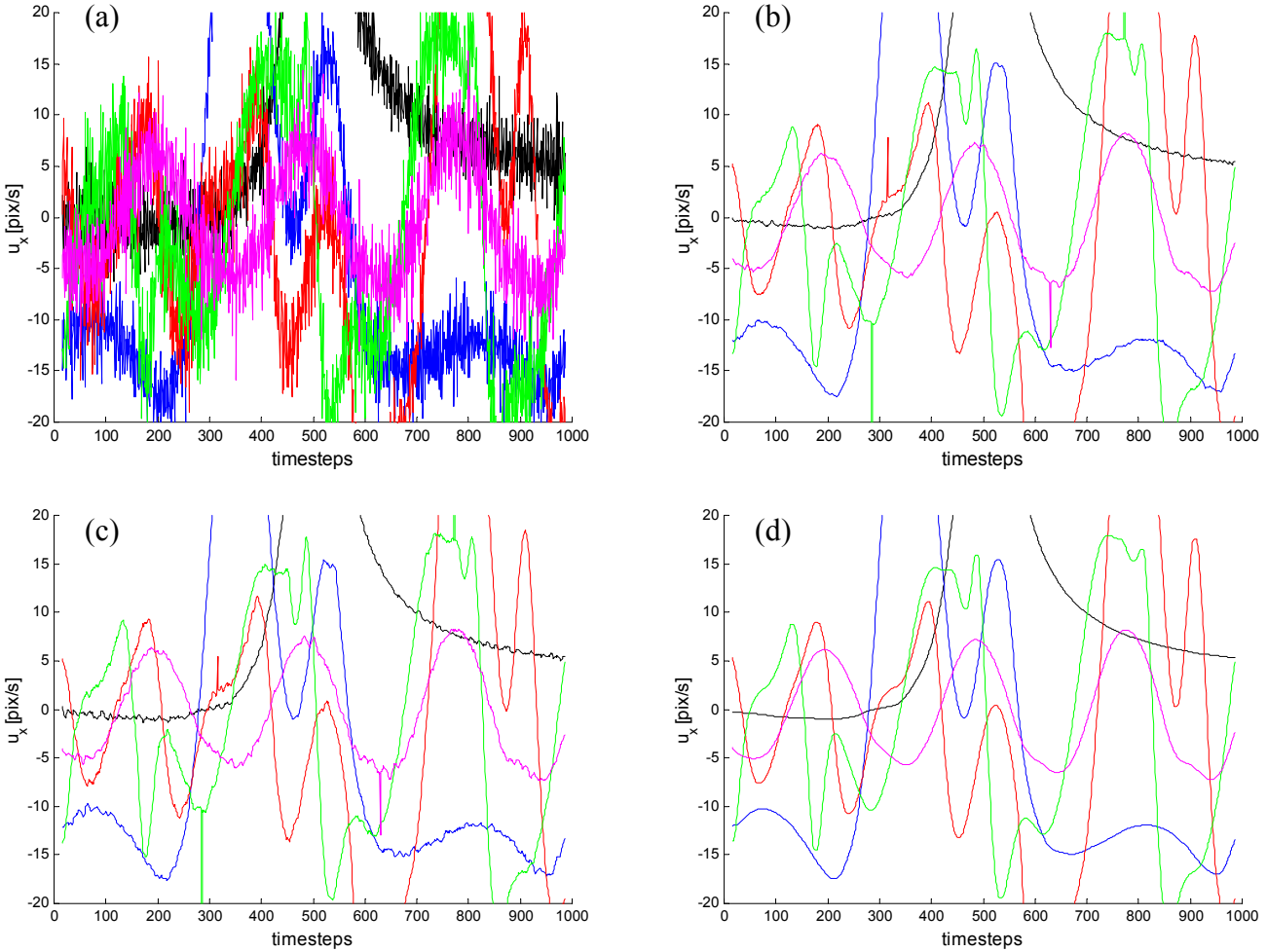

Figure 4.8 Comparison among the x-component of the Lagrangian velocity measured by different methods, along the trajectory of Figure 4.7, versus time: (a) division of the space covered over three time steps by the time interval; (b) moving polynomial approximation of order two with a fixed number of positions; (c) moving polynomial approximation of order four with a fixed number of positions; (d) PTVA; same colours as Figure 4.7.

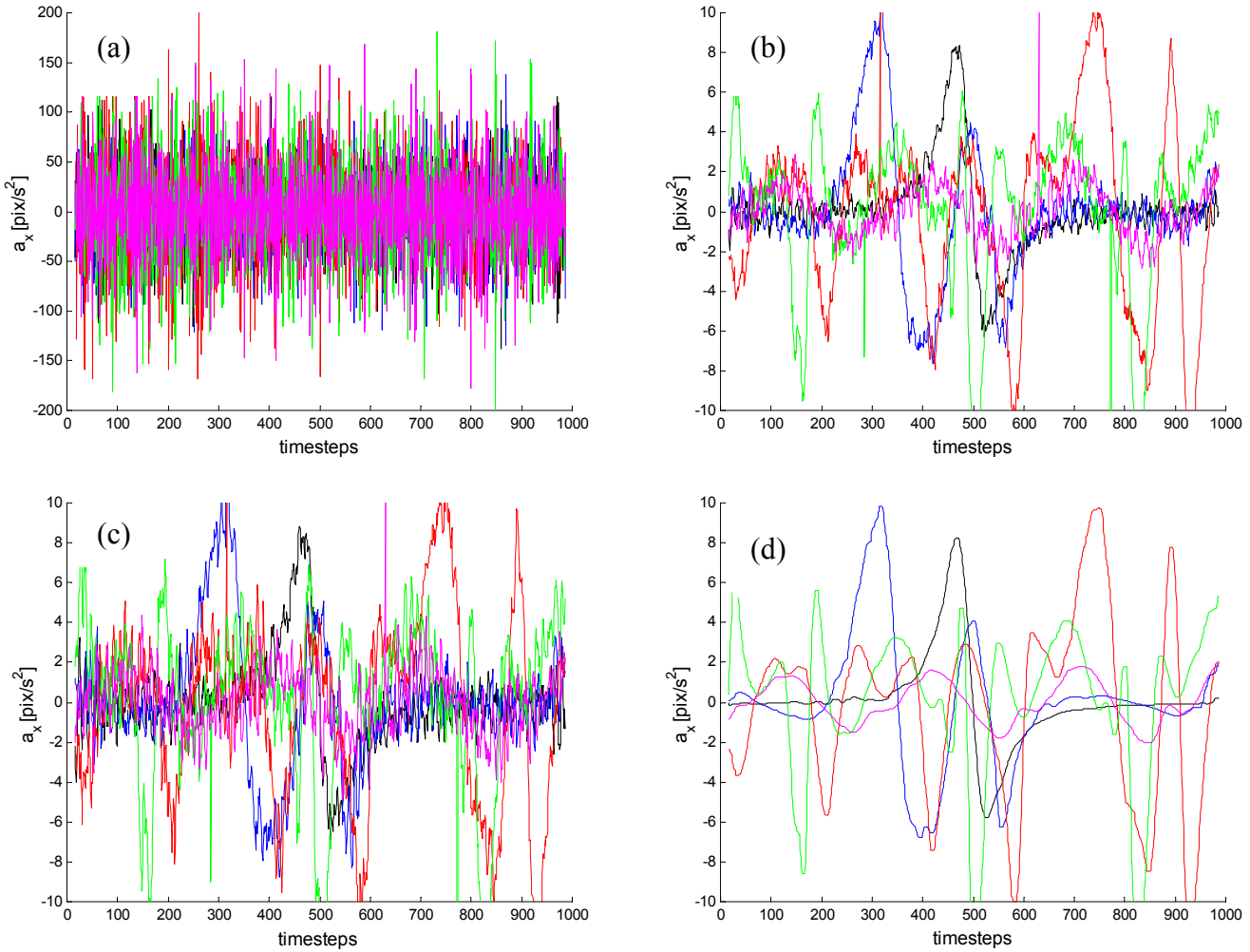

Figure 4.9 Comparison among the x-component of the Lagrangian acceleration measured by different methods, along the trajectory of Figure 4.7, versus time: (a) temporal derivative of the division of the space covered over three time steps by the time interval; (b) moving polynomial approximation of order two with a fixed number of positions; (c) moving polynomial approximation of order four with a fixed number of positions; (d) PTVA; same colours as Figure 4.7.

7 PTVA'S ADAPTABLE NUMBER OF POSITION AND FEEDBACK ON THE MEASUREMENT QUALITY

Why PTVA is able to provide such better results on the acceleration measurement when compared with previous methods based on Particle Tracking?

As previously stated, the reason is the ability of the method to really adapt to the local characteristics of the flow that is reached through the adaptive number of positions and through the convection removal: this ability permits to effectively remove a large amount of noise from the trajectories without deleting their small fluctuations.

To illustrate the variation of the number of positions N_n used by PTVA, in Figure 4.10 is shown the probability density function of this parameter on the laboratory experiments object of this work: it is clearly visible that there is a continuous distribution of N_n, implying that a single number of positions cannot effectively measure the flow without side effects. The minimum and maximum number of position used by the PTVA algorithm were respectively set to 11 and 267 for these experiments, so they are the boundaries of the probability density. Some peaks of probability are visible on the figure: the peak at 63 is the initial number of positions, the other peaks are at 25, 257 and 263.

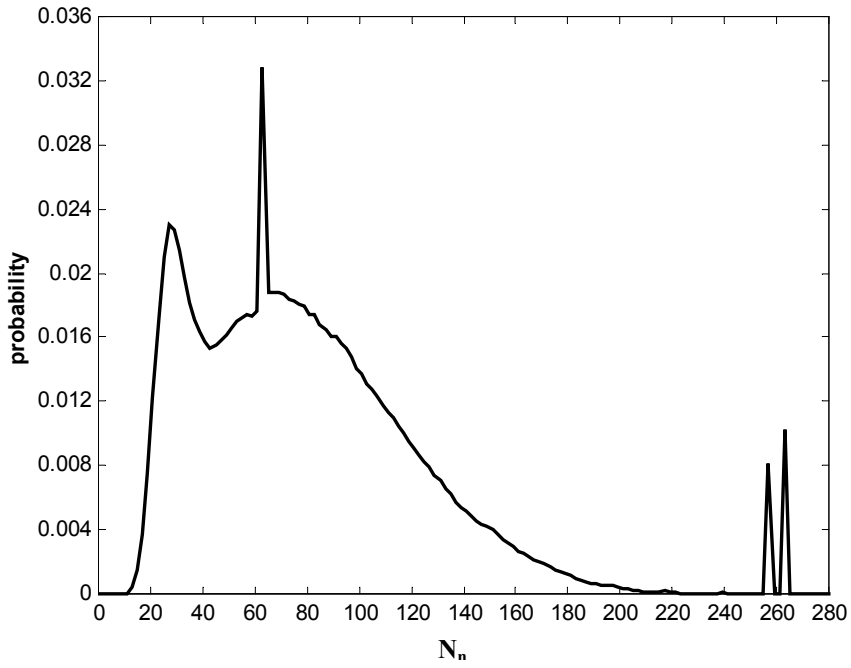

Figure 4.10 Probability density function of the number of position, N_n, used by the PTVA method on the laboratory experiments object of this work; the peak at 63 is the initial number of positions.

To illustrate where these peaks come from according to the topology of the flow but also, more significantly, how PTVA adapts the number of positions N_n to the topology of the acceleration, the Eulerian field (spatial distribution over the investigation field) of N_n used by PTVA is shown in Figure 4.11 together with the Eulerian field of the acceleration.

This figure clearly shows that PTVA really adapts to the local properties of the flow and particularly to the acceleration topology: as a matter of fact, the comparison between the field of N_n and the acceleration one shows that N_n adapts to the intensity of the acceleration so as to accurately measure high values of acceleration as well as low values of acceleration and this at all scales. The two Eulerian fields turn out to be one the negative of the other: local minima of the acceleration correspond to local maxima of N_n and vice versa.

Also if the computation of the Eulerian field implies an average of the values of N_n over a 3·3 pixel cell and over all the runs, causing the extrema of the Eulerian field to be different from the ones of the probability density function of N_n) this map of the N_n allows to identify where the peaks of the pdf arise from: the two peaks with the highest values of N_n in the pdf come from particles travelling with an almost constant velocity in region where the flow is very slow (with very low values of Δ_S that forces the PTVA methods to increase the number of positions as much as possible). The peak with the smallest value of N_n arises instead from particles travelling very close to the local acceleration maxima that are, also, regions where both velocities and streamline curvatures are high (see next chapter).

Similar features can be better observed on Figure 4.12, where a zoom on the South-west quarter of the same two Eulerian fields is shown.

Finally, with the aim of give an insight on the quality of the laboratory measurements object of this work and to allow a comparison with the value of percentage errors previously obtained, in Figure 4.13 the probability density functions of the intensity of the ratio $\sigma_{NOISE} / \Delta_S$ (above) and of its two components (below) are reported. The most probable value of the intensity of $\sigma_{NOISE} / \Delta_S$ is about 0.0065, with a maximum value of 0.94. Similar values are found on the two components of the ratio $\sigma_{NOISE} / \Delta_S$, with most probable values of about 0.0045 for the y component and of about 0.0055 for the x one, and maximum values under 0.09.

As this value is performed for all the points, the quality of the measure can be checked and verified on every single point and, in case, a threshold of the quality can be chosen. It should be noticed anyway that all the measured values are under one tenth, with the largest amount of data well below one hundredth: this explains the good quality of the measurements that will be shown in the next chapter.

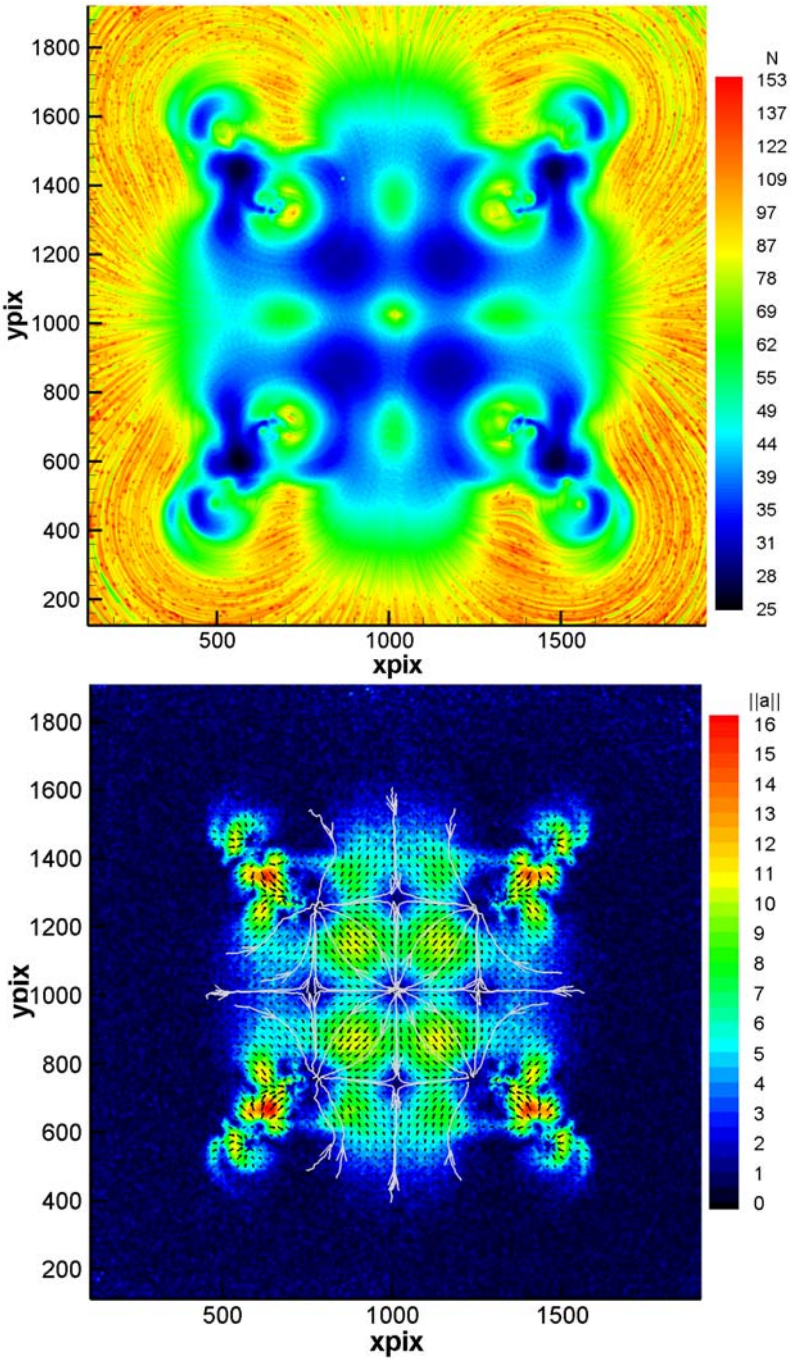

Figure 4.11 Above, the large frame of the Eulerian field of the number of position N_n used by PTVA to fit a moving polynomial of order four on the trajectories; below, the large frame of the acceleration field: the Eulerian acceleration intensity ||a|| is in pixel/s^2, lines correspond to acceleration lines, i.e. lines that on every point are tangential to acceleration vectors (1 arrow for 64 are plotted); 1mm is about 2.02 pixels, the mesh is of 600x600 points with a mesh's size of 3 pixels.

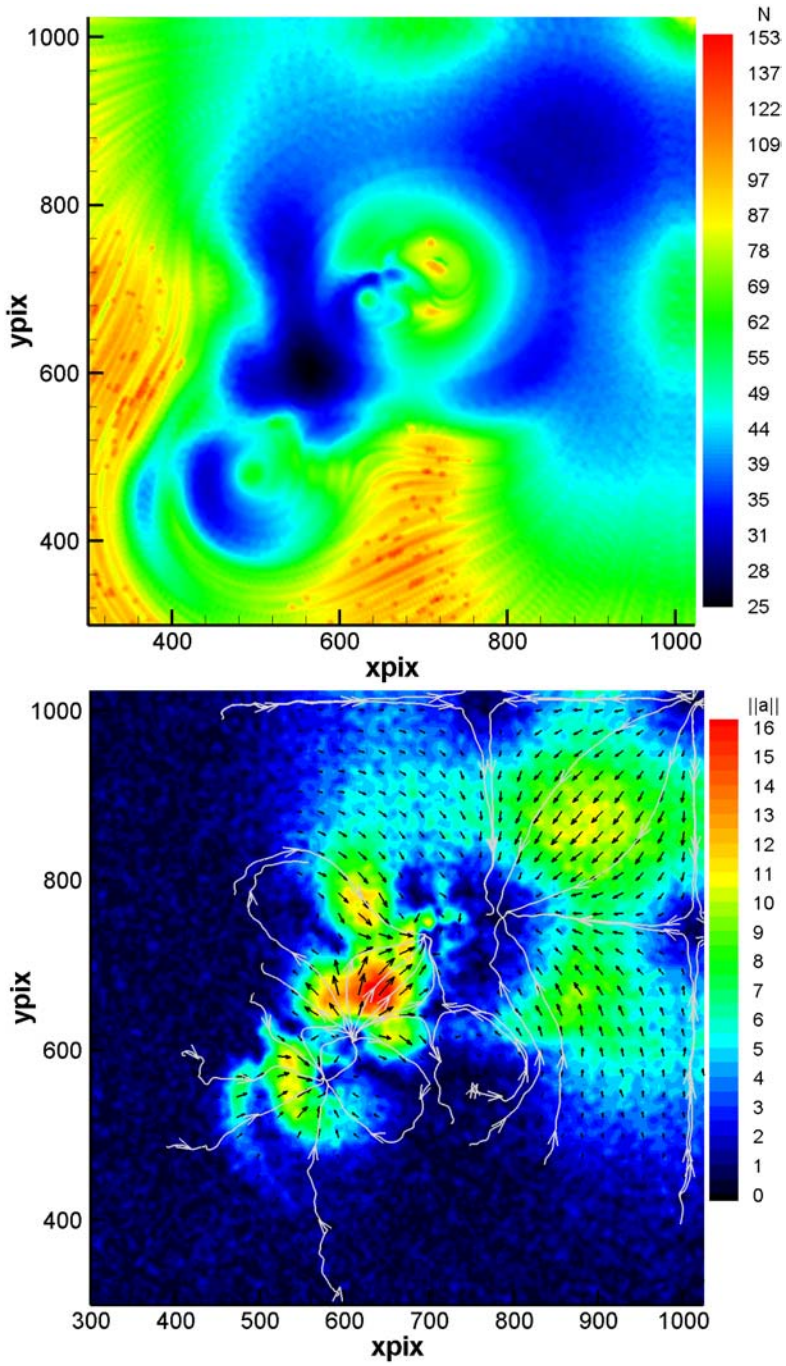

Figure 4.12 Above, a zoom on the South-West quarter of the Eulerian field of the number of position N_n used by PTVA to fit a moving polynomial of order four on the trajectories; below, the same zoom on the Eulerian acceleration field: the acceleration intensity ||a|| is in pixel/s^2, lines correspond to acceleration lines, i.e. lines that on every point are tangential to acceleration vectors (1 arrow for 64 are plotted); 1mm is about 2.02 pixels, the mesh's size of 3 pixels.

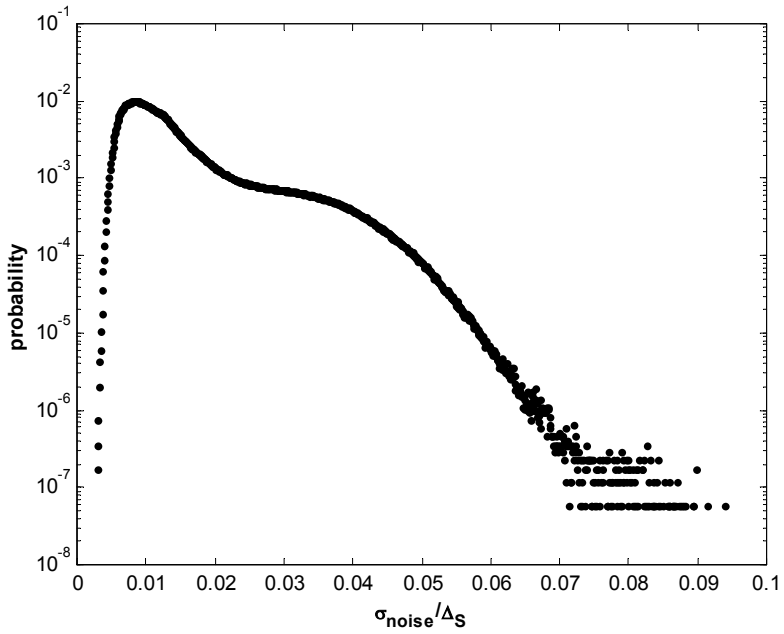

Figure 4.13 Probability Density Function of $\sigma_{NOISE} / \Delta_S$ used by the PTVA method on the laboratory experiments object of this work; the most probable value is about 0.0065.

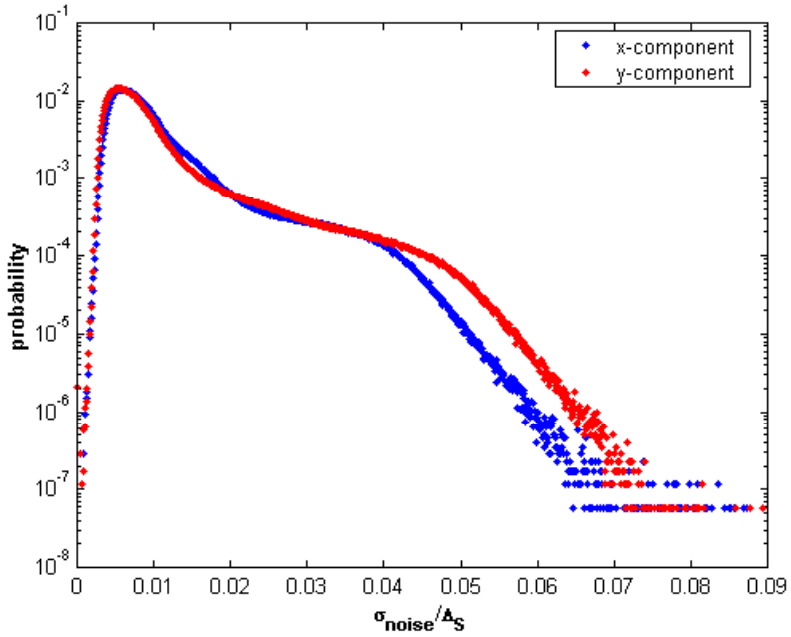

Figure 4.14 Probability Density Function of the x (blue dots) and y (red dots) components of $\sigma_{NOISE} / \Delta_S$ used by the PTVA method on the laboratory experiments object of this work; most probable value is about 0.0045 for y and 0.0055 for x.

5. RESULTS

1 INTRODUCTION

The PTVA method, illustrated in the previous chapter, was born with the target of accurately studying a turbulent-like quasi-two-dimensional electromagnetically-controlled multi-scale flow. As previously stated, this measurement method has shown the ability to extract velocity and acceleration measures with an accuracy at least one order of magnitude higher than previous methods based on PTV, from this flow but also from a more general toy-model flow based on equations 4.10 (see chapter 4). PTVA has encountered basically three development stages: a first one, where the basic idea of an adaptive number of position N to approximate the trajectories with a moving polynomial of order four was tested, based the choice of N only on considerations about the maximum velocity; in a second one, considerations about the maximum and minimum distance admissible to catch the smallest vortex in the flow were introduced, leading to an improvement in the quality of the measurement; finally, the convection removal allowed the definition of Δ_S, the bulk parameter of PTVA, carrying the results showed hereafter.

Some results coming from the PTVA second stage development are reported in Ferrari and Rossi 2006 (a), while the first results from the final version are reported in Ferrari and Rossi 2006 (b) and Rossi and Ferrari 2006. Regarding the results hereafter showed, some of them are part of a journal article by Ferrari and Rossi, 2006c, "Measurements of velocity and acceleration from PTVA, Particle Tracking Velocimetry and Accelerometry, and its application to electromagnetically controlled quasi-two-dimensional multi-scale flows", submitted to the international journal Experiment in Fluids.

The outline of this chapter's first part follows, in some sense, the history of the results extracted by PTVA during its development, so an example of the approximated trajectories will be given, followed by some examples of Lagrangian measures of velocity and acceleration, to then use these data to compute some Lagrangian statistics of velocity and acceleration. Provided the large number of trajectories and the high quality of the measurements, Eulerian measures can be extracted from the Lagrangian ones, so a description of the Eulerian fields (velocity, acceleration, Navier-Stokes equations' viscous term, power input-output, power transformation, as well as divergence of acceleration) over all the investigation area will eventually close this chapter.

All the results presented in this chapter, except where differently written, come from 130 runs of the experiment with a constant forcing.

2 TRAJECTORIES

In Figure 5.1 the trajectories measured for at least one turnover time of the large

scales (19.17 seconds that is equivalent to 192 time steps, as the acquisition rate in all these experiments were 10 frames per second) on eight runs are superimposed: the various colours have the only aim to allow a better distinction of the different trajectories. On the top of Figure 5.1, the entire flow is shown, while on the bottom a zoom on the Southwest quarter of the flow itself allows a better visualization of some features of the small scales. Some circles lay upon the pictures, highlighting the position of some elliptical stagnation points, while the squares shows where some hyperbolic stagnation points arise in the flow; regarding the colours, yellow is used to point the large scales out, red to the medium scales and green to the small ones.

It is clearly visible that PTVA is able to track, for a long time, all the kind of trajectories of the present flow (from very tiny vortices, like the purple one enclosed in the green circle, to straight lines passing over the big magnets and going toward the large scale hyperbolic stagnation point, passing through trajectories travelling between small and medium scales) and at all the scales. In particular, it is noticeable that many trajectories go very close to hyperbolic stagnation point, where velocities are very small but trajectories have a strong curvature and so the tracking is more difficult. Especially interesting from this point of view are two trajectories, a red and a black one, visible on the top right corner of the lower picture of Figure 5.1: the red trajectory belongs to a particle that, travelling toward the centre of the investigation field comes very close to the large scale hyperbolic stagnation point (yellow square on the top of Figure 5.1) and there remains some time; on the contrary, the trajectory related to the black line starts from the same stagnation point and only after some time leaves it to move rightwards. This kind of trajectories carries very useful information to have a complete description of the flow. Hyperbolic stagnation points are so very well defined at all the flow's scales, from large (yellow square) to medium (red squares) to small (green squares) ones, as well as elliptical stagnation points (red circles for medium scales, green for small ones). The same thing can be asserted for the elliptical stagnation points too (see the red and the green circles).

Even if this figure is the result of the overlapping of only eight runs over the 130 carried out (the first eight runs of the second campaign of experiments, see section 5.1 of Chapter 3, for a total number trajectories equal to 3549, each one with a number of points varying from 192 to 1000), almost all the investigation area is already well covered, even the corners and the boundaries where particles enter and exit the filmed field.

Moreover, trajectories turn out to be very smooth, despite the noise typical of PTV measurements: this high degree of noise removal is at the very base of the acceleration measurement that, coming from a double derivative in time, tends to amplify the noise.

3 LAGRANGIAN MEASUREMENTS

In Figure 5.2 an example of instantaneous velocity (picture on the top of the page) and acceleration (picture on the bottom) measured along trajectories extracted from one run (310 trajectories, from the first run of the first campaign of experiments, each one with a length of 1200 points) is shown. In the cited figure, the colours close to the

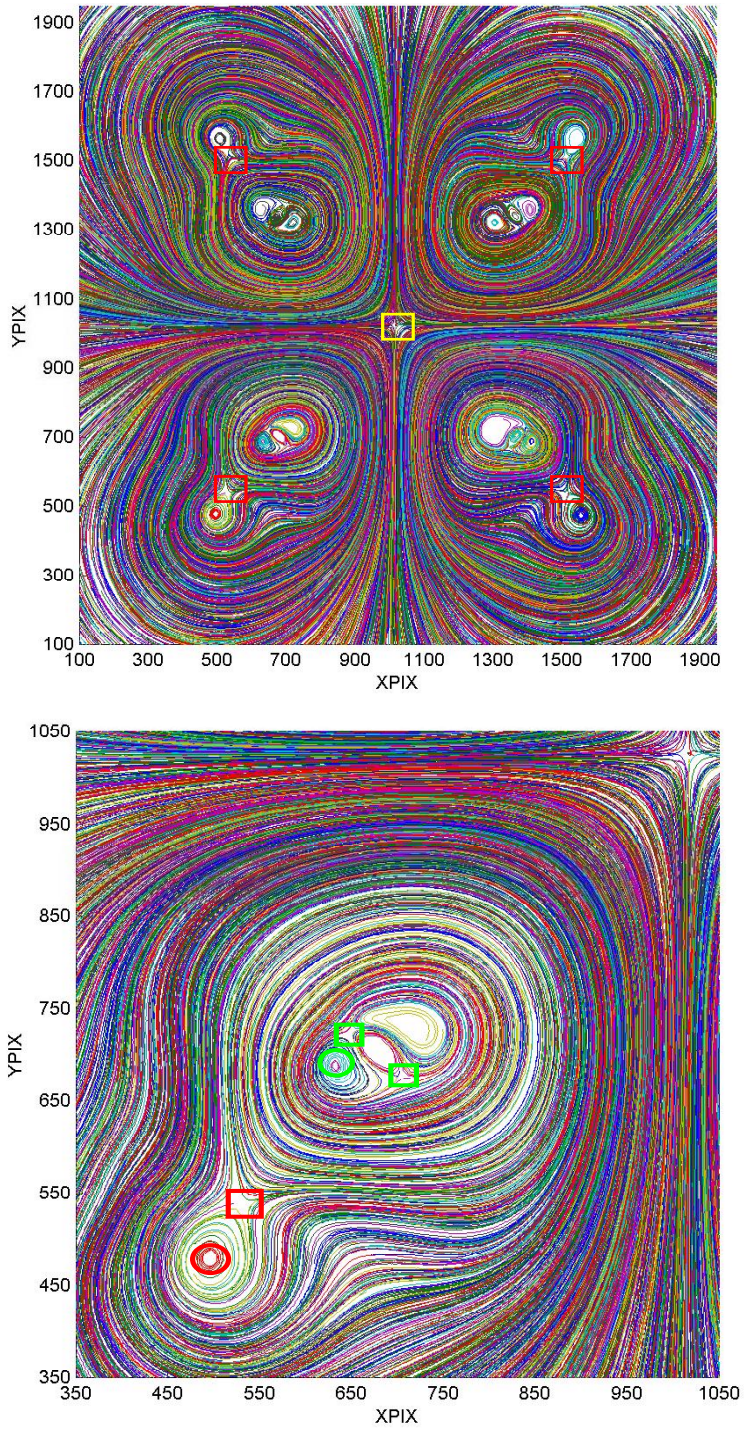

Figure 5.1 Examples of tracked trajectories over eight runs: on the top, the entire flow, below a zoom on the Southwest quarter of it; 1 pixel is about 0.495 mm; circles highlight elliptical stagnation points, squares hyperbolic ones.

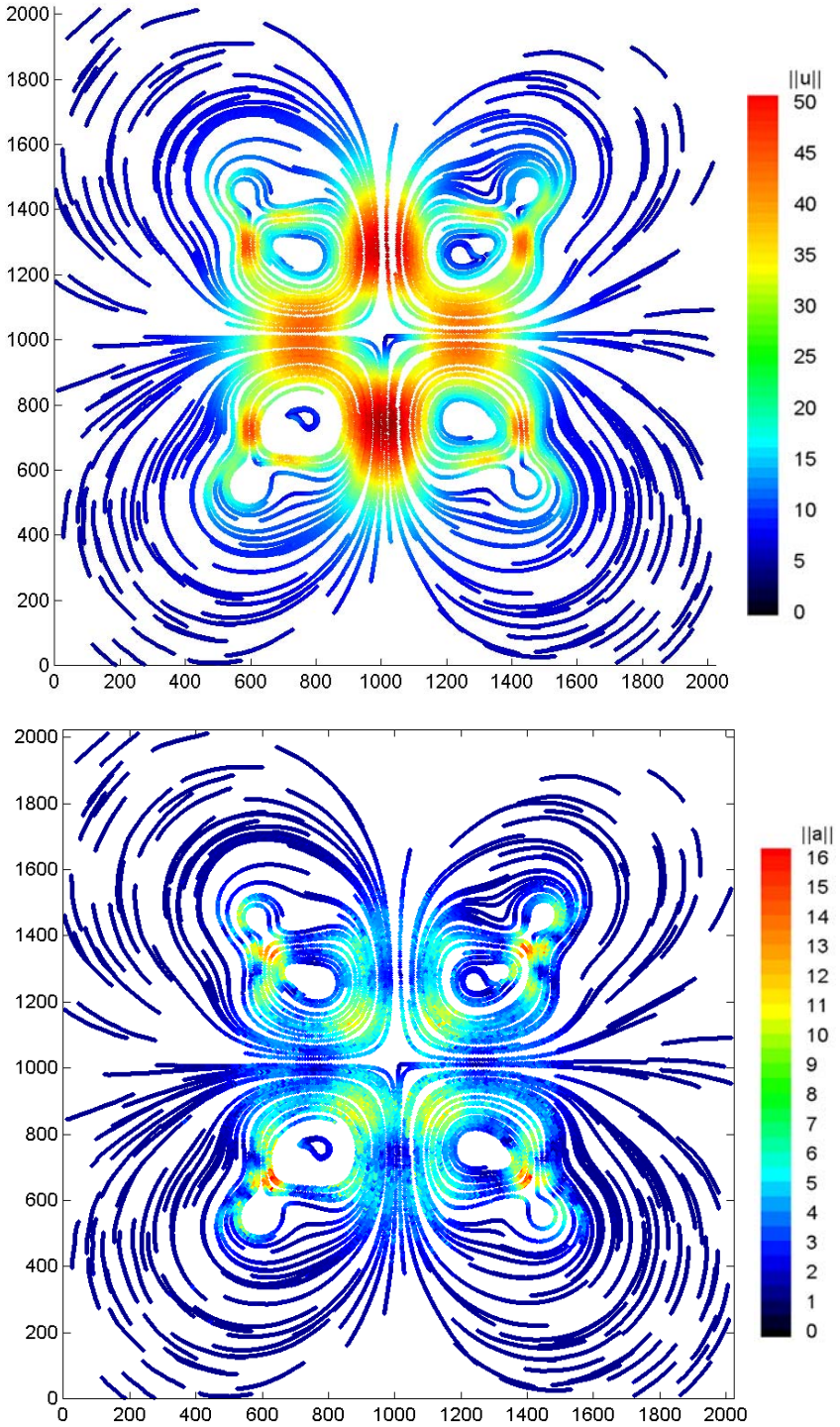

Figure 5.2 Example of instantaneous velocity (above) and acceleration (below) measured along trajectories over one run ($\|\vec{u}\|$ is in pixel/s, $\|\vec{a}\|$ is in pixel/s^2, 1 mm is about 2.02 pixels).

red mean high values, whilst the ones close to the dark blue mean low values.

Velocity shows a behaviour that is in agreement with previous measurements via PIV (Particle Image Velocimetry) obtained by Rossi et al. (2005): for instance, the highest velocities are found above the two big magnets, with a maximum velocity of 50 pixel/s (i.e., about 25 mm/s), equivalent to the one previously measured; moreover, the hyperbolic stagnation points of the large and medium scales begin to be defined as the dark blue zones of the flow surrounded by higher velocity values (see the centre of the picture and the hyperbolic point of the medium scale figure-of-eight).

The acceleration measures have a physical meaning, as the highest values of acceleration come from the point where both velocity and strain are high (from the definition of Lagrangian acceleration), whilst strong velocities and strong curvature alone do not produce high acceleration.

The compliance with previous measurements and the physical plausibility of these results gave some confidence and the first boost to the further development of PTVA.

4 PROBABILITY DENSITY FUNCTION OF VELOCITY AND ACCELERATION

In Figure 5.3, the probability density function (pdf) of the instantaneous velocity is normalized by the root mean square velocity u_{RMS} of the flow (15.378 pixel/s corresponding to 7.612 mm/s), assumed as the typical velocity of the flow: on the top, the intensity of velocity and on the bottom its two components. The shape of the velocity intensity pdf shows that the measurements cover a broad range of velocity intensities. The cut-off corresponding to around 3 times u_{RMS} suggests the bounded conditions for the velocity we have in this flow: the possible values of the velocity go from zero (over stagnation points) up to a maximum value, reached by the fluid elements when they pass over the big magnets. The maximum instantaneous velocity measured in the present case (I = 0.53 A) is about 26.26 mm/s, very close to the largest mean velocity found in the Eulerian field, about 24.95 mm/s (see also Figures from 5.5 to 5.7; the method to build the Eulerian grids from the Lagrangian data is briefly described in section 5). The peak of probability, around 0.2 u_{RMS} equivalent to 1.522 mm/s, comes mainly from the boundaries and corners of the investigation field, where particles do not stay still but slowly move to enter or exit the field. Also the signature of the multi-scale forcing can be found in the pdf.

Similar features can be spotted on the bottom of Figure 5.3, concerning the pdf of the two component of the velocity in the x and y-direction. It should be noticed that only the stagnation point have both zero x- and y-velocity whilst, more often, when one of the two velocity component is zero, the other is non-zero (look, for instance, at straight trajectories crossing the two big magnets, with high y-velocity and zero x-velocity).

The pdf of acceleration intensity, normalized with the root mean square acceleration a_{RMS} of the flow (6.304 pixel/s^2 corresponding to 3.121 mm/s^2), is plotted on the top of Figure 5.4. Also in this case we have a large tail but, differently from the velocity intensity, there is not a sharp cut-off. The largest instantaneous acceleration measured is about 21.22 mm/s^2, larger than the maximum mean acceleration found on the Eulerian

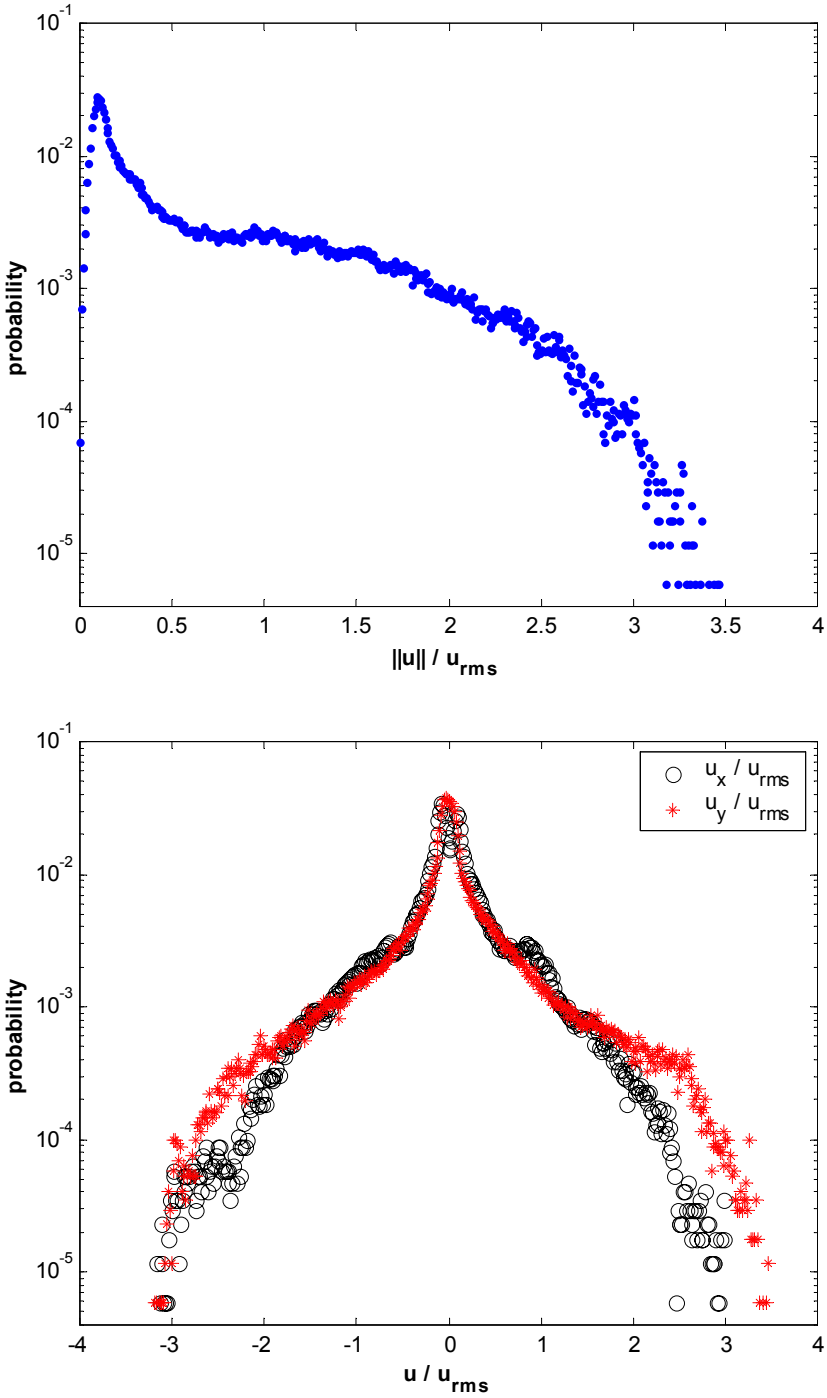

Figure 5.3 Probability density functions of the velocity: on the top, the velocity intensity, on the bottom, the velocity x component (black circles) and the y one (red asterisks); on both plots, velocity is normalized by $\vec{u}_{RMS}$ = 15.378 pixel/s corresponding to 7.612 mm/s.

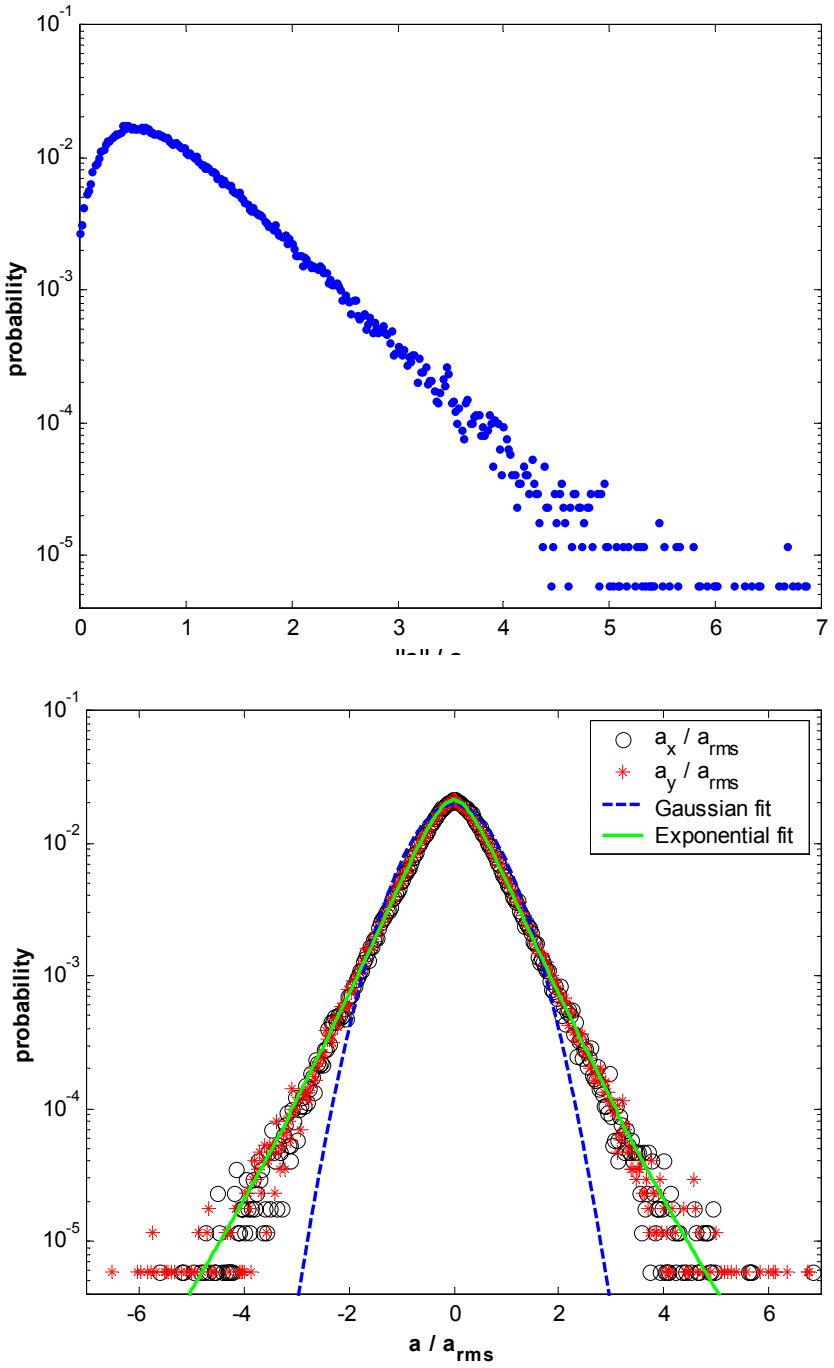

Figure 5.4 Probability density functions of the acceleration: on the top, the acceleration intensity, on the bottom, the acceleration x component (black circles) and the y one (red asterisks); the dashed blue line is the best-fit Gaussian curve, the solid green line is the best-fit curve of an empirical curve proposed by La Porta et al. (2001) and Voth et al (2002) to describe acceleration components on turbulent flows; on both plots, acceleration is normalized by $\vec{a}_{RMS}$ = 6.304 pixel/s^2 that is 3.1205 mm/s^2.

field, which is 8.23 mm/s^2 (compare with Figures from 5.5 to 5.7): this can be explained by the space averaging introduced on the measurement in the Eulerian measure but also by imperfections of the PTVA, whose percentage errors on acceleration are smaller than previous methods but still present.

Regarding the pdf of the acceleration x and y components, they are showed on the lower part of Figure 5.4: the x-component is plotted with black circles while the y component with red asterisks; the Gaussian curve that best-fit the data in a least mean square sense is drown with a dashed blue line; the solid green line is the best-fit curve of an empirical function proposed by La Porta et al. (2001) and Voth et al (2002) to describe acceleration components on turbulent flows (see below). Both these components are Gaussian for more than one decade of the probability density (and for absolute values of the acceleration components smaller than almost 2 $a_{RMS)}$, to then show broader tails, assuming the stretched exponential form displayed by the same components reported in Voth et al. (1998), La Porta et al. (2001) and Voth et al (2002). As the values that acceleration can assume in this flow are bounded by the experimental conditions, the values assumed by the acceleration components go from 0 to $\pm$ 6 $\vec{a}_{RMS}$, while in real turbulence they can go from 0 to more than 30 $\vec{a}_{RMS}$.

In particular, the cited Authors proposed, to parameterize the acceleration component pdf, the phenomenological function

$$P(a) = C\exp\left(-a^2 / \left[(1+|a\beta/\sigma|^{\gamma})\sigma^2\right]\right) \tag{5.1}$$

with the following values for the parameters: $\beta = 0.539$, $\gamma = 1.588$, $\sigma = 0.508$ and $C = 0.786$. The value of these parameters for the solid green line of Figure 5.4 turn out to be very similar to the one reported by the quoted Authors, with $\beta = 0.562$, $\gamma = 1.266$, $\sigma = 0.614$, except for the value of C, in this case equal to 0.0211. Such an exponential curve is considered one of the signature of turbulence, therefore it has been used to as a prove of the reliability of innovative measurement methods, like in Mordant et al., 2004 and in Oullette et al., 2006, or of numerical simulation via DNS (Biferale et al., 2005). Aringazin and Mazhitov (2003) also derived theoretically a distribution of this type.

The shape of the acceleration component pdf displayed by this multi-scale turbulent-like flow is so very similar to the one usually measured in real turbulence that arguing that this confirms some other turbulent-like properties of this flow becomes very tempting. Anyway, it is necessary to keep in mind that this flow is a laminar and quasi-steady one, so the question of which characteristics of turbulence generate which features spontaneously arises: the answer to this question (and additional quantifications of acceleration fields properties) is planned to be investigated in future researches.

5 EULERIAN FIELDS

The very good coverage of the investigation area, coming from large number of trajectories tracked for a long time, coupled with Eulerian repeatability of our experiments, made naturally arise the curiosity of seen if it is possible to extract a good quality Eulerian information from the Lagrangian measurements: whether this was feasible, it would have meant that doing two times the experiments, once with PIV to extract the Eulerian frame and once with PTVA to have the Lagrangian one, was no more necessary. As it will be shown soon, this result was possible on this flow, permitting not only to extract the velocity field but also the acceleration field. The accuracy on these two fields is so good to allow decomposing and analysing the components of Navier-Stokes equation,

$$\vec{a} = \frac{D\vec{u}}{Dt} = \frac{\partial \vec{u}}{\partial t} + (\vec{u} \cdot \nabla)\vec{u} = -\frac{\nabla P}{\rho} + \upsilon \nabla^2 \vec{u} + \vec{f} \tag{5.2}$$

(where P is the pressure ρ the fluid density, ν the fluid kinematic viscosity and $\vec{f}$ the forcing) as well as the divergence of the acceleration. Moreover, this was possible over the entire investigation field and with a resolution larger than the one obtained on the same flow via PIV. This high definition coming from the high number of positions (more than $2.6 \cdot 10^6$) of instantaneous velocity and acceleration, allows extracting grids of 600 x 600 points, with a mesh's size of 3 pixels and an extrapolation window's size that is, on average, of about 6.75 pixels. 600 x 600 grids lead to a resolution that is more than 4 times larger than the one obtained on the same flow with PIV (287 x 287 grid on the same investigation field).

The method used to construct the Eulerian grids adjusts the size of the extrapolation windows, depending on the number of samples available within the window; it is based on Smooth Particle Hydrodynamic approximations (Monaghan, 1992) when more than 18 samples are available within the extrapolation windows (in this case the extrapolation windows are significantly smaller than the size of small magnets), and on a biquadratic approximation (with feedback on the standard deviation and more than 24 positions within the extrapolation windows) when the extrapolation windows are of the order or larger than the size of the small magnets; the latter is a very rare case with more than $2.6 \cdot 10^6$ positions.

5.1 Eulerian fields of velocity and acceleration

The picture on the top of Figure 5.5 shows the large frame of the velocity field extracted from the PTVA data, the one on the top of Figure 5.6 is a zoom on the Southwest quarter of the large frame (to better highlight the medium scales), and the one on the top of Figure 5.7 represents a zoom on smallest scales of the Southwest quarter (to better focus on the small scales). As on all the subsequent figures, colours close to the red are associated to high values, colours close to the dark blue to low values; the colour bar on the right of each image allows a quantitative evaluation of the values of a particular quantity over the investigation field. On all the velocity fields, the grey lines cor

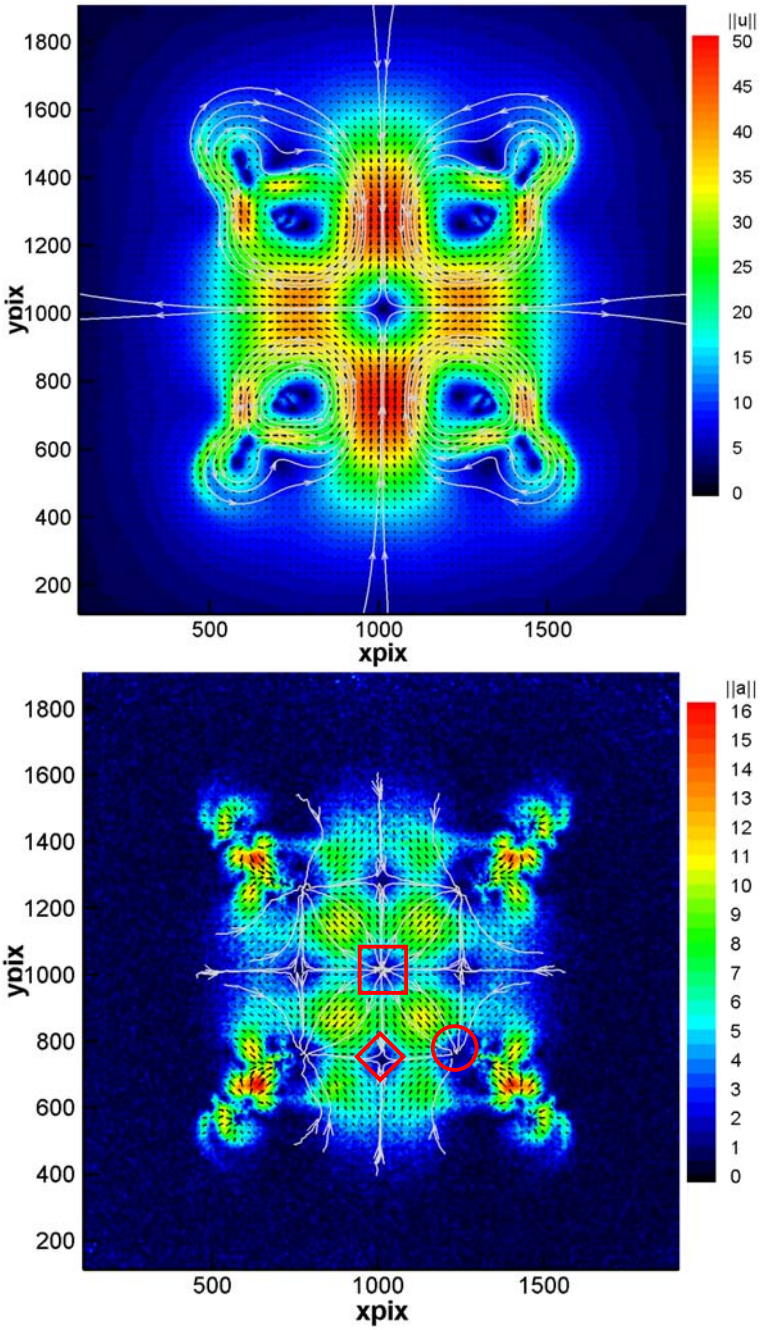

Figure 5.5 On the top, the large frame of the velocity field: the velocity intensity ||**u**|| is in pixel/s, lines correspond to streamlines. Below, the large frame of the acceleration field: the acceleration intensity ||**a**|| is in pixel/s^2, lines correspond to acceleration lines, i.e. lines that on every point are tangential to acceleration vectors. Circles are superimposed on elliptical stagnation point (on the velocity field) and on acceleration sinks, squares on hyperbolic stagnation points (on the velocity field) and on acceleration sources, and a rhombus on an acceleration spreader. 1 arrow for 64 is plotted, 1mm is about 2.02 pixels, the mesh is of 600x600 points with a mesh's size of 3 pixels.

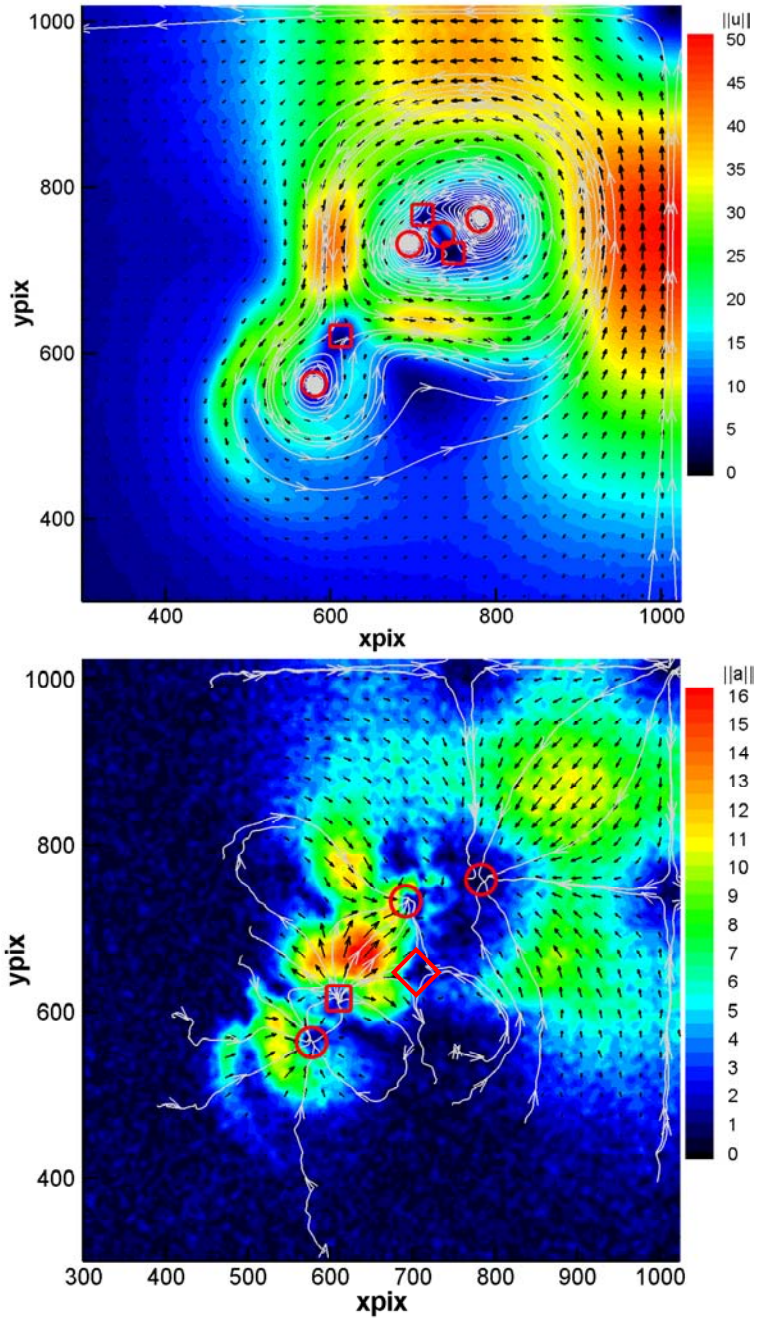

Figure 5.6 On the top, a zoom on the Southwest quarter of the velocity field: the velocity intensity ||**u**|| is in pixel/s, lines correspond to streamlines. Below, the same zoom on the acceleration field: the acceleration intensity ||**a**|| is in pixel/s^2, lines correspond to acceleration lines, i.e. lines that on every point are tangential to acceleration vectors. Circles are superimposed on elliptical stagnation point (on the velocity field) and on acceleration sinks, squares on hyperbolic stagnation points (on the velocity field) and on acceleration sources, and a rhombus on an acceleration spreader. 1 arrow for 64 are plotted, 1mm is about 2.02 pixels, the mesh's size of 3 pixels.

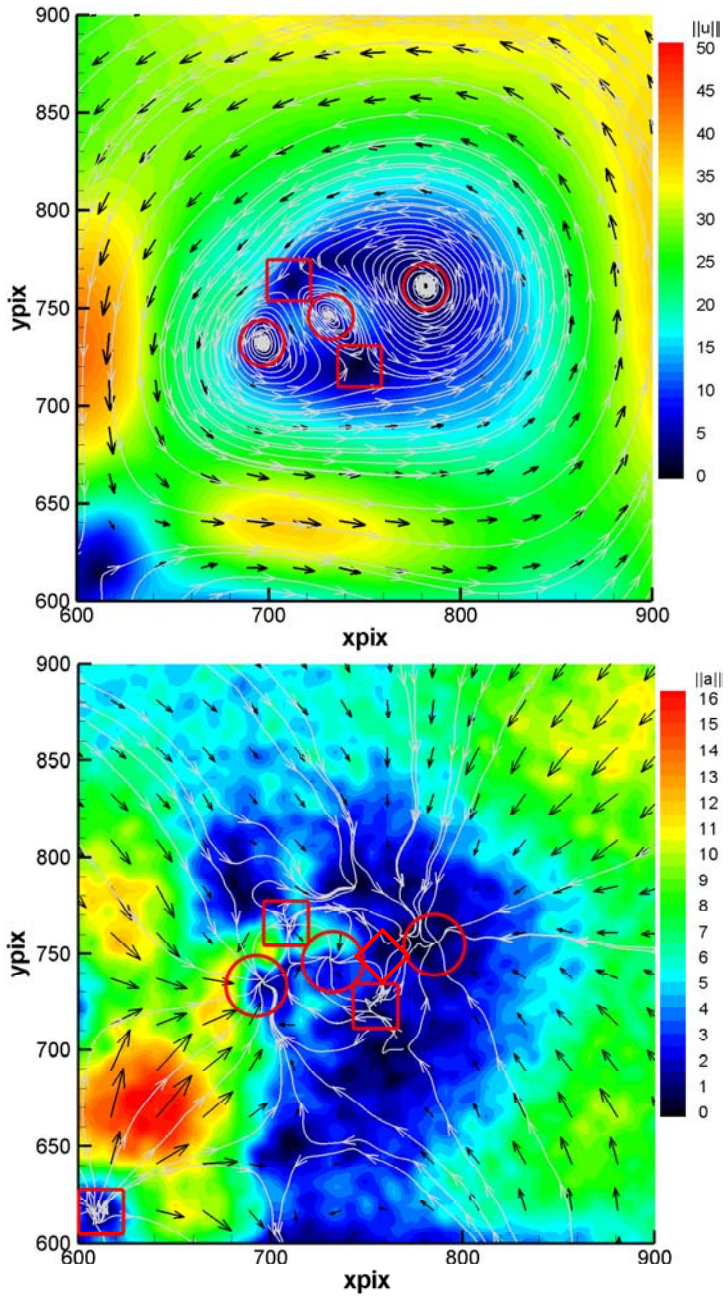

Figure 5.7 On the top, a zoom on smallest scales of the Southwest quarter of the velocity field: the velocity intensity ||**u**|| is in pixel/s, lines correspond to streamlines. Below, the same zoom on the acceleration field: the acceleration intensity ||**a**|| is in pixel/s^2, lines correspond to acceleration lines, i.e. lines that on every point are tangential to acceleration vectors. Circles are superimposed on elliptical stagnation point (on the velocity field) and on acceleration sinks, squares on hyperbolic stagnation points (on the velocity field) and on acceleration sources, and a rhombus on an acceleration spreader. 1 arrow for 64 are plotted, 1mm is about 2.02 pixels, the mesh's size of 3 pixels.

respond to streamlines, the black arrows to velocity vectors. The large frame illustrates the multi-scale flow generated by the electromagnetical forcing described in Figure 3.1, with the highest velocities found above the two biggest magnets and the hyperbolic stagnation point, connected to the large scales of the flow, clearly noticeable as the spot with zero velocity values in the centre of the field. This velocity field constructed from PTVA data is the same as the one obtained by Rossi et al. (2006a) (forcing I = 0.53 A) with Particle Image Velocimetry (PIV), except that, as already stated, the resolution is 4.3 here times higher than the one of PIV fields and the extrapolation window's size are typically 2.4 times smaller than PIV correlation window's size. The flow is well defined at all the scales, as shown by figures 5.6 and 5.7: on these figures, the red circles refer to elliptical stagnation points whilst the red squares refer to hyperbolic stagnation points. It is clear that stagnation points are very well defined at all the scales, with an impressively high definition of the elliptical stagnation points of the small scales. These pictures confirm that PTVA gives an extra quality on the measurements on this flow also if compared to PIV. The high definition reached on these measurements can be used also to automatically find the stagnation points on the flow: for example, Figure 5.8 shows how it is possible to obtain the map of the multiple-scale distribution of stagnation points simply by filtering out all the values higher than a certain threshold (2 pixel/s equivalent to about 0.99 mm/s in this case).

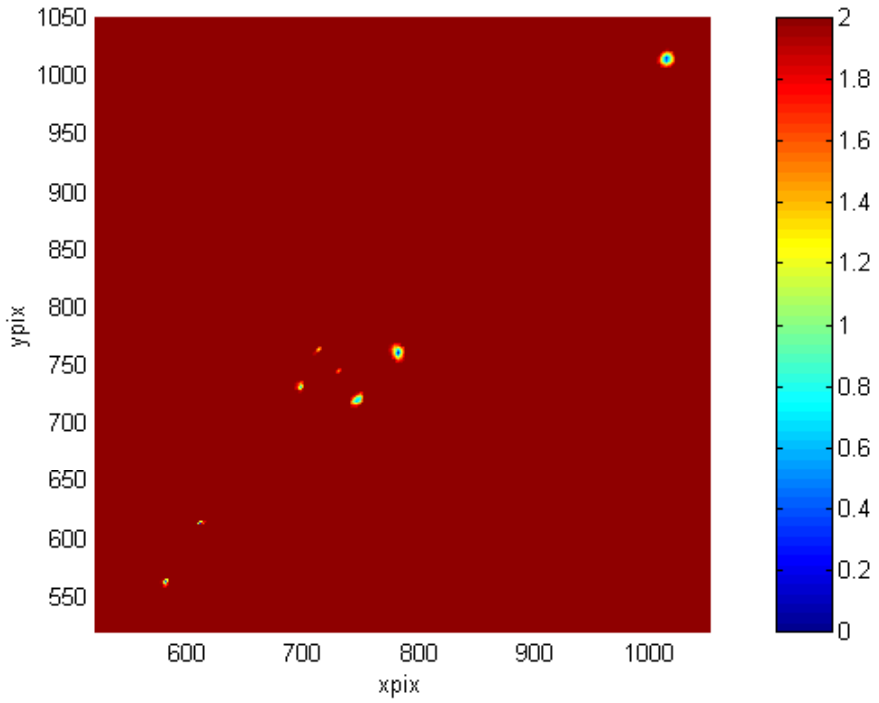

Figure 5.8 A zoom on the Southwest quarter of the velocity field, rescaled to only keep very low values of the velocity intensity ||**u**|| (in pixel/s) highlights the multi-scale distribution of of the stagnation points in this portion of the field.

Concerning the Eulerian acceleration field, its large frame is shown on the bottom of Figure 5.5, with a zoom on the Southwest quarter on the bottom of Figure 5.6 and a zoom on the small scales of this quarter on the bottom of Figure 5.7. On all these acceleration fields, the black arrows correspond to acceleration vectors and the grey lines to "acceleration lines". These "acceleration lines" are here defined as lines tangential on every point to the acceleration vectors: it was necessary to coin this new name as it was not find in literature a name to define this kind of lines. Regarding the spatial distribution of acceleration intensities, the highest acceleration values arise where both strain and velocity are high, as happens in the vicinity of the hyperbolic stagnation point of the medium scales, as it comes out from equation 1.1. This is confirmed by the fact that, at all the scales of the flow, both the local velocity maxima (for instance, above the two big magnets) and the local highest strain region (the hyperbolic stagnation points), instead of generate local acceleration maxima, create zones of zero acceleration. The distribution and the characteristics of these zero acceleration points are particularly interesting so, in the next section, they will be described.

5.2 Zero Acceleration Points

For a steady flow like the one studied here, the elliptical and hyperbolic stagnation points in the velocity field generates zero acceleration points: from a comparison between the velocity and the acceleration fields it is possible to confirm this fact but, also, to note that there are more zero acceleration points than stagnation points. In fact, the acceleration field shows some zero acceleration points which are not velocity stagnation points, for example above the two biggest magnets. This fact was numerically found by Goto and Vassilicos (2004), but not yet experimentally shown.

To allow a better visualization of the zero acceleration points and to make easier their analysis, on the lower part of figures 5.5, 5.6 and 5.7 some circles are superimposed on "acceleration sinks", squares on "acceleration sources" and rhombus on "acceleration spreader"; the reasons for these names will be explained soon.

A first analysis of the relations between velocity and acceleration fields clearly indicate that all the zero acceleration points come out from local velocity extrema, that is from stagnation point (local minima) or from local velocity maxima.

But a better way to classify the zero acceleration points is hinted by the acceleration lines, more precisely by their direction when they get close to the zero acceleration points. In practice, in the case of zero acceleration points arising from velocity stagnation points (local velocity minima), the acceleration lines going toward them have all the "same direction": if they go toward the zero acceleration points, they come from elliptical stagnation points; if they go away from the zero acceleration points, they arise from hyperbolic stagnation point; finally, if they are similar to the streamlines of a hyperbolic stagnation point (i.e., half of the acceleration lines go toward and half away from the zero acceleration point), they are not generated by s stagnation point but by a local velocity maximum. It should be noted that these three different kinds of zero acceleration points are present at all the scales of the flow. Drawing a parallel with potential flows, we can say that the zero acceleration points arising from hyperbolic stagnation points are sources of acceleration (so they will be called "acceleration sources"

from now on), the ones coming from elliptical stagnation points are sinks of acceleration (so they will be called “acceleration sinks” from now on) and the ones generated by local velocity maxima are spreader of acceleration (so they will be called “acceleration spreader” from now on). It should be noticed that this kind of analysis is allowed by the good definition of the acceleration lines at all the scales (see, for example, the sequence of acceleration sinks, spreader and sources at the small scales on the bottom of Figure 5.7), thing made possible by the high quality of PTVA method.

The Eulerian field of $\nabla \cdot \vec{a}$ (see Figure 5.12, whose better description can be found in section 5.5) allows to quantitatively classify the zero acceleration points, sustaining at the same time what just asserted: the acceleration sinks lead to local minima of $\nabla \cdot \vec{a}$, the acceleration sources lead to local maxima of $\nabla \cdot \vec{a}$ (so the zero acceleration point generated by stagnation points are local maxima of the absolute value of the acceleration divergence)**,** while the acceleration spreader correspond to local zeros of $\nabla \cdot \vec{a}$ (so to minima of the absolute values of the acceleration divergence). It should be noticed that this description of zero acceleration points is in agreement with the one suggested by Goto and Vassilicos (2004) that introduced the names of elliptic (vortical) zero-acceleration points and hyperbolic (straining) zero-acceleration points.

Now that the zero acceleration points have been classified, a deeper insight on their role in the flow can be attempted. In fact, the observation of the quoted figures reveals a multi-scale distribution of acceleration sources, sinks and spreaders similar to the multi-scale distribution of stagnation points, e.g. the one found by Rossi et al. 2006b. It should be noticed here that the acceleration lines emanating from sources (respectively sinks) can be directly connected to sinks (respectively sources) of different scales. This clearly works differently than streamlines, where elliptical stagnation points are not directly connected to hyperbolic stagnation points via streamlines. This information contained in the acceleration field is thus extremely complementary to the velocity field as it highlights which flow structure is connected to which ones and so design the "web of the flow". Such information is expected to be crucial for flow control applications.

5.3 Navier-Stokes equations’ viscous term

The computation of the Navier-Stokes equations’ viscous term, $\upsilon \nabla^2 \vec{u}$, implies a second order spatial derivative on the velocity values, so it is very sensible to the noise and the quality of measurements. Despite that, the velocity field measured via PTVA is good enough to allow the computation of the velocity Laplacian: the resulting viscous term field is given in Figure 5.9, with the large frame on the top and a zoom on the Southwest quarter below. A circle is superimposed on an elliptical stagnation point of the velocity field, a square on a hyperbolic stagnation point, and a triangle on a region of shear flow.

This Eulerian field is noisy but still physically coherent: this coherence can be illustrated, for instance, by the comparison with the velocity field. In general, where the velocity vectors and the viscous term vectors have opposite direction, the viscosity is subtracting energy from the flow and so pulling it, whilst where they have the same direction the viscosity is pushing the flow. As it is possible to note that the vectors of veloci-

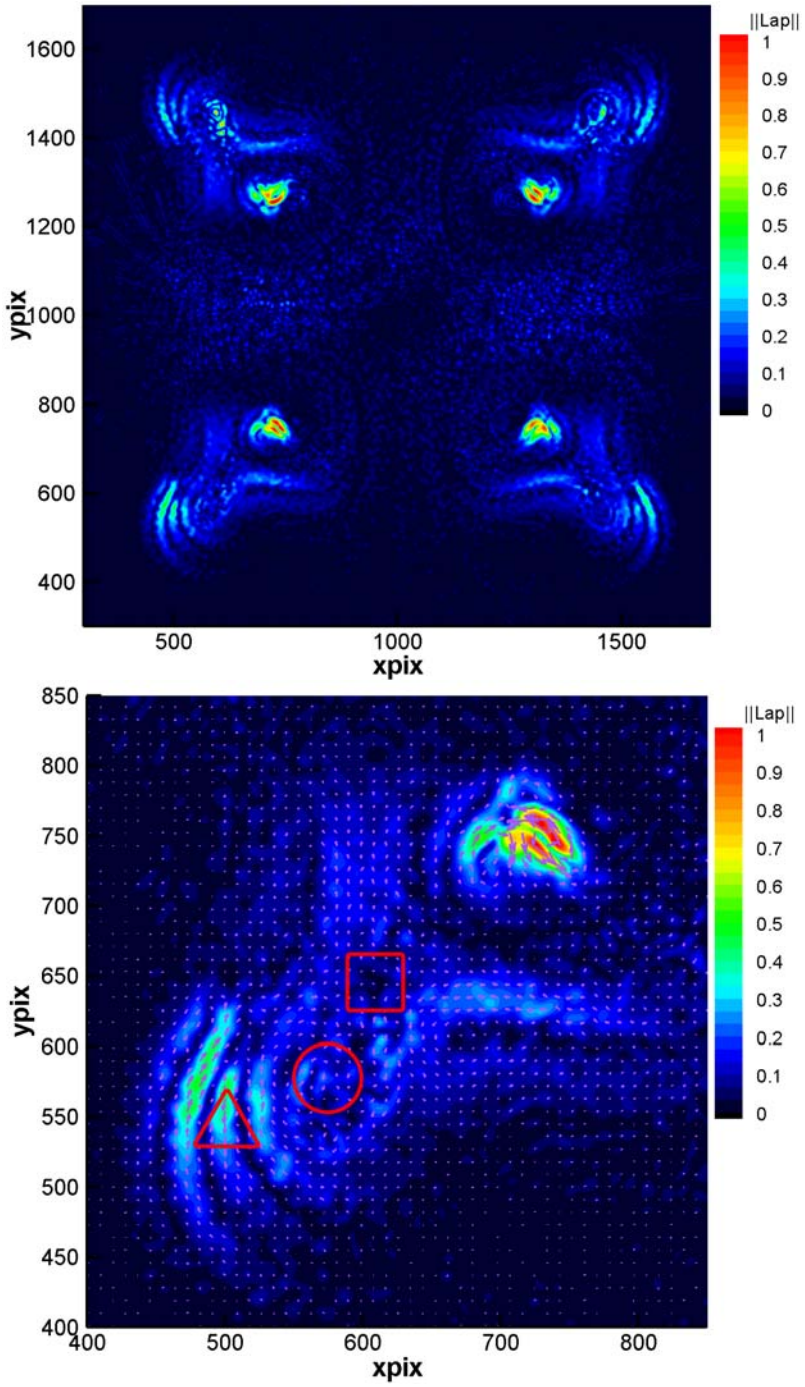

Figure 5.9 On the top, the large frame of the Navier-Stokes equations' viscous term field: the viscous term intensity $\|\nu\nabla^2\mathbf{u}\|$ is in pixel/s^2. Below, a zoom on the Southwest quarter of the same field. A circle is superimposed on an elliptical stagnation point of the velocity field, a square on a hyperbolic stagnation point, and a triangle on a region of shear flow. 1 arrow for 64 is plotted, 1mm is about 2.02 pixels, the mesh is of 600x600 points with a mesh's size of 3 pixels.

ty and viscous term around the elliptical stagnation point have opposite direction (the vectors of viscous term go clockwise while the velocity ones go anticlockwise), the viscosity is acting against the eddy to rotate. On the left of the triangle, a tongue of faster fluid is squeezing in a zone of slower fluid: so the viscosity is acting to slow it down (in fact velocity and viscous vectors have opposite direction); on the tongue over the triangle the viscous term is acting in the same direction as the velocity as this small scale low speed area bridges to higher speed areas of the flow.

Moreover, the root mean square of the viscous term (0.13 pixel/s^2) is almost 50 times smaller than the one of the acceleration (6.304 pixel/s^2): from the comparison of the acceleration field with the viscous term one it is clearly visible that the viscosity is of the same order of magnitude as the acceleration (and so relevant to the flow) almost only at the small scales (corresponding to the red zones of viscous term), as it happens in turbulent flows.

5.4 The pressure gradient

As the forcing is known and the electromagnetic forces are concentrated only above the magnets (see figure 3.11), which are also of weak percentage area (less than 2.6% of the investigation area), the pressure gradient field, which is difficult to measure experimentally, can be extracted from the difference between acceleration and viscous terms in Navier-Stokes equations. Moreover, as the viscous term is negligible over the vast majority of the flow, an estimation of the pressure values can be given through the analysis of the acceleration field using the equation

$$\vec{a} = -\frac{\nabla P}{\rho} \tag{5.3}$$

In practice, when acceleration lines all converge towards a node (acceleration sink) the pressure gradient is decreasing toward this point, which turns out to be a local minimum of pressure, which is physically coherent as the acceleration sinks are also the centres of eddies; on the contrary, acceleration lines all diverging from a node (acceleration source) correspond to an increasing pressure toward this point, which is so a local maximum of pressure: also in this case this assertion is physically correct, as the acceleration sources are generated by hyperbolic stagnation point, where two counter-jet generated by a couple of magnets meet, causing high pressure values. It should be noticed that, to date, on the Authors knowledge only once the pressure field was measured over the entire investigation field, by Liu and Katz, 2006, using a four-exposure PIV system.

5.5 Towards efficient mixing

Efficient mixing can be defined as the one achieved when a required mixing is

reached with the minimum power input or, vice versa, when the mixing is maximized given a certain power input. The chance to measure (and therefore to reach) an efficient mixing would be of major significance for many fields in industry and for a lot of engineering applications: in particular, a quasi-two-dimensional efficient mixer can be important for the glass and plastic sheet (Plexiglas, polythene, etc.) industry, where some chemical substances, added in many points of thin layers of fluid glass or plastic, have to be uniformly distributed over the entire layer. So, to clarify which one of the feasible configuration of a particular apparatus gives efficient mixing, a way to measure the power input into the flow and how this input generates mixing is needed.
As a way to analyse the power input/output and transformation for unit mass in the flow, the study of the scalar field of the scalar product $\vec{u} \cdot \vec{a}$ and of the pseudo-vectorial field of the vectorial product $\vec{u} \times \vec{a}$ has been chosen; as a way to measure where there is a strong stirring in the flow and so where fluid elements are more likely t separate, the study of the acceleration divergence $\nabla \cdot \vec{a}$ was selected. If, after the measurements of the acceleration and velocity showed just before, the extraction of the first two fields seemed not very difficult, the measure of $\nabla \cdot \vec{a}$, implying a spatial derivative on the acceleration (coming out from two temporal derivatives already) seemed challenging. Moreover, on the Author knowledge, an experimental measure of the acceleration divergence over the entire investigation field had been never achieved.
Starting with the analysis of the power input/output and transformation in the flow, Figure 5.10 gives the Eulerian fields of the scalar product $\vec{u} \cdot \vec{a}$**,** on the top, and of the vectorial product $\vec{u} \times \vec{a}$**,** on the bottom: the two fields are computed on PTVA data of velocity and acceleration before to construct their Eulerian fields, so without additional spatial averages. On the $\vec{u} \cdot \vec{a}$ field, red regions indicates a power input and blue regions a power output, on the $\vec{u} \times \vec{a}$ field, red regions indicates a transformation of the power input into forces that causes the flow to rotate anticlockwise and blue regions to rotate clockwise.
$\vec{u} \cdot \vec{a}$ (measured in pixel^2/s^3) is proportional, point by point, to the tangential acceleration so it shows where fluid particles increase their velocity (velocity and acceleration in the same direction) or decrease their velocity (acceleration and velocity in opposite directions) but, more significantly, it gives the power input and output in the flow per unit mass. As in this flow the main power input comes from the forcing above the magnets, it is coherent that $\vec{u} \cdot \vec{a}$ roughly identifies the magnets' positions (see figure 5.11, where a zoom on the inner part of the $\vec{u} \cdot \vec{a}$ field is shown together with some red dotted lines pinpointing the position of the big and medium magnets). In particular, taking in account that on the South big magnet the flow goes upward and on the North goes downward, the fluid elements receives the most part of the power when they meet the big magnets, while the large scale hyperbolic stagnation point makes feel its presence from the second half of the magnets, subtracting power from the flow to make it decelerate. A similar behaviour can be observed above the medium scales magnets. Anyway, the presence in the field of regions of local maxima and minima of $\vec{u} \cdot \vec{a}$ indicates that this field also illustrates the power input/output related to the work of pressure terms: see, for example, the alternated values encountered following the line ypix $\cong$ 1000, caused by the presence of the large scale hyperbolic stagnation point. This Eulerian field per-

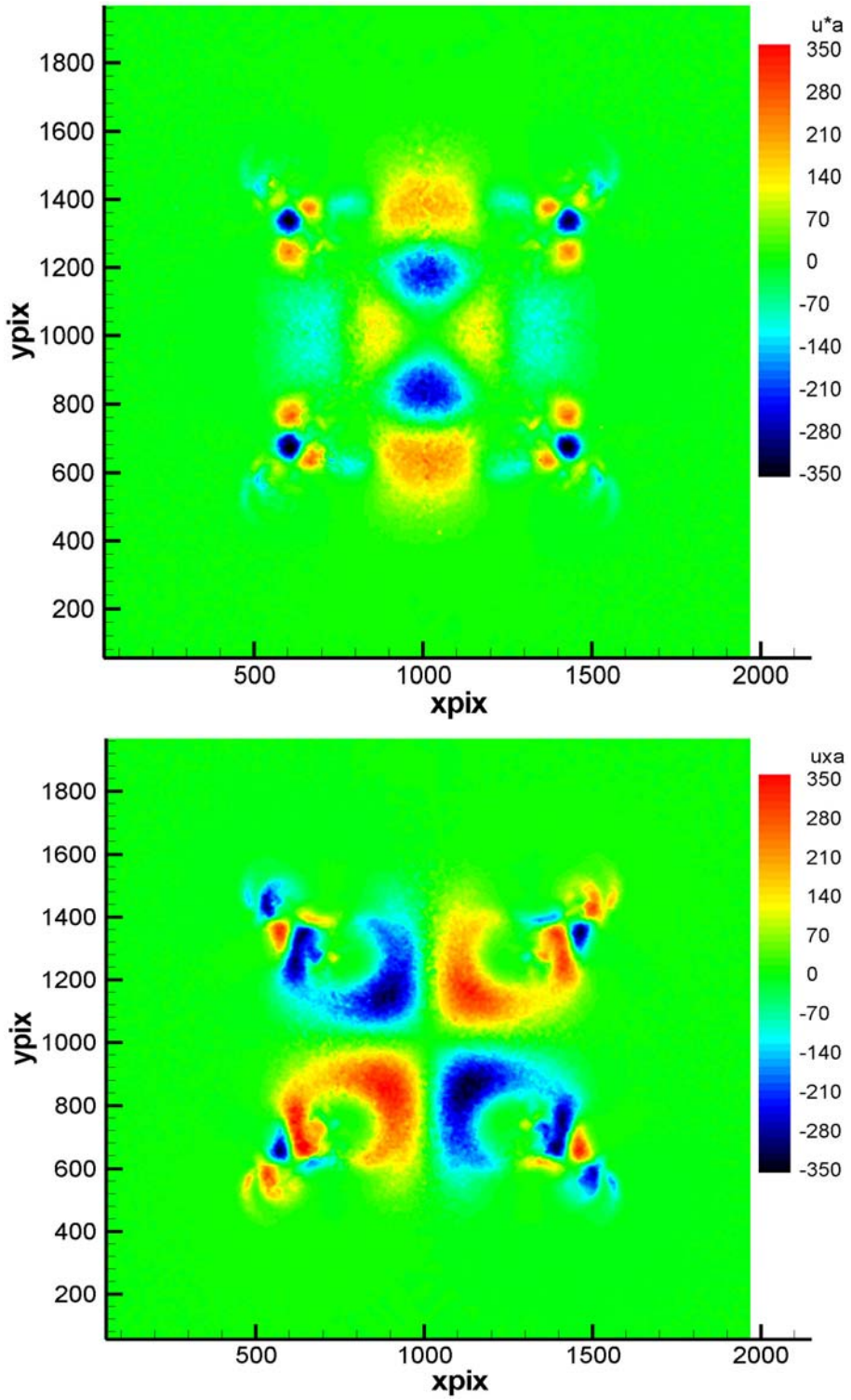

Figure 5.10: On the top, the field of the scalar product $\vec{u} \cdot \vec{a}$ **,** in pixel^2/s^3. Below, the field of the intensity of the vectorial product $||\vec{u} \times \vec{a}||$**,** in pixel^2/s^3. 1mm is about 2.02 pixels, the mesh is of 600x600 points with a mesh's size of 3 pixels.

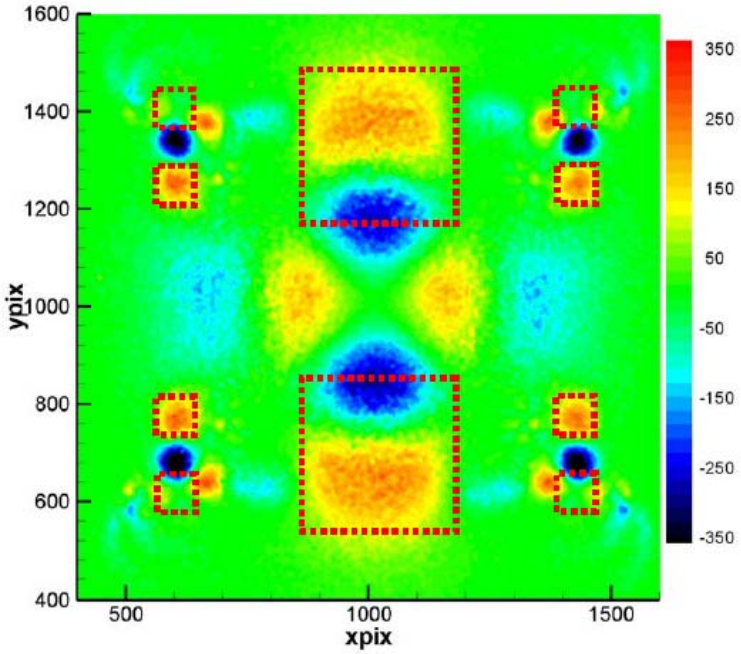

Figure 5.11: A zoom on the inner part of the field of the scalar product $\vec{u} \cdot \vec{a}$**,** in pixel^2/s^3, with the superposition of the position of big and medium magnets (red dotted lines). 1mm is about 2.02 pixels.

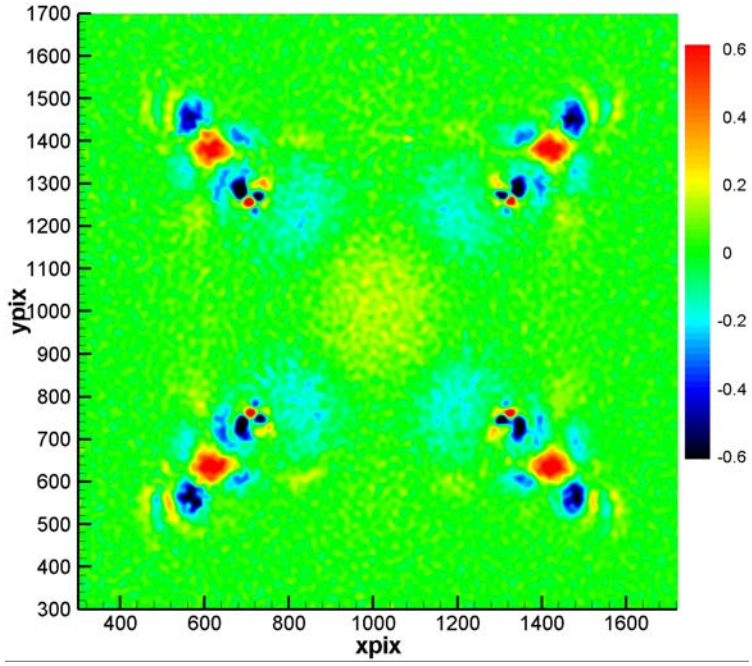

Figure 5.12: the field of $\nabla \cdot \vec{a}$, in s^{-2}; the color map does not use the full scale, that goes from about –1 s^{-2} to 1 s^{-2}, to keep visible the values above the large scale hyperbolic stagnation point. 1mm is about 2.02 pixels.

mits a deeper insight in the pressure distribution according to the flow topology and to its fractal forcing.

The vectorial product $\vec{u} \times \vec{a}$ (measured in pixel^2/s^3) is linked to transformation of the power input into forces that causes the flow to rotate that so allow the formation of eddies in it. This because it is proportional to the transversal component of the acceleration: for instance, the tilting of the shear flow already highlighted on the top of Figure 5.7 generates in a zone of the flow where the tangential acceleration is small compared to the transversal one.

The two products $\vec{u} \cdot \vec{a}$ and $\vec{u} \times \vec{a}$ can so be useful to characterize the power input/output and transformation, as well as the pressure distribution, of the flow in relation to its topology.

Once the tools to characterize the power input in the flow have been illustrated, it is time to try to identify a tool to measure the intensity of the stirring in the flow. In Figure 5.12, the Eulerian field of $\nabla \cdot \vec{a}$ (measured in s^{-2}) is shown; to keep visible the values of the divergence above the large scale hyperbolic stagnation point, the colour map does not use the full scale, that goes from about –1 s^{-2} to +1 s^{-2}, but only a fraction of it, in the range ±0.6 s^{-2}. High values of the acceleration divergence (and so of strong stirring) are indicated by the red, low values by the blue. So this Eulerian field of the acceleration divergence permits to identify and characterize the regions of the flow where stirring is high as the regions of local maxima of the field. In fact, the fluid particle acceleration is given by the Lagrangian derivative

$$\frac{D\vec{u}}{Dt} = \vec{a} \tag{5.4}$$

On the other hand, the topology of the velocity field is largely determined by the incompressibility of the velocity field that, applied to (5.4) gives

$$\nabla \cdot \vec{a} = \vec{s}^{\,2} - \frac{\vec{\omega}^2}{2} \tag{5.5}$$

where $\vec{s}$ is the strain matrix and $\vec{\omega}$ the vorticity vector. From equation 5.4 it is possible to see that, on one hand, $\nabla \cdot \vec{a}$ has the local maxima most often around hyperbolic stagnation points where $\vec{s}^{\,2}$ is large whilst $\vec{\omega}^2$ is close to zero, on the other hand $\nabla \cdot \vec{a}$ has the local minima most often around elliptical stagnation points, where then opposite happens ($\vec{s}^{\,2}$ is close to zero whilst $\vec{\omega}^2$ is large). So, fluid elements pairs can separate significantly where their acceleration divergence is large and positive that, whether the streamline structure is persistent enough in time, happens most often in the vicinity of hyperbolic stagnation points, as shown by Vassilicos (2002). From a comparison between the Eulerian field of the acceleration divergence (Figure 5.12) and the one of the acceleration (Figure 5.5), it is possible to experimentally show what previously asserted: as in this flow the streamline structure and so the stagnation points are persistent (quasi-steady flow), the local maxima of $\nabla \cdot \vec{a}$ corresponds to the acceleration sources coming

out from hyperbolic stagnation points, whilst the local minima of $\nabla \cdot \vec{a}$ corresponds to the acceleration sinks coming out from elliptical stagnation points. So, even if the Eulerian field of the acceleration divergence is still noisy (because each derivative amplify the noise present in the trajectory measure) it turns out to be physically coherent and, to the Authors knowledge, Figure 5.12 can be considered the first experimental measure of the acceleration divergence.

It should be noticed that the acceleration sources causing the higher stirring are not the one connected to the large scales and so to the largest power input: in fact, the divergence of the large scale acceleration source is around three times smaller than the divergence of the medium scale acceleration source and of one of the small scale acceleration source. So it is not always true that to have the higher stirring (that increase mixing) it is needed to put as much power as possible into the flow but, following a multi-scale approach, it should be better to inject a smaller amount of power into the right scales, the ones that cause strongest stirring in relation to the multi-scale flow structure. Anyway, the decrease of the acceleration source's influence area going from large to small scales should be notice too: this aspect need to be more deeply investigated in the future. It should also be notice that some regions of high acceleration divergence arise from regions of strong shear flow, as visible in the tongue of faster fluid squeezing in a zone of slower fluid already described in section 5.3.

Also if the Eulerian maps presented in this section cannot be considered as the ultimate tool to reach the efficient mixing, they permit to characterize the power input in the flow and how this generate stirring in it, so the combination of these Eulerian fields can be seen as a first set of tools useful to make a first step toward efficient mixing.

6. CONCLUSIONS

In order to obtain accurate Lagrangian measurements of the acceleration in fluids, a novel method (PTVA, Particle Tracking Velocimetry and Accelerometry), amenable to extract acceleration from particle tracking, has been presented and validated: this method is self adaptive according to the local flow properties. It has been shown that PTVA allows increasing the quality of the acceleration measurement compared to previous methods based on particle tracking: in particular, PTVA allows a reduction of the percentage measure errors of about six times for the velocity and of about four times for the acceleration. Moreover, PTVA has also shown to be robust to convection and to flow structures time dependency. As it does not involve any complex experimental set-up, PTVA can be an useful tool for future measurements in the field of turbulent and turbulent-like flows and for other people working in these fields. In addiction, as it takes as an input the particle positions extracted from PTV, it can be used to improve the quality of previous PTV measurements.

This PTVA method has been applied to a quasi-two-dimensional electromagnetically-controlled multi-scale turbulent-like flow. The extra quality provided by the method has permitted to have a deeper insight in the physics of the flow object of this study and to experimentally measure, for the first time on the Author's knowledge, the divergence of the acceleration over all the investigation field with a high spatial definition.

Taking advantage of the Eulerian repeatability of these measurements (performed on multiple-scale laminar flows), PTVA has allowed to extract the Eulerian fields of $\vec{u}$ and $\vec{a}$ from the Lagrangian information, and so to study their multiple-scale distribution according to the flow topology and to its fractal forcing.

Moreover, the fact that there are more zero acceleration points than zero velocity points, already numerically found by Goto and Vassilicos (2004), has been measured experimentally, for the first time in the Author's knowledge. Three different kinds of these zero acceleration points has been detected, classified and an attempt to explain their role for the flow behaviour has been given: this classification is in agreement with the one numerically found by the Authors quoted in the previous sentence. The zero acceleration points appear to be as a multi-scale distribution of "sources", "sinks" and "spreader" of acceleration and which are related to local maxima and minima of pressure. The acceleration sources are local maxima of $\nabla \cdot \vec{a}$ and so region with the highest stirring in the flow field, the acceleration sinks are local minima of $\nabla \cdot \vec{a}$ and the acceleration spreaders local zeros of $\nabla \cdot \vec{a}$**.** Moreover, the acceleration sources and sinks are connected via "acceleration lines" (i.e., lines parallel in every point to the acceleration vectors), defining a "web structure" of the flow able to give information on it that are complementary to the one of the velocity field.

The computations of the whole Eulerian field of the viscous term of the Navier-Stokes equations, $\upsilon \nabla^2 \vec{u}$, has permitted to complete the measurement of the Navier-Stokes equations' terms, so allowing an indirect measurement of the pressure gradient all over the investigation area.

To clarify which one of the feasible configuration of a particular apparatus gives ef-

ficient mixing (which can be defined as the one achieved when a required mixing is reached with the minimum power input or, vice versa, when the mixing is maximized given a certain power input), the measure of the power input into the flow and of how this input generates stirring and mixing is needed. As a way to analyse the power input/output and transformation for unit mass in the flow, the study of the scalar field of the scalar product $\vec{u} \cdot \vec{a}$ and of the pseudo-vectorial field of the vectorial product $\vec{u} \times \vec{a}$ has been proposed; as a way to measure where there is a strong stirring in the flow, the study of the acceleration divergence $\nabla \cdot \vec{a}$ was selected following Vassilicos (2002). In particular, the experimental measure of $\nabla \cdot \vec{a}$, implying a spatial derivative on the acceleration (already coming out from two temporal derivatives on the trajectory) was challenging and, on the Author knowledge, never experimentally achieved over the entire investigation field before. Anyway, the high rate of noise removal from the trajectories allowed by PTVA, has permitted to extract it, allowing to reach a deeper insight to the multi-scale distribution of the intensity of stirring in the flow. This permits to make a further step toward efficient mixing, also because a multi-scale approach could lead to a definition of the way to inject power into the right scales, the ones that cause most of the stirring, in relation to the multi-scale flow structure.

The probability density function of the Lagrangian acceleration has been studied too: in particular, the pdf of the acceleration components displayed by this multi-scale turbulent-like flow has turned out to be very similar to the one usually measured in real turbulence. This makes very tempting to argue that this confirms some other turbulent-like properties of this flow. Anyway, it is necessary to keep in mind that this flow is a laminar and quasi-steady one, so the question of which characteristics of turbulence generate which features spontaneously arises: the answer to this question, along with some additional quantifications of the acceleration properties linked to the flow topology, will be investigated in future researches.

ACKNOWLEDGEMENTS

Even if the acknowledgements of a PhD manuscript should begin with thanks to the supervisors, I would like to thank, first of all, my friend and master Lionel Rossi, for his patience and for all the time we spent together working in the lab, discussing of science, drinking pints…

Thanks to my two supervisors, Giorgio Querzoli and John Christos Vassilicos, for having backed and endured me.

Thanks to all the European Community's Marie Curie Training Site on Environmental Turbulence, for giving me two times the bursary to spend six month at Imperial College London.

Thanks to all the friends in ICL, particularly to Ala, Erwan, Frederic and Richard, for everything we did together and to William and Prangchira for all the help before and during experiments.

Thanks to everybody in the Turbulence and Mixing Group of the Department of Aeronautics.

Thanks to everybody in the Department of Aeronautics' staff, particularly to Molly and Sabine.

Thanks to everybody in the Dipartimento di Ingegneria del Territorio, particularly to Mari and Antonio for all the coffees drunk together.

Thanks to all my friends, particularly to Massimo Salvatore Giovanni, he knows why.

A big thank to Giancarlo, Elia and Gina, for too many things to stay in just thousands pages.

Last but undoubtedly not least, my biggest thank goes to my turtle Gnappetta: occi cocci ciccoi.

1st February 2007 Simone

8. REFERENCES

Adrian R.J., *Particle-imaging techniques for experimental fluid mechanics*, Annual Review of Fluid Mechanics, 261-303, 1991.

Antonia R. A., Chambers A. J., Britz D. and Browne L. W. B., *Organized structures in a turbulent plane jet – topology and contribution to momentum and heat transport*, Journal of Fluid Mechanics, 172, 211-229, 1986.

Aringazin A.K. and Mazhitov M.I., *The PDF of fluid particle acceleration in turbulent flow with underlying normal distribution of velocity fluctuactions,* Physical Letters A, 313, 2003.

Auton T.R., Hunt J.C.R. and Prud'homme M., *The force exerted on a body in inviscid unsteady non-uniform rotational flow*, Journal of Fluid Mechanics, 197, 241-257, 1988.

Belmonte A., Martin B. and Goldburg W. I., *Experimental study of a Taylor's hypothesis in a turbulent soap film*, Phisics of Fluids, 12, 1999.

Bergthorson J. M. and Dimotakis P. E., *Particle velocimetry in high-gradient/high-curvature flows,* Experiments in Fluids, 41 (2), 255-263, 2006.

Biferale L., Boffeta G., Celani A., Lanotte A and Toschi F., *Lagrangian statistics in fully developed turbulence*, arXiv:nlin.CD/0402032, 1-4, 2005.

Boffetta G. and Celani A., *Pair dispersion in turbulence*, Physica A, 280, 1-9, 2000.

Boffetta G., Celani A. and Vergassola M., *Inverse energy cascade in two-dimensional turbulence: deviation from Gaussian behaviour*, Physical Review E, 61 (1), R29-R32, 2000.

Boffetta G., Lacorata G., Redaelli G. and Vulpiani A., *Detecting barriers to transport: a review of different techniques*, Physica D, 159, 58-70, 2001.

Bracco A., von Haedenberg J., Provenzale A., Weiss J. B. and Mc Williams J. C., *Dispersion and mixing in Quasigeostrophic turbulence*, Physical Review Letters, 92 (8), 084501, 2004.

Cardoso O., Marteau D. and Tabeling P., *Quantitative experimental study of the free decay of quasi-two-dimensional turbulence*, Physical Reviews E, 49, 1994.

Cenedese A. and Querzoli G., *A laboratory model of turbulent convection in the atmospheric boundary layer*, Atmos. Environ, 28, 1901-1913, 1994.

Cenedese A. and Querzoli G., *Lagrangian statistics and transilient matrix measurements by PTV in a convective boundary layer*, Measurement in Science and Technology, 8, 1553-1561, 1997.

Cenedese A. and Querzoli G., *Particle tracking Velocimetry: measuring in the Lagrangian reference frame,* in *Particle image velocimetry and associated techniques*, M.L. Riethmuller (editor), von Karman Institute for Fluid Dynamics, 2000.

Cenedese A., Espa S. and Miozzi M., *Experimental study of two-dimensional turbulence using Feature Tracking,* Proceedings of the 12th International Symposium on Application of Laser Techniques to Fluid Mechanics, Lisbon (Portugal), 2004.

Chen. L., Goto S. and Vassilicos J.C., *Turbulent clustering of stagnation points and inertial particles*, Journal of Fluid Mechanics, 55, 143-154, 2006.

Christensen K.T. and Adrian, R.J., *Measurement of instantaneous Eulerian acceleration fields by particle image accelerometry: method and accuracy*, Experiments in Fluids, 33, 759-769, 2002.

Clercx H. J. H., van Hejist G. J. F. and Zoeteweij M. L., *Quasi-two-dimensional mturbulence in shallow fluid layers: the role of bottom friction and fluid layer depth*, Physical Review E, 67, 066303, 2003.

Couder Y., Chomaz J. and Rabaud M., *On the hydrodynamics of soap films*, Physica D, 37, 1989.

Dalziel S.B., *Decay of rotating turbulence: some particle tracking experiments*, Applied Scientific Research, 49, 217-244, 1992.

Davidson P.A., *Turbulence: an introduction for scientists and engineers*, 1-656, Oxford University Press, 2004.

Davila J. and Vassilicos J.C., *Richardson pair diffusion and the stagnation point structure of turbulence*, Physical Review Letters., 91(14), 144501, 2003.

Dong P., Hsu T.Y., Atsavapranee P. and Wei T., *Digital particle image accelerometry*, Experiments in Fluids, 30 (6), 626-632, 2001.

Falkovich G., Gawedzki K. and Vergassola M, *Particles and fields in fluid turbulence*, Rev. Mod. Phys. 73, 913, 2001.

Ferrari S. and Rossi L., *Velocity and acceleration measurements on an electromagnetically controlled multi-scale quasi-two-dimensional flow*", Proceedings of the XXX Convegno di Idraulica e Costruzioni Idrauliche - IDRA 2006, Rome, 2006a.

Ferrari S. and Rossi L., *Lagrangian velocity and acceleration measurements, PTVA, in quasi-two-dimensional electromagnetically controlled multi-scale flows*, Proceedings of the 13th International Symposium on Applications of Laser Techniques to Fluid Mechanics, Lisbon (Portugal), 2006b.

Ferrari S. and Rossi L., *Measurements of velocity and acceleration via PTVA (particle tracking Velocimetry and Accelerometry) and its application to electromagnetically controlled quasi-two-dimensionale multi-scale* flows, Experiments in Fluids, submitted, 2006c.

Fung J. C. H. and Vassilicos J. C., *Two-particle dispersion in turbulentlike flows*, Physical Review E, 57, 1998.

Goldstein M. E. and Hultgren L. S., *Boundary-Layer Receptivity to Long-Wave Free-Stream Disturbances*, Annual Review of Fluid Mechanics, 21, 137-166, 1989.

Goto S. and Vassilicos J. C., *Particle pair diffusion and persistent streamline topology in two-dimensional turbulence,* New Journal of Physics, 6, 65, 2004.

Goto S., Osborne D.R., Vassilicos J.C. and Haigh J.D., *Acceleration statistic as measures of statistical persistence of streamlines in isotropic turbulence*, Physical Review E, 71, 015301(R), 2005.

Hansen A. E. and Tabeling P., *Coherent structures in two-dimensional decaying turbulence*, Nonlinearity, 13, C1-C3, 2000.

Hascoët E., Rossi L. and Vassilicos ‚J.C., *Turbulent-like flows sustained and controlled by multi-scale electromagnetic forces*, Journal of Fluid Mechanics, submitted (2006a).

Hinsch K.D., *Holographic particle image velocimetry*, Measurement Science and Technology, 13, R61-R72, 2002.

Hishida K., Fujiwara A., Nagaya S., Kakugawa A. and Kodama Y., *Measurements of turbulent micro-structure in bubbly flows using combined PIV/LIF/IST tecnique*, Proceedings of the 2nd Symposium on Smart Control of Turbulence, Tokyo (Japan), 69-78, 2001.

Hopfinger E., Griffiths R. W. and Mory M., *The structure of the turbulence in homogeneous and stratified rotating fluids*, Journal of Mech. Theor. Appl., 21, 1983.

Jullien M.-C., Paret J. and Tabeling P., *Richardson pair diffusion in two-dimensional turbulence*, Physical Review Letters, 82, 1999.

Jullien M.-C., *Dispersion of passive tracers in the direct enstrophy cascade: experimental observations*, Physics of Fluids, 15(8), 2228-2237, 2003.

Kraichnan R. H., *Inertial Ranges in Two-Dimensional Turbulence*, Physics of Fluids, 10, 1417, 1967.

La Porta A., Voth G. A., Crawford A. M., Alexander J. and Bodenschatz E., *Fluid particle accelerations in fully developed turbulence*, Nature, 409, 1017-1019, 2001.

Legras B., Paireau O. and Tabeling P., *Vortex submitted to a shear: an experimental study*, Phys. Rev., 351, 1998.

Liu X. and Katz J., *Instantaneous pressure and material acceleration measurements using a four-exposure PIV system*, Experiments in Fluids, 41, 227-240, 2006.

Lowe K.T. and Simpson R.L., *Measurements of velocity acceleration statistics in turbulent boundary layers*, Proceedings of the Fourth International Symposium on Turbulence and Shear Flow Phenomena (TSFP-4), Williamsburg, Virginia (USA), 1043-1048, 2005.

Lucas B.D. and Kanade T., *An Iterative Image Registration Technique with an Application to Stereo Vision,* Proceedings of Imaging Understanding Workshop, Washington, D.C. (USA), 121-130, 1981.

Luthi B., Tsinober A. and Kinselbach W., *Lagrangian measurement of vorticity dynamics in turbulent flows,* Journal of Fluid Mechanics, 529, 87-118, 2005.

Marteau D., Cardoso O. and Tabeling P., *Equilibrium state of two-dimensional turbulence: an experimental study*, Physical Review E, 51, 1995.

Maxey M.R. and Riley J.J., *Equation of motion for a small rigid sphere in a non uniform flow*, Physics of Fluids, 26(4), 883-889, 1982.

Mc Williams J. C., *The emergence of isolated coherent vortices in turbulent flows*, Jounal of Fluid Mechanics, 146, 1984.

Melling A., *Tracer particles and seeding for particle image velocimetry*, Measurement Science and Technology, 8, 1406-1416, 1997.

Merzkirch W. Mrosewski T. and Wintrich H., *Digital particle image velocimetry applied to a natural convective flow*, Acta Mechanica, 4, 314-327, 1994.

Miller J., Weichman P. B. and Cross M. c., *Statistical mechanics, Euler's equation and Jupiter's Red Spot*, Physical review A, 45 (4), 2328-2359, 1992.

Moffat H. K., *The topology of scalar fields in2D and 3D turbulence*, T. Kambe et al. (eds), *IUTAM Symposium on Geometry and Statistics of Turbulence*, 13-22, Kluwer Academic Publishers, 2001.

Monaghan J.J., *Smoothed particle hydrodynamics*, Annual Review of Astronomy and Astrophysics, 30, 543-574, 1992.

Mordant N., Crawford A.M. and Bodenschatz E., *Experimental Lagrangian acceleration probability density function measurement*, Phisica D, 193, 245-251, 2004.

Mordant N., Pinton J.-F. and Michel O., *Time-resolved tracking of a sound scatterer in a complex flow: nonstationary signal analysis and applications,* Journal of the Acoustic Society of America, 112(1), 108-118, 2002.

Nadeem A. M. and Dracos, T., *Lagrangian PTV in 3D flows,* Applied Scientific Research, 51, 161-166, 1993.

Nagaya S., Kakugawa A., Kodama Y. and Hishida K., *PIV/LIF measurements on 2-D turbulence channel flow with microbubbles,* Proceedings of the 4th International Symposium on Particle Image Velocimetry, Goettingen (Germany), 2001.

O'Hern T.J., *An experimental investigation of turbulent shear flow cavitation,* Journal of Fluid Mechanics, 215, 365-391, 1990.

Ooi K.K. and Acosta A.J., *The utilization of specially tailored air bubbles as static pressure sensor in a jet,* Journal of Fluid Engineering, 106, 459-465, 1983.

Osborne D. R., Vassilicos J. C. and Haig J. D., *One-particle two-time diffusion in three-dimensional homogeneous isotropic turbulence,* Physics of Fluids, 17, 035104, 2005.

Ott S. and Mann J., *An experimental investigation of the relative diffusion of particle pairs in three-dimensional turbulent flow*, Journal of Fluid Mechanics, 422, 207-223, 2000.

Ottino J.M., *The kinematics of mixing: stretching, chaos, and transport*, 1-364, Cambridge University Press, 1989.

Oullette N.T., Xu H. and Bodenschatz E., *A quantitative study of three-dimensional Lagrangian particle trackung algortihms*, Experiments in Fluids, 40, 301-313, 2006.

Paret J. and Tabeling P., *Experimental observation of the two-dimensional inverse energy cascade*, Physical Review Letters, 79, 1997.

Perry A. E. and Chong M. S., *A description of eddying motions and flow patterns using critical-point concepts*, Annual Review of Fluid Mechanics, 19, 125-155, 1987.

Querzoli, G., *A Lagrangian study of particle dispersion in the unstable boundary layer*, Atmospheric Environment, 30(16), 2821-2829, 1996.

Ran B. and Katz J., *Pressure fluctuation and their effect on cavitation inception within water jets*, Journal of Fluid Mechanics, 262, 223-263, 1994.

Richardson L. F., *Atmospheric diffusion shown on a distance-neighbour graph*, Proceedings of the Royal Society of London, Series A, 110, 709-737, 1926.

Rossi L. and Ferrari S., *Particle Tracking Velocimetry and Accelerometry (PTVA) on electromagnetically controlled quasi-two-dimensional multi-scale flows*, Proceedings of the 12th ISFV (International Symposium on Flow Visualization), Gottingen (Germany), 2006.

Rossi L., Hascoët E., Vassilicos J.C. and Hardalupas Y., *2D fractal flow generated by electromagnetic forcing: laboratory experiments and numerical simulations*, Proccedings of the Fourth International Symposium on Turbulence and Shear Flow Phenomena (TSFP-4), Williamsburg, Virginia (USA), 485-490, 2005.

Rossi L., Vassilicos J.C. and Hardalupas Y., *Electromagnetically controlled multiple scale flows*, Journal of Fluid Mechanics, 558, 207-242, 2006a.

Rossi L., Vassilicos J.C. and Hardalupas Y., *Multi-scale laminar flows with turbulent-like properties*, Physical Review Letters, 97, 144501, 2006b.

Saffman P.G., *The lift on a small sphere in a slow shear flow*, Journal of Fluid Mechanics, 22(2), 385-400, 1965.

Salmon R., *Lectures in Geophysical Fluid Dynamics*, Oxford Press, New York, 1998.

Satijn M. p., Cense A. W., Verzicco R., Clercx H. J. H. and van Heijst J. F., *Three dimensional structure and decay properties of vortices in shallow fluid layers*, Physics of Fluids, 13 (7), 1932-1945, 2001.

Shi J. and Tomasi C., *Good* features *to track,* Proceedings of the IEEE Conference on Computer Vision and Pattern Recognition (CVPR94), Seattle, USA, 1994.

Sommeria J., *Experimental study of the inverse cascade in a square box*, Journal of Fluid Mechanics, 170, 1986.

Staicu A., Mazzi B., Vassilicos J. C. and van de Water W., *Turbulent wake of fractal objects*, Physical Review E, 67, 066306, 2003.

Stanislas M., Okamoto K., Kähler C.J. and Westerweel J., *Main results of the Second International PIV Challenge*, Experiments in Fluids, 39, 170-191, 2005.

Tabeling P., *Two-dimensional turbulence: a physicist approach*, Physics Reports, 362, 1-62, 2002.

Taylor G. I., *Diffusion by continous movement*, Proceedings of the London Mathematics Society, 20, 196, 1921.

Tatarski V. I., *Radiophysical methods of investigating atmospheric turbulence*, Izv. Vyssh. Uchebn. Zaved. Radiofiz., 4, 551–583, 1960.

Thibault J. P. and Rossi L., *Electromagnetic flow control: characteristic numbers and flow regimes of a wall normal actuator*, J. Phis. D: Appl. Phys, 36, 2559-2568, 2003.

Tsinober A., *An informal introduction to turbulence*, 1-324, Kluwer Academic Publishers, 2001.

Tsinober A., Vedula P. and Yeung P.K., *Random Taylor hypothesis and the behaviour of local and convective accelerations in isotropic turbulence*, Physics of Fluids, 13(7), 1974-1984, 2001.

Vassilicos J.C., *Mixing in vortical, chaotic and turbulent flows*, Philosophical Transactions of the Royal Society of London, Series A, 360, 2819-2837, 2002.

Vedula P. and Yeung, P.K., *Similarity scaling of acceleration and pressure statistic in numerical simulations of isotropic turbulence*, Physics of Fluids, 11(5), 1208-1220, 1999.

Virant M. and Dracos T., *3D PTV and its application on Lagrangian motion*, Measurement Science and Technology, 8, 1539-1552, 1997.

Voth G. A., La Porta A., Crawford A. M., Alexander J. and Bodenschatz E., *Measurement of particle accelerations in fully developed turbulence*, Journal of Fluid Mechanics, 469, 121-160, 2002.

Voth G. A., Saint T. C., Dobler G. and Gollub J. P., *Mixing rates and symmetry breaking in two-dimensional chaotic flow*, Physics of Fluids, 15, 2560-2566, 2003.

Voth G. A., Satyanarayan K. and Bodenschatz E., *Lagrangian acceleration measurements at lerge Reynolds numbers*, Physics of Fluids, 10(9), 2268-2280, 1998.

Westerweel J., *Effect of sensor geometry on the performance of PIV interrogation*, in: Adrian et al (editors*), Laser techniques applied to fluid mechanics*, Springer, Berlin Heidelberg New York, pp 37-55, 2000.

Williams B. S., Marteau D. and Gollub J. P., *Mixing of a passive scalar in magnetically forced two-dimensional turbulence*, Physics of Fluids, 9, 1997.